Spatial Anisotropy Characterization and Magnetic Domain Image Analysis in $La_{0.7}Sr_{0.3}MnO_3$ Based 'Donut' Micromagnets

By

TANAYA SAHOO

THESIS

Submitted in partial satisfaction of the requirements for the degree of

MASTER OF SCIENCE

in

MATERIALS SCIENCE AND ENGINEERING

in the

OFFICE OF GRADUATE STUDIES

of the

UNIVERSITY OF CALIFORNIA

DAVIS

Approved:

Yayoi Takamura, Chair

Seung Sae Hong

Roopali Kukreja

Committee in Charge

2024

Spatial Anisotropy Characterization and Magnetic Domain Image Analysis in $La_{0.7}Sr_{0.3}MnO_3$ Based 'Donut' Micromagnets

---

ABSTRACT

Developing next-generation computing devices based on spintronics and magnonics requires understanding how spin textures can be tailored in patterned magnetic materials. Lithographically patterned micro/nanostructures can provide insights into the formation of magnetic domains consisting of flux closure states that are potential building blocks of magnetic memory. Complex oxides such as epitaxially grown $La_{0.7}Sr_{0.3}MnO_3$ (LSMO) thin films exhibit strong correlations among spin, orbital, charge, and lattice degrees of freedom. As a soft ferromagnet, LSMO is a promising material for analyzing complex spin textures and controlling domain configurations by varying the micromagnet geometry. Using x-ray photoemission electron microscopy, thermally demagnetized LSMO donuts i.e., circular micromagnets with variable hole diameters, were imaged. The combination of quantitative image analysis and micromagnetic simulations allows probing and explaining the formation of spin textures consisting of either a single vortex or a pair of concentric vortices with opposite chirality in the donut structures. The results presented in this research are a step towards furthering our understanding of magnetic spin texture formation and vortex dynamics for developing spin-based devices.

ACKNOWLEDGEMENTS

I am immensely grateful to my advisor, Professor Yayoi Takamura, who, despite her many responsibilities as the Department chair, has perpetually extended unwavering support, invaluable guidance, and patience throughout my Master's journey. I sincerely thank Professor Seung Sae Hong and Professor Roopali Kukreja for their contributions as members of my thesis committee.

Thanks to Dr. Dayne Sasaki, my fellow Takamura group member and now an alumnus, for patiently allowing me to pick his brain apart in navigating the complexities of my research and pushing me to the best possible outcomes; to Ishmam Nihal, Hudson Shih, and Dr. Mingzhen Feng of the Takamura Research Group for training me on equipment and being supportive peers since I commenced lab work; to rest of the Takamura group, old and new that I had a pleasure interacting with in my time at University of California, Davis and making acquaintances. Special compliments to group alumni Dr. Michael Lee and Dr. Thomas Wynn for laying the foundations of micromagnetic work that inspired me to take a deep dive into this research.

I acknowledge the contributions of our collaborators at the Oak Ridge National Laboratory, Dr. Scott Retterer, for the lithography patterning of the sample; to the beamline scientists at the Dichroism group, Advance Light Source, Dr. Alpha N'Diaye, Dr. Barat Achinuq, Dr. Christoph Klewe and Dr. Andreas Scholl (now, Deputy for Science and the Interim Director of the Advanced Light Source).

Last but not least, I want to express my heartfelt gratitude to my amazing parents for their endless love, especially for keeping up with their wild child's often far-fetched ambitions; my baby sister looking up to me and loving me; my big fat family for their support and affection as I set forth in my journey overseas; and my two late grandmothers for blessing me in body and spirit.

Table of Contents

List of Figures

Chapter 1: Introduction

Mankind had embarked on a captivating journey churning magnetism with device innovation since the ancient scientific discovery of the lodestone. Imagine the astonishment of ancient explorers stumbling upon a magnetic rock guiding their compass needles toward the Earth's magnetic poles. Fast-forward through centuries of scientific inquiry, and we find ourselves at the frontier of innovation, developing advanced electronic devices and harnessing the unseen forces of magnetic fields. The chance encounter with lodestone serves as a prologue, setting the stage for the latest chapter in the ever-evolving saga of materials science and device engineering. From Samuel Morse's electromagnetic telegraph to magnetic storage media, from transformational diagnostics of magnetic resonance imaging to magnetic levitation trains and quantum computing with q-bits, science is at the precipice of spintronics - a promising technological odyssey leveraging electron spin for advancing device innovation. The significance of the electron's spin in governing transport properties was underscored by Sir Nevill Mott as early as 1936 [1], marking a pivotal moment in understanding the electrical conductivities of transition metals and their alloys. The inherent spin nature of electron transport, elucidated by Mott's model, forms the cornerstone of contemporary magnetic data storage technologies, exemplified in computer hard drives and magnetic random-access memories (MRAMs). Moving forward exploring further possibilities, the controlled manipulation of electron spin in correlated material systems is central to data encoding and retrieval processes. Understanding the intricate arrangement of magnetic moments on a microscopic scale has been paramount.

1.1 Spintronics

The frontline of the electronics industry consists of computing (memory and logic). A critical constraint of developing computing devices lies in the escalating power consumption necessitated by the pursuit of higher processing speeds. Mitigating this challenge involves the exploration of alternative solutions, with one notable approach being the advancement of multi-core processors. While these processors offer a potential reduction in power requirements, they also introduce a significant demand for larger memory. Consequently, the proportion of silicon chips allocated to memory is expected to surge from current typical values, reflecting the evolving landscape of computing architectures. *Spintronics*, short for spin transport electronics, represents a revolutionary paradigm in electronics that goes beyond traditional charge-based approaches. Unlike conventional electronics, where information is encoded using the charge of electrons, spintronics exploits the intrinsic spin property of electrons. It aims to overcome these limitations by harnessing the spin of electrons. Triggered by the discovery of giant magnetoresistance (GMR) in 1988 [1], the development of these devices leverages the spin degree of freedom inherent in electrons and/or holes, a property that can interact with their orbital moments. The control of spin polarization in such devices is achieved through magnetic layers serving as spin-polarizers or analyzers, or through spin-orbit coupling.

Additionally, spin waves can be harnessed as carriers of spin current. Spin-polarized currents can be generated by capitalizing on the impact of spin on the transport characteristics of electrons within ferromagnetic conductors. This concept, initially proposed by Mott [2], had been experimentally validated and theoretically elucidated in earlier studies, over a decade before the unveiling of the GMR phenomena [3]. Mott's influential two-current model, wherein conductivity is expressed as the sum of two unequal contributions from distinct spin projections, provided a

profound explanation for the elevated resistivity observed in ferromagnetic metals compared to their nonmagnetic counterparts.

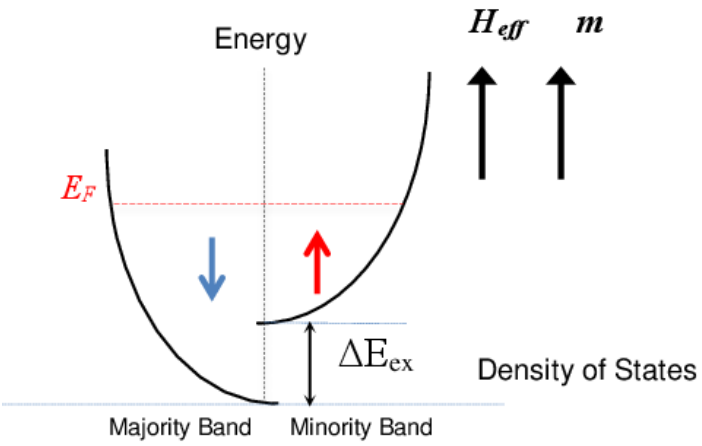

Fig. 1.1 Description of the band structure in transition metals showing band splitting in the presence of an effective magnetic field H_{eff}, which can induce magnetic moment *m*. Arrows depict spin-up and down electron configuration. Adapted from Ref. [4].

This model not only introduced the concept of spin transport but also highlighted the crucial role of magnetism in shaping transport properties. This distinction arises from the energy separation between the "majority spin" and "minority spin" directions (typically denoted as spin up and spin down) depicted in Figure 1.1. In a material, electrons occupy energy levels in what is known as the electronic band structure. At absolute zero temperature, all energy levels up to the Fermi level (E_F) are filled with electrons following the Pauli exclusion principle, which states that no two electrons can simultaneously occupy the same quantum state. When the temperature is increased above absolute zero, electrons can gain energy and move to higher energy states. In semiconductors, E_F is close to the middle of the bandgap, and its position can be shifted by doping or applying an external electric field, thereby influencing the material's conductivity.

Consequently, the position of E_F determines which electron states are available for conduction. In spin-polarized materials, the conduction properties for spin-up and spin-down electrons may differ, depending on their relative positions to E_F. Electrons near E_F contribute most significantly to electrical conduction, so spin-polarized electronic states near E_F can influence the material's conductive behavior.

The most prominent application of magnetic spin is seen in MRAM, as data gets written in the direction of magnetization of a ferromagnetic (FM) material [5]. As illustrated in Figure 1.2, MRAMs utilize the concept of a magnetic tunnel junction (MTJ) [5] [6] wherein a sandwich with two layers of special materials separated by a thin insulating layer resulting in one layer changing its direction with a small magnetic field (free layer), while the other keeps a fixed direction (reference layer). Data stored is represented as "one" and "zero," based on the free layer's magnetization direction.

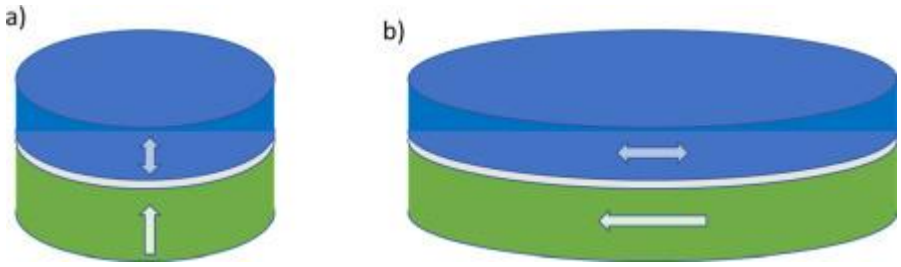

Fig. 1.2 (a) Schematic diagram of an MTJ with perpendicular magnetization and (b) MTJ with in-plane magnetization. The *double-sided arrow* indicates the magnetization of the free layer having two stable states with magnetization in opposite directions along the same axis. The *single-sided arrow* indicates the reference layer has a magnetization direction set in a particular direction and remains in that direction in normal MRAM operation. The MTJ devices used in MRAMs have low resistance in the parallel magnetic state and high resistance in the antiparallel state [8].

A notable limitation in MTJ elements is that field writing is susceptible to thermal fluctuations, causing the free layer's magnetic moment to overcome the magnetic anisotropy energy barrier if

the barrier is not large enough, consequently reversing the free layer's magnetization direction. Such drawbacks call for exploring novel alternatives in device engineering like "toggle" switching [4][8]. By introducing a thin layer of antiferromagnetic (AFM) material to couple between two magnetic layers, the magnetization direction can be toggled between two stable states with the application of external stimuli such as magnetic fields or spin currents. This effect occurs due to exchange coupling between the FM and AFM layers and helps to achieve a much greater degree of combination of writing bit values (0s or 1s). Further, high fields leading to increased power consumption are tackled by introducing the concept of spin transfer torque (STT) to enhance the efficiency of novel spintronics [10].

However, countering high breakdown voltages and seeking better writing threshold control has called upon robust advancements in novel spintronics such as the concept of *racetrack memory.* Initially, proposed by IBM in 2002, [11] this memory storage scheme of storing data within magnetic domains (within a magnetic material, similar orientations of magnetic moments form magnetic domains where the magnetization is uniform). At boundary regions referred to as domain walls (DW) between these domains (Figure 1.3), the magnetization undergoes a transition from one orientation to another. The data pattern resides as a series of DWs in a microscopic FM wire (or racetrack), and current pulses are used to move the entire pattern along the wire for reading and writing.

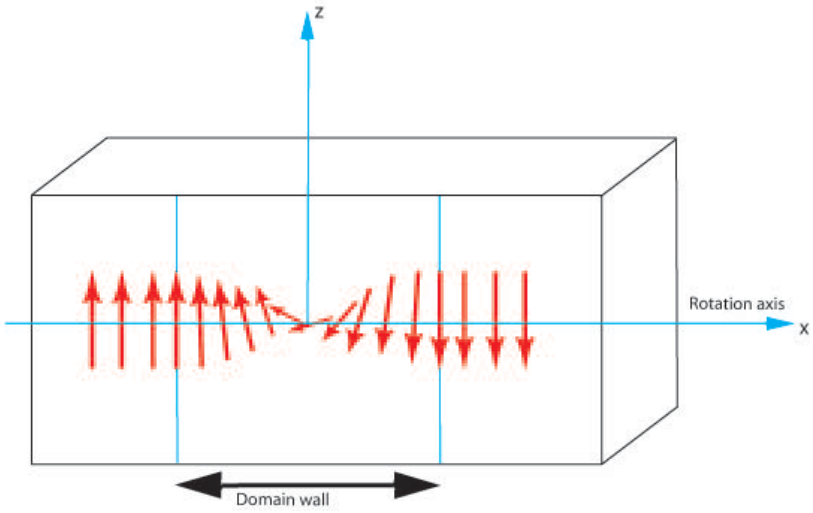

Fig. 1.3 Schematic representation of domain walls showing different transitions of the magnetization between magnetic domains [12].

What sets racetrack memory apart is its use of the spintronic concept of "spin momentum transfer" rather than magnetic fields to move the DWs. In this approach, the spin-polarized current carries spin angular momentum, allowing precise and efficient movement of DWs along the racetrack (illustrated in Figure 1.4).

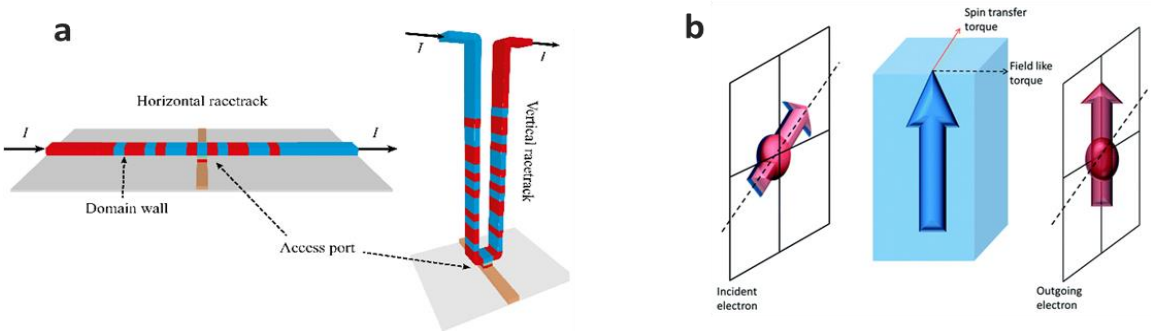

Fig. 1.4 (a) Horizontal and vertical racetracks with one access port. The current flows through the device in the direction of bit motion. **(b)** Illustration of current-induced torques that arise from the interaction between spin-polarized conduction electrons and the magnetization of an FM material. This interaction causes a change in the spin polarization direction of the outgoing electron, resulting in torques on the FM layer. The torque within the plane of incident and outgoing spin directions is called spin-transfer torque, while the torque perpendicular to this plane is termed a field-like torque. The bold blue arrow represents the magnetization vector of the ferromagnet [13].

When this spin angular momentum is transferred to a magnetic DW, it induces a torque, allowing for controlled displacement of the DW along the racetrack. The critical factor at the heart of this application is achieving more direct and efficient means of manipulating DWs, contributing to the remarkable functionality of racetrack memory. The nature of the racetrack, whether composed of magnetically "soft" or "hard" materials, significantly influences its behavior. Soft materials are characterized by their easy susceptibility to magnetization and demagnetization in response to an applied magnetic field, whereas hard materials are resistant to demagnetization once they are magnetized. Their behavioral distinction concerning racetrack memory hinges on the ratio of "magnetic anisotropy energy" to "magnetostatic energy" (discussed in section 3.1.3), as well as structural factors such as crystal structure or surface and interface contributions [7], [14], [15]. The quality factor refers to the following equation,

$$Q = \frac{K}{2\pi M_S^2}, \qquad \text{(Equation 1.1)}$$

where K is the anisotropy constant, and M_S is the saturation magnetization. This ratio dictates the material's ability to resist changes in magnetization direction.

In soft magnetic materials, 'shape anisotropy,' where the material's geometry influences magnetic behavior, and DW manipulation can provide extraordinary insights for technology innovation. With $Q << 1$, indicating a low resistance to changes in magnetization, soft materials exhibit heightened sensitivity to external influences. Specifically, transition metal oxides that are soft FM materials, introduce a dynamic range of possibilities not just for manipulating the material's predisposition to magnetization changes but also for deterministic switching of magnetization profile [16] [17]and domain engineering [18] [19].

1.2 Magnetism in Complex Oxide Perovskites

Complex oxides, often perovskites (illustrated in Figure 1.6), provide a wide avenue to probe into unique crystalline structures and their applications in tunable magnetic and electronic properties. The structural diversity of complex oxides incentivized by the tailoring of lattice and ordered arrangement of ions present a myriad of functionalities, including superconductivity [20], metal--to-insulator transitions (MIT) [21], and colossal magnetoresistance. A comprehensive depiction of elements forming a perovskite structure that are compatible with the structure specifications is provided in Figure 1.5. A typical perovskite oxide unit cell has an A ion at the cube corners, a B ion at the body center, and oxygen ions at the face centers, as illustrated in Figure 1.6.

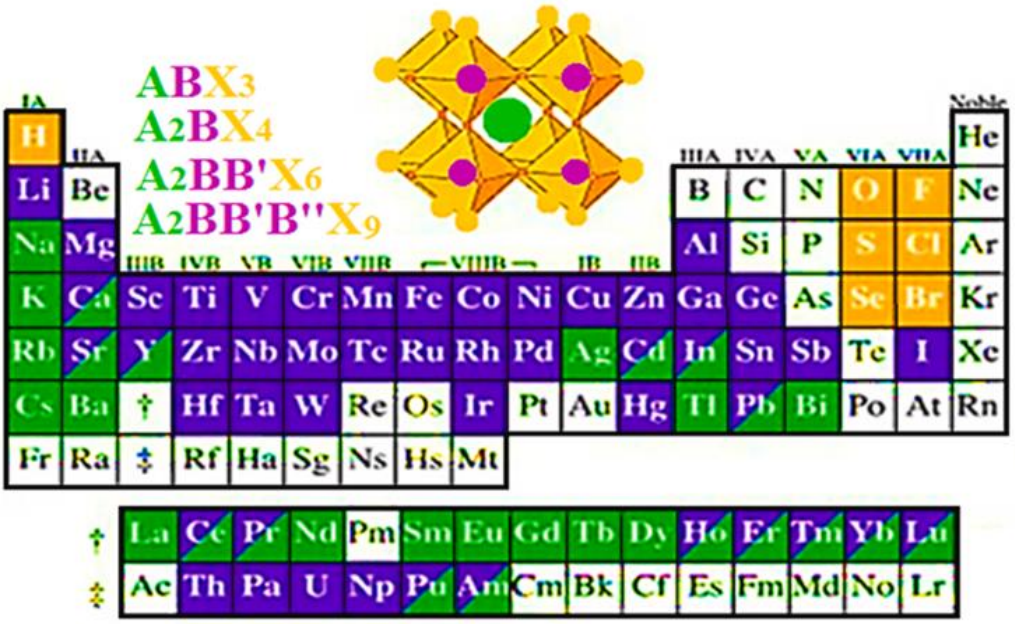

Fig. 1.5 Elements on the periodic table compatible with the perovskite structure [49].

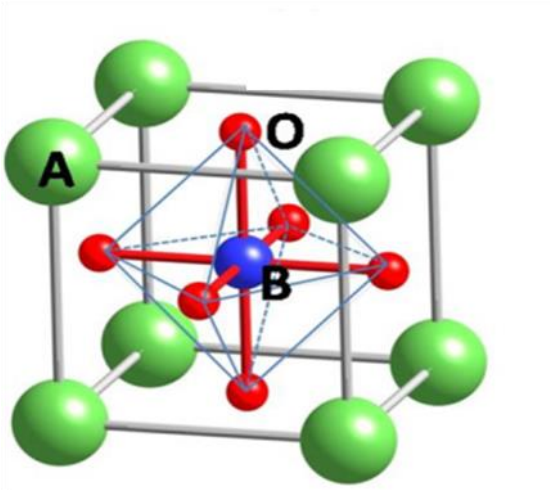

Fig 1.6 An ideal perovskite unit cell with general formula ABO_3 and octahedral coordination of BO_6 in the cubic crystal structure [23].

Additionally, the interplay of spin, charge, orbital, and lattice degrees of freedom in complex oxides serves as a playground for not only exploring novel functionalities of spintronics, superconductivity, and multiferroics but also probing material systems like complex oxide heterostructures or superlattices [24]. This flexibility of the ABO_3 perovskite structure allows for a plethora of potential substitution of various elements at the cationic and anionic sites, a crucial aspect in complex oxide doping. The Goldschmidt tolerance factor (t),

$$t = \frac{(r_a + r_b)}{\sqrt{2}(r_b + r_o)} \qquad \text{(Equation 1.2)}$$

which considers the ionic radii r_a, r_b, r_o of the constituent ions, and ensures structural stability by assessing whether the combination of elements fits well within the perovskite lattice. In the case of half-metallic magnetic oxides like (La, Sr)MnO_3 and (La, Sr)CoO_3, which adopt the perovskite structure, this versatility becomes evident [24],[25],[27]. The B-O-B bond fluctuations within octahedron coordination affect the balance between the electrostatic forces and the inherent flexibility of the oxygen atoms in response to the transition metal ion's presence. Following the illustration in Figure 1.6, this dynamic environment gives rise to crystal field splitting [32]. In this

phenomenon, the degeneracy of *d* orbitals of the transition metal ion is lifted due to the surrounding oxygen ligands [28]. The crystal field effect alters the energy levels of the *d* orbitals, creating a distinct pattern of energy states. They set the stage for subsequent phenomena, such as Jahn-Teller distortions [29], where the interactions between electrons and the crystal lattice further modify the electronic states, introducing additional complexity to the material's properties. Together, these factors contribute to the rich and diverse behaviors observed in complex oxides, making them intriguing subjects.

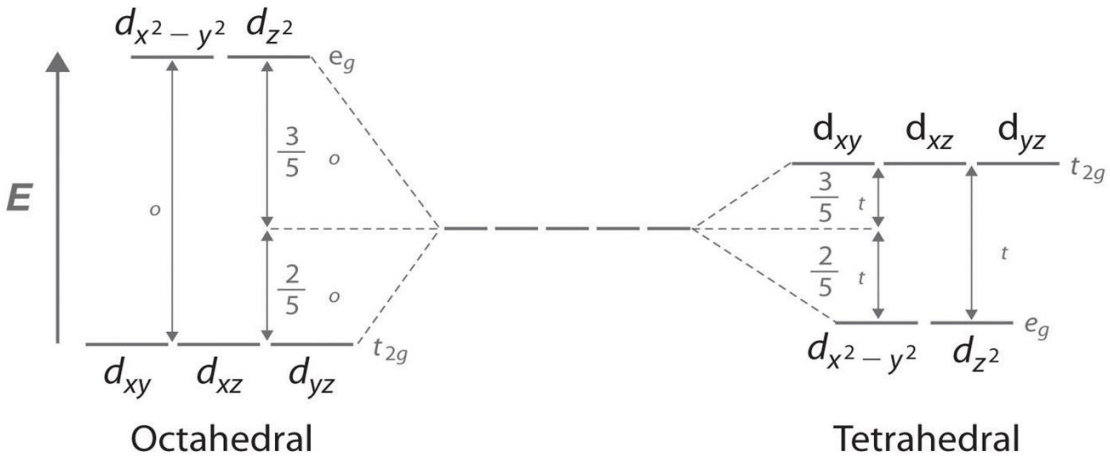

Fig 1.7 Crystal field splitting in a transition metal complex [30]. The ligands generate a repulsive electric field that affects the energy levels of the *d* orbitals differently depending on their orientation and distance from the metal ion. This effect results in the splitting of degenerate *d* orbitals into different energy levels, forming a series of higher-energy orbitals and a series of lower-energy orbitals.

Magnetism in complex oxides is fundamentally rooted in indirect exchange interactions wherein the transition metal ions exhibit localized magnetic moments or the alignment of electron spins. Two prominent types of exchange interactions dominate in complex oxides: the FM exchange [31], favoring parallel alignment of spins, and the AFM superexchange [32], favoring antiparallel

alignment. These interactions, influenced by factors like crystal structure, electronic configurations, and temperature, determine the magnetic properties of the material [33]—strong Coulomb interactions and a large density of states at the Fermi energy cause spontaneous ferromagnetism [34]. Moreover, this arrangement of spins is closely connected to the concept of the "Curie temperature" T_c, a pivotal parameter in ferromagnetism. As material is heated beyond its T_c, the FM order begins to unravel, causing a transition to a paramagnetic state. In addition to the interatomic exchange mechanisms, intra-atomic exchange interactions exist in complex oxides, exemplified by the presence of specific ions like Fe, Ni, or Mn. Notably, magnetic moments in transition-metal elements, like Ni, deviate from integer values, showcasing a moment of 0.61 μB per atom [33]. This departure from integer values is indicative of the itinerant Stoner exchange- a fundamental quantum mechanical phenomenon[35], which encompasses both inter and intra-atomic contributions.

In mixed-valence systems such as manganite with the perovskite structure, two types of indirect exchange interaction mechanisms arise- *superexchange* and *double-exchange*, as illustrated in Figure 1.8. In superexchange, an FM or AFM alignment occurs between two atoms in mixed valence states, while in double-exchange, the interaction occurs only when one atom has an extra electron resulting in FM alignment only. The superexchange mechanism considers intermediate exchange interactions between the anion and cation orbitals (*p*-type of oxygen and *d*-type of transition metal M for case in point) either when the orbitals align in 180 degrees (refer to cases 1 and 2 in Fig. 1.8(b)) or 90 degrees (case 3 in Fig. 1.8(b)). Unlike superexchange, the double-exchange mechanism results from a combination of Coulombic and kinetic exchange of the mixed-valence cations without any intermediate exchange with the anion that changes the anionic valence state during hopping (Fig. 1.8(a)). In a sense, the 90-degree superexchange mechanism discussed

above is a double exchange mechanism but mediated via the Coulomb exchange on the connecting oxygen. The presence of anion here, however, influences the degree of overlap between the magnetic ions, and electron localization for transfer as the electron hopping probability is enhanced by a critical bond angle (M-O-M) closer to 180 degrees.

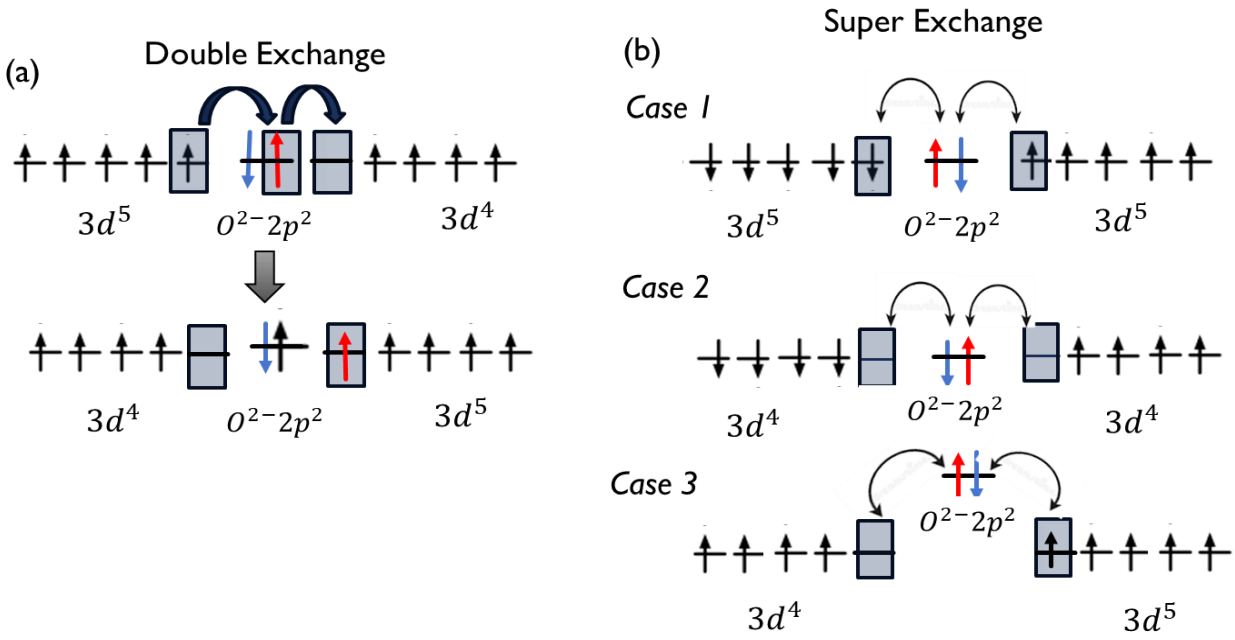

Fig 1.8 Illustration of double and superexchange mechanisms in perovskites. Schematics show spin orientations as one-sided arrows and double-sided arrows represent the transfer in orbitals. **(a)** The double exchange shows electrons use the oxygen anion to 'hop' (characterized by a hopping probability 't') from one cation to another. **(b)** The superexchange mechanism is further shown in three different cases for a 180° M-O-M bond: Case 1: an AFM ordering is established between two half-filled orbitals; Case 2: an AFM ordering is established between two empty orbitals; or Case 3: an FM ordering is established between one half-filled and one empty orbital where *p* and *d* orbitals align 90 degrees. In all cases, Pauli's exclusion rules must be obeyed.

In the case of the double-exchange, when an itinerant electron hops between B-type cations, like from an Mn^{3+} (B1) ion to an Mn^{4+} (B2) ion, the spins become aligned, resulting in an FM interaction [36]. This ferromagnetism can lend metallicity to mixed valence ion state cases. This

process is energetically favorable, driving the system toward an FM ground state. The strength of the double exchange interactions is influenced by the degree of overlap between the electron orbitals of the participating ions and the energy gain is associated with spin alignment. This phenomenon not only dictates their magnetic order but also contributes to intriguing phenomena like colossal magnetoresistance (CMR) [37], [38]. Superexchange often occurs in materials with partially covalent bonding between the magnetic and non-magnetic ions, as depicted in Figure 1.8. This covalent bonding facilitates the overlap of electron orbitals and the hopping of electrons between neighboring ions while obeying Pauli's exclusion rules. Depending on the relative orientations of the magnetic moments on neighboring ions, superexchange can result in either FM or AFM ordering. It is to be noted the AFM superexchange interactions in Cases 1 and 2 are stronger than the FM superexchange in Case 3 [39], [40], [41], [42]. Moreover, combined with these exchange interactions, crystal field effects, and lattice distortion influences on the overall magnetic behavior of manganites, they are a fascinating class of materials for fundamental studies and practical applications for spintronics.

1.3 $La_{0.7}Sr_{0.3}MnO_3$ (LSMO) complex oxide

Notable among the mixed valence manganite for its double exchange and CMR is $La_{1-x}Sr_xMnO_3$, a "half-metallic ferromagnet" with a maximum $T_c \sim 360$ K for x= 0.3 [43], [44]. The wide variety of structural, electronic, and magnetic phases that LSMO exhibits is provided in Figure 1.9.

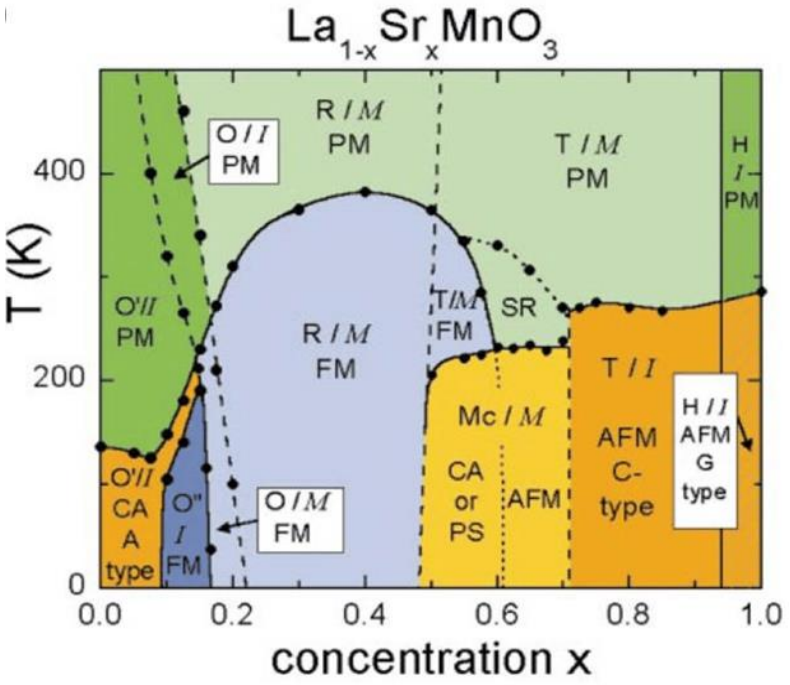

Fig 1.9. Phase diagram of single-crystalline $La_{1-x}Sr_xMnO_3$ as a function of Sr-doping concentration, x, and temperature, T [45]. Information about the structural, magnetic, and electronic properties are given with the following symbols. Structure: O – orthorhombic, O' – Jahn-Teller distorted orthorhombic, O'' – orbital-ordered orthorhombic, R – rhombohedral, T – tetragonal, Mc – monoclinic, H – hexagonal. Electronic state: M – metallic, I – insulating. Magnetic ordering: FM – ferromagnetic, PM – paramagnetic, SR – short-ranged order, PS – phase separated, AFM – antiferromagnetic with A-, C-, or G-type moment ordering

The unique characteristics in stoichiometric $La_{0.7}Sr_{0.3}MnO_3$ (LSMO) are crucial in advancing spintronics, particularly in achieving 100% spin polarization at the E_F. Its half-metallic behavior ensures that one of the spin bands completely lacks states at E_F, while the other remains fully populated and attains maximal spin polarization [46]. Moreover, the development of MTJs for non-volatile memory applications has pioneered the concept of tunnel magnetoresistance (TMR), quantified by Jullière's expression [47]:

$$\text{TMR} = \frac{R_{AP} - R_P}{R_P}, \qquad \text{(Equation 1.3)}$$

where R_{AP} is the electrical resistance in the antiparallel state, and R_P is the resistance in the parallel state. This concept builds on the spin-dependent transport properties of materials like LSMO due to the relative alignment or misalignment of magnetic moments in the adjacent layers [48]. The concept of TMR is intricately linked to the spin-polarized transport of electrons and hence, crucial in spintronic applications. LSMO is a perovskite structure that can accommodate an extensive range of atoms into various atomic positions, as shown in Figure 1.5. LSMO exhibits unique charge transport and magnetic properties influenced by dopant size and content, which determine the tolerance factor. When Sr^{2+} ions replace La^{3+} ions in the parent $LaMnO_3$, an insulating AFM material [49], it converts Mn^{3+} ions to Mn^{4+} ions and subsequent ferromagnetism through the double exchange mechanism, illustrated in Figure 1.8. This induces itinerant holes, causing carrier delocalization in the FM phase at a doping concentration around x = 0.3. The hopping probability (t) of carriers is influenced by the alignment of manganese spins. Temperature-dependent behaviors, such as the metal-insulator transition (T_{MI}), are attributed to the double exchange mechanism and the localization of itinerant carriers by Jahn-Teller distortions of the oxygen octahedron surrounding each Mn ion (Figure 1.10). These distortions arise from the spontaneous tendency of trivalent Mn^{3+} ions to lift orbital degeneracy.

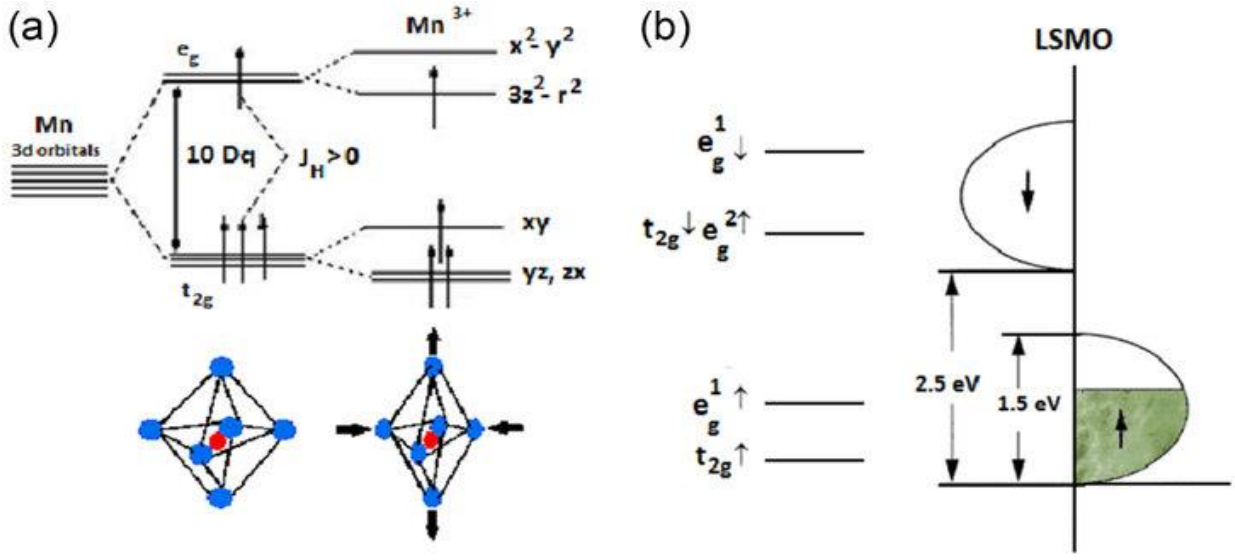

Fig. 1.10. (a) Schematic of crystal field splitting of Mn ions proposed by C. Zener [33]. (b) Energy diagram of the orbitals of a free transition metal in an octahedron crystal field formed by O atoms, and in an octahedron with distortion (Jahn-Teller effect) as adapted from Ref [51]. The Right panel shows a schematic illustration of the density of states of LSMO [52].

This model explains conductivity below the T_c and high resistivity around the T_{MI} and the CMR, characterized by a huge peak in magnetoresistance [38],[52]. This, combined with a high STT efficiency [53], makes LSMO-based structures promising candidates for exploring micromagnetism, where spin-textures could be manipulated to develop spintronic applications [54].

An extremely relevant factor in this mix is LSMO's 'magnetocrystalline anisotropy' (MCA), which occurs when the crystal lattice of an object influences its preferred direction for magnetization (described further in Section 3.1.3). Several half-metallic materials like CrO_2, exhibit large magnetocrystalline anisotropies and have been investigated for ease of controlling magnetic domains [45], [55]. However, controlling magnetic anisotropies in a materials system with MCA like LSMO ($K_1/M_S \sim -0.01$ T) remains unresolved. With a $T_c \sim 360$ K and promising

magneto-transport properties discussed above, epitaxially grown LSMO thin films are particularly favorable candidates to explore for tailoring of spin structure. This idea is the principal motivation behind designing LSMO-based micromagnets and probing their magnetic behavior in this thesis work. While the physical width of the domains is controlled by the exchange and MCA energies, the driving force behind the formation of the domains in micromagnets with varying shapes and sizes is the 'magnetostatic energy.' Represented in Figure 1.11, adding additional domains going from Figure 1.11 (a) to (c) allows the magnetic material to minimize its total magnetostatic energy (or '*stray fields*' shown in blue lines) by redistributing magnetic flux. Demagnetizing fields arise due to the tendency of magnetic domains to align in a manner that reduces the overall magnetostatic energy of the system. These fields exert forces on the magnetic domains, influencing their orientation and distribution within the material. Furthermore, the energetic landscape carved by a specific combination of demagnetizing fields and MCA complicates the behavior of magnetic materials.

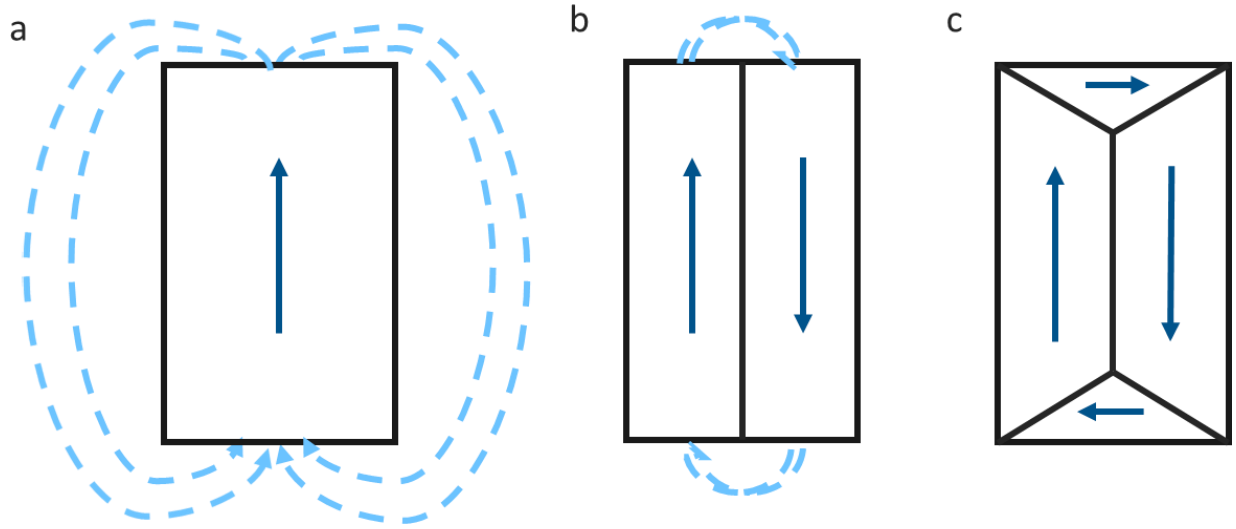

Fig. 1.11 Illustration of emanating magnetic fields (in light blue arrows) around domains (dark blue arrows) that have preferred orientations of the magnetization vector. (a)-(c) depicts a growing number of domains decreasing stray fields.

In LSMO films, the orientation of magnetocrystalline axes plays a crucial role in determining the material's magnetic properties. The difference in energy associated with magnetization along the "hard" and "easy" axes defines the magnetocrystalline energy for a material system; easy refers to the preferred direction of magnetization. To minimize this energy, magnetic domains form in a way that aligns their magnetizations along the easy crystallographic directions. For bulk LSMO, [100] and [110] directions correspond to easy and hard axes, respectively [56]. Under small tensile strain, LSMO thin film is known to have <110> directions as the easy axes [57]. Illustrated in Figure 1.12, examining hysteresis loops obtained under different magnetic field orientations, one can associate remnant magnetization as an indicator of the easy directions. Typically, remnant magnetization is higher along the easy axis in a hysteresis loop considering the material's magnetic domains align more readily in this direction hence, requiring less external magnetic field to achieve saturation magnetization. Conversely, along the hard axis, remanent magnetization is lower due to the increased difficulty in aligning the domains. 'Coercivity' is a fundamental property of magnetic materials that measures their resistance to demagnetization. It represents the intensity of an external magnetic field required to reduce the material's magnetization to zero after fully magnetizing it in a specific direction. Figure 1.12 shows a higher remnant magnetization for the easy direction, however, the presence of defects that often pin domain walls, may increase coercivity, thus, influencing MCA directions.

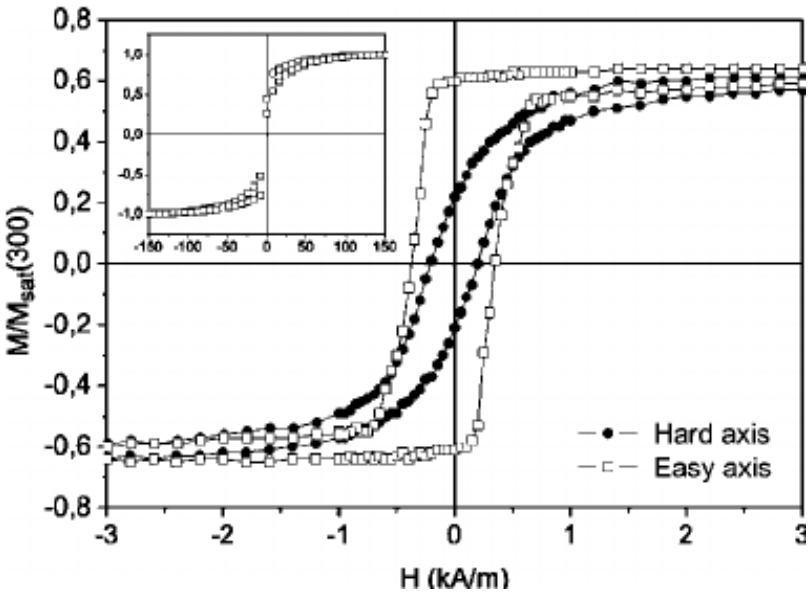

Fig 1.12 The magnetic hysteresis (M-H) loops of a coherently strained LSMO thin film (25 nm) along hard and easy directions adapted from Ref. [58]. Depending on the crystallographic orientation of the sample in the magnetic field, the magnetization reaches saturation in the two different anisotropy fields – hard and easy axes. The inset shows the magnetization measured up to full saturation.

In the context of magnetization, work is necessary to rotate moments away from their easy axis, quantifying the definition of MCA energy, denoted as E_K. For a cubic crystal structure, the expression for E_K is as follows:

$$E_K = K_0 + K_1 (\alpha_1^2 \alpha_2^2 + \alpha_2^2\alpha_3^2 + \alpha_1^2\alpha_3^2) + K_2 (\alpha_1^2\alpha_2^2\alpha_3^2) + \ldots \quad \text{(Equation 1.4)}$$

Here, K_0, K_1, *and* K_2 represent magnetocrystalline anisotropy constants, while the α values correspond to the cosines of angles between crystallographic axes and the magnetic saturation direction. Notably, K_0 remains orientation-independent and is effectively disregarded when comparing properties across different directions. Typically, K_2 is negligible in cubic crystals. Hence, K_1 is the primary determinant quantifying magnetocrystalline anisotropy. This context will be further enunciated in Section 2.1 for Micromagnetic Simulations in Chapter 2, corroborating quantitative techniques applied in this research.

Recent research has focused on identifying materials and structural configurations conducive to integrating magnetic domain features like ‘skyrmions’ into functional devices [59]. One avenue of exploration involves the development of specially crafted metal heterostructures featuring spatially divergent spin−orbit torque. Additionally, efforts have been made to embed a magnetic “vortex” within a perpendicular spin environment. Despite these advancements, a comprehensive understanding of the spatial distribution of fundamental magnetic characteristics in nano/microstructures remains largely untapped. This is particularly pertinent in various material categories, with complex oxides especially sensitive to lattice strains, as functional properties are intricately linked to their structural properties.

The profound impact of magnetic anisotropies because of varying geometry in LSMO micromagnets can play a crucial role as an additional tunability parameter in stabilizing spin-based magnetic memory devices. In this context, domain patterns observed in LSMO circular micromagnets by Lee *et al.* [60] paint a dramatic energetic landscape where domain patterns tend to align themselves along specific crystallographic directions to minimize the system's overall energy. This study looked into the magnetic domain characterization of LSMO-based micromagnets of varying geometry and obtained interesting insights into the balance of MCA. The results on chiral domain patterns and magnetic anisotropy potentially render them highly appealing for applications in nanoscale spintronic devices or in building magneto-logic devices which require information to be encoded in a resulting magnetic configuration or by using magnetic domains as the fundamental unit for memory storage. In this thesis, I will address the micromagnetic domain evolution observed in patterned LSMO thin films, specifically probing into the magnetic domain formations in a ‘donut’ geometry of LSMO micromagnets. The donut pattern was fabricated to remove the magnet domains' central vortex core- a characteristic feature of the chiral flux closure

domain patterns observed by Lee *et al.* in the circular discs that do contain a central hole. This donut geometry and the observed domain patterns add to the complexities of the spatial magnetism of the LSMO micromagnets (namely, magnetocrystalline anisotropy) that was previously observed. Hence, a quantitative characterization framework comprising of experimental and simulation techniques has been laid out in this thesis to understand the micromagnetism-driven spatial variation of magnetocrystalline anisotropy and their correlation with the thin film properties.

1.4 Summary

This chapter outlines the magnetism in complex oxide perovskites and sets the stage for deep diving into magnetic textures and their behavior at micro/nano scales. Chapter 2 describes various experimental techniques that serve as a tool kit to probe the magnetism of epitaxial thin films, namely crystalline single-layer LSMO. High-end magnetic domain imaging techniques like photoemission electron microscopy (PEEM)-based X-ray magnetic circular dichroism (XMCD) on patterned films unravel the intricacies of these domain textures, while computational methods enable characterization of these vortex textures and determination of the spatial distribution of magnetic energies. Chapter 3 will further delve into describing unique spin textures observed in circular micromagnets of LSMO, along with a qualitative description of the magnetic anisotropy state governing the formation of domain patterns. Building on the research done by Lee *et al.*, Chapter 4 presents a comprehensive discussion of analyses derived from experiments, micromagnetic simulations, and quantitative image analysis operations performed on spin textures observed in 'donut' shaped LSMO micromagnets. Finally, Chapter 5 provides objectives for future work and an outlook on this research work.

Chapter 2: Experimental and Computational Techniques

The experimental techniques in this research are the growth of LSMO thin films, patterning arrays of micromagnetic islands on the film, and scientific investigation of their magnetic spin textures. High-quality fabrication techniques like pulsed laser deposition employed in this work impart structural and compositional characteristics to growing complex oxide thin films and pave the way for using element-specific and magnetically sensitive soft x-ray spectroscopic techniques to probe their spin textures. The process of shaping micromagnetic structures onto thin films involves finely controlling the dimensions and arrangement of these structures at the micro/nanoscale. In this context, the goal was to engineer micromagnetic islands to facilitate the emergence and manipulation of magnetic domains within the LSMO thin films by using an ion-implantation-based patterning technique. This work involves not only controlling the physical dimensions and geometry of the microstructures but also ensuring their alignment and arrangement to influence the magnetic behavior of the material system. Micromagnetic simulations were performed to corroborate our understanding of quantitative aspects of magnetization and gauge the balance of the magnetic energetics in the imaged domain textures.

2.1 Pulsed Laser Deposition

The key to probing spin textures in material systems like complex oxides with specific magnetic properties lies in the synthesis technique that offers precise control over composition, thickness, and crystal structure. Growing high-quality thin films (in other words, a layer of a material with one dimension in the nanoscale) directly contributes to the ordered arrangement of atoms in crystal

systems responsible for the propagation of electronic and magnetic properties in conjunction with the crystallographic alignment of the substrate used. Thin films can experience strain due to lattice mismatch with the growth substrate [61]. This strain can significantly influence the structural, electronic, and magnetic properties of the thin film, leading to phenomena such as strain-induced phase transitions, enhanced carrier mobility, and modified magnetic ordering [62], [63], [64]. This strain is quantified by the lattice mismatch in the following relationship,

$$\varepsilon = \frac{(a_e - a_m)}{a_e} \qquad \text{(Equation 2.1)}$$

a_e and a_m are the lattice parameters of the unconstrained epilayer and matrix in a plane parallel to the interface. However, increasing the extent of misfit or thickness of films also increases the potential for developing defects/dislocations thus, deteriorating crystalline quality. Coherently strained thin films are crystalline layers of material grown on a substrate in such a way that their crystal lattice structure aligns in-plane with that of the substrate as shown in Figure 2.1. This alignment, known as *epitaxy*, results in a high degree of structural order and orientation of single crystals, making epitaxial thin films distinct from polycrystalline or amorphous films [65][66]. By carefully selecting substrates and growth conditions, several growth techniques exploit strain engineering capabilities to tune lattice properties [67], [68].

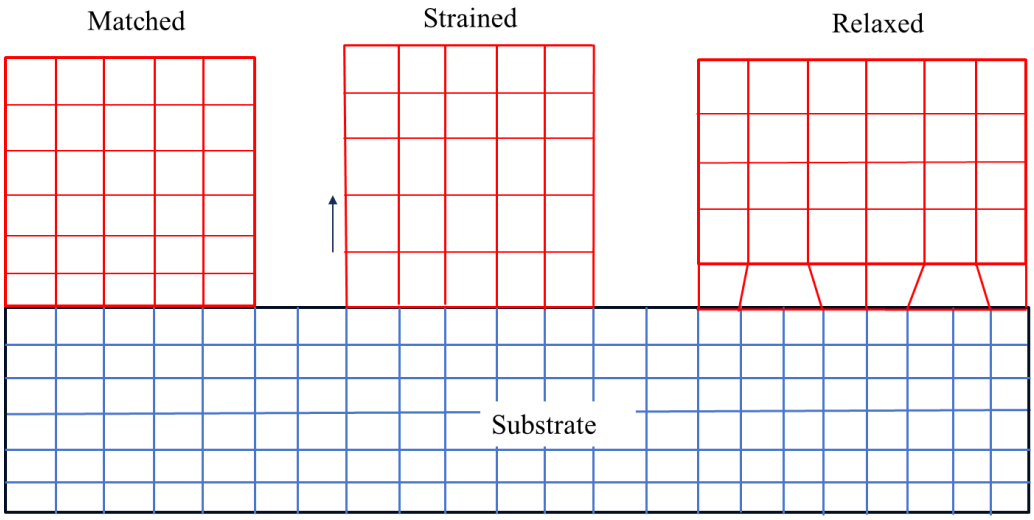

Fig 2.1 Illustration of the epitaxial growth process on a substrate (in blue) showing strain generation by lattice mismatch in thin films. Coherent strain arises from the lattice structure of the grown layer (in red) when heteroepitaxy occurs on a lattice-mismatched substrate (in blue). As shown, assuming cubic unit cells for the substrate, a biaxial strain can be induced in the grown film resulting in the expansion of the out-of-plane lattice parameter (tetragonal distortion). Relaxed strain occurs when a film's thickness exceeds the critical level in heteroepitaxy, the lattice undergoes relaxation, leading to changes in the average lattice strain. This relaxation is generally caused by the introduction of lattice imperfections, such as dislocations and defects, which result in a mixed strain state that can diminish the impact of pure elastic strain.

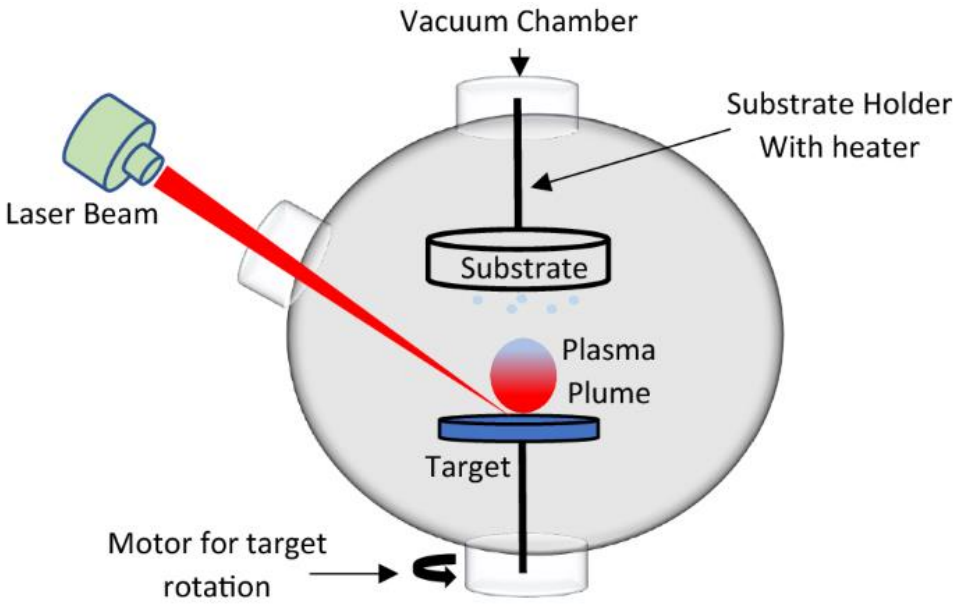

Fig 2.2 Schematic of PLD growth chamber [69].

Pulsed laser deposition (PLD) illustrated in Figure 2.2 is one such growth technique working on the principles of physical vapor deposition wherein a high-energy excimer laser pulse ablates material from a target, which is then deposited onto a substrate to form a thin film. This process offers several advantages for the growth of complex oxide thin films, namely the deposition of materials with diverse compositions, including complex oxides with multiple elements, while maintaining stoichiometry. The energetic laser pulse efficiently transfers material from the target to the substrate, preserving the chemical composition of the deposited film and aligning its in-plane crystallographic orientation by appropriately selecting a combination of material and deposition conditions. This step is crucial for complex oxide thin films, where precise stoichiometry is often necessary to achieve desired magnetic properties useful for emergent spintronic applications as discussed in Section 1.2. The body of work carried out towards this thesis specifically focuses on forming a coherent single crystal thin film (40 nm) of $La_{0.7}Sr_{0.3}MnO_3$ grown using PLD on an as recieved (001)-oriented Nb-doped $SrTiO_3$ (Nb:STO) substrate. The choice of substrate depends on the close relationship of its crystal structure with that of a specific

target material [61], [70]. In this case, the perovskite crystal structure of LSMO with a pseudo-cubic lattice parameter of 3.889 Å has a similar unit cell size and crystal structure as that of STO with a lattice parameter of 3.905 Å [71], [72]. If the lattice parameter of the target material exceeds that of the substrate, the thin film will experience compressive strain in-plane and tensile strain out-of-plane. The selection of the termination on the STO substrate can significantly influence the physical and chemical characteristics of LSMO film. STO substrates in the [001] direction can exhibit two possible terminations, consisting of alternating layers of SrO and TiO_2 (depicted in Figure 2.3). The literature demonstrates that for achieving a smooth and epitaxial film, a single-terminated substrate is preferable [73]. In bulk, Ti exhibits a coordination number of six, while on the surface, it decreases to five. Conversely, Sr possesses a coordination number of 12 in bulk and eight on the surface. The disparity in coordination numbers implies that the TiO_2 surface is more stable compared to the SrO surface, as fewer atomic bonds are disrupted at the TiO_2 surface. This enhanced stability facilitates smoother film growth and promotes epitaxy. Given that in either case, for the as-received (001)-oriented STO substrate any chemical-based surface characterization can disrupt the material integrity, substrate sonication in organic solvents is carried out to clean the substrate surface.

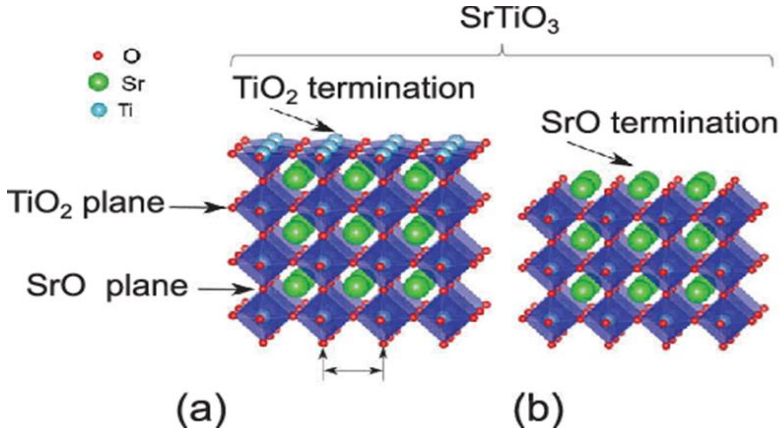

Fig 2.3 Schematic view of $SrTiO_3$ substrate with TiO_2 **(a)** and SrO **(b)** terminations [73].

The deposition process in a PLD chamber is carried out in an ultra-high vacuum condition given an intermediate temperature range from 500 ℃ to 800 ℃. In this setup, laser pulses of varying repetition rates are utilized to generate plasma from the material intended for deposition onto a substrate. Optical lenses guide the laser beam to the surface of the target, with both the target and substrate positioned on rotational holders within a vacuum chamber. Gas and pump valves are integrated into the chamber to regulate the introduction and management of gas background levels. Additionally, a high-energy electron diffraction (RHEED) reflection system can be incorporated into the chamber to monitor the growth process. To initiate film fabrication from the target material, precise focusing of the laser beam onto a small volume of the target is essential. The high energy density of the absorbed laser beam leads to thermal evaporation of the target material, resulting in the creation of vapor. Continuous absorption of laser energy results in the formation of a dense plasma (or plume), comprising of high-energy atomic, diatomic, and other low-mass species from the target material. Collision events within the plume, occurring in proximity, typically a few inches to the target surface, yield a well-oriented plume that is perpendicular to the target surface.

The material deposited onto the substrate retains the composition of the target material by stoichiometric transfer. Notably, the energetic nature of the plume facilitates reactions with the gas environment present in the chamber. Depending on the specific gas introduced, which could include oxygen, nitrogen, or hydrogen, various compounds such as oxides, nitrides, and hydrides can form during the deposition process. Specifically for the complex oxide film, oxygen pressure is set on the order of hundreds of mtorr (~ 300 mtorr for the sample discussed in this thesis) that achieves a desirable O_2 gas species reaction with the ablated material and minimizes oxygen vacancy formation. PLD chambers often allow for the rotation of the substrate to ensure an even

film growth. Following this, the target was also rotated to avoid re-ablating the same region and ultimately avoid particulate formation.

During epitaxial growth using PLD, various growth modes can occur, dictated by the equilibrium of interfacial energies among the film material, substrate, and the atmosphere within the growth chamber. In the process of physical vapor deposition, the material vaporized from the target adheres to the substrate surface. Subsequently, the adatoms diffuse across the surface and aggregate to form clusters. The specific types of clusters formed are contingent upon the equilibrium between the energies at the substrate-atmosphere ($\gamma_{s\text{-}a}$), film-atmosphere ($\gamma_{f\text{-}a}$), and substrate-film ($\gamma_{s\text{-}f}$) interfaces. Describing the film as a droplet allows for the characterization of this energetic equilibrium using Young's equation:

$$\gamma_{f-a}\cos\theta + \gamma_{s-f} = \gamma_{s-a} \qquad \text{(Equation 2.2)}$$

Here, θ represents the contact angle formed by the droplet on the substrate. The degree to which the film material wets the surface, indicated by the value of θ, is influenced by the balance of interfacial energies. When θ equals 0°, the film adatoms fully wet the substrate surface, allowing for either layer-by-layer or step-flow growth modes. These modes illustrated in Figure 2.4 involve the sequential growth of individual monolayers, which is optimal for epitaxial thin film growth. In the layer-by-layer mode, monolayers result from the growth of 2D islands of adatoms that eventually coalesce into a single monolayer. In contrast, during step-flow mode, monolayers may nucleate at steps between atomic planes formed by non-flat substrates, with the growth front advancing away from the step. Conversely, if θ is greater than 0°, adatoms tend to aggregate into islands, leading to a three-dimensional island growth mode. The final growth mode, Stranski-Krastanov growth, commences with layer-by-layer growth near the substrate surface and

transitions to island growth beyond a critical thickness, determined by the epitaxial strain within the film [74].

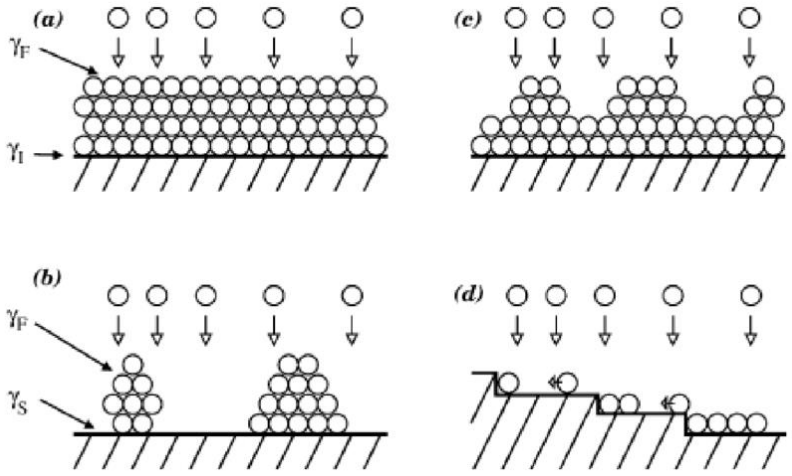

Fig 2.4 Film growth modes in pulsed laser deposition: **(a)** Frank---van der Merwe, or layer-by-layer growth; **(b)** Volmer---Weber, or island growth; **(c)** Stranski---Krastanov, or mixed growth; and **(d)** step---flow growth[75].

Additionally, variations in the laser energy density, also referred to as laser fluence can influence the kinetic energy of the ablated species and their subsequent interaction with the substrate surface, affecting the nucleation and growth mechanisms of the LSMO thin films. If the fluence is insufficiently high, the deposition process will be influenced primarily by partial pressure, hindering the transfer of material in a stoichiometric manner. Conversely, elevating the fluence heightens the probability of particulate emission from the target, potentially leading to the embedding of particulates within the film and consequently diminishing its quality. In the case of LSMO films, a fluence of approximately 1 J/cm^2 produced thin films exhibiting structural and magnetic characteristics in line with previous literature findings. This was confirmed with the XMCD signal

2.2 Micromagnetic Patterning

Following the epitaxial film growth process, the LSMO thin film was subjected to an Ar-ion-implantation-based technique developed by Takamura *et al.* [76] for lithographically patterning arrays of micromagnetic islands of a specified geometry. Figure 2.5 a-d shows a schematic overview of the patterning process.

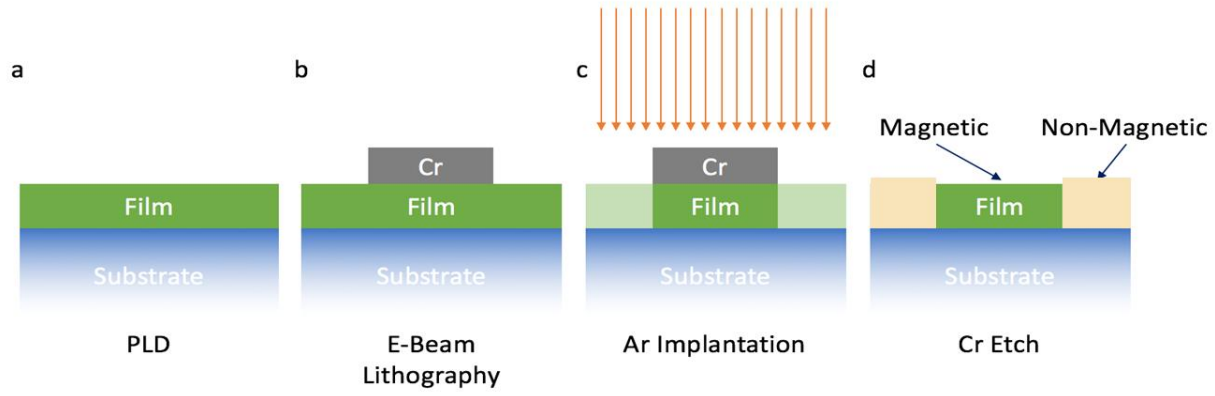

Fig 2.5 Illustration of the Ar ion implantation-based patterning process for perovskite thin films [106]. (a) Perovskite thin film grown via PLD. (b) A hard mask was created atop the thin film using electron beam lithography and lift-off. (c) Flood Ar ion implantation was applied to the entire sample, exposing regions not shielded by the Cr hard mask to the ion flux. (d) Acid-wet etching removes the Cr mask, revealing the protected magnetic perovskite film surrounded by the Ar-ion-exposed film rendered amorphous and non-magnetic.

The process of patterning a PLD-grown oxide sample commences with spin-coating a positive tone resist, ZEP 520 onto the sample surface, followed by employing electron beam lithography to define intricate patterns within the resist. Afterward, the resist is developed, selectively removing the regions exposed to the electron beam in a solution. A subsequent step involves depositing a ~70 nm thick chromium (Cr) layer onto the sample surface via thermal evaporation. Any excess Cr deposited atop the resist is then eliminated through a lift-off cleaning procedure, resulting in the retention of a Cr hard mask bearing the originally defined patterns from electron

beam lithography, as illustrated in Figure 2.5(b). The sample then undergoes argon implantation with a dose of 10^{15} Ar/cm^2 and an energy of 50 keV, effectively rendering any exposed perovskite oxide film amorphous and non-magnetic (depicted as light-yellow regions in Figure 2.5(d)). Notably, regions shielded by the Cr hard mask remain unaffected by the ion implantation (depicted as green regions in Figure 2.5(d)), with the thickness of the Cr layer carefully chosen to prevent Ar ion penetration into the oxide thin film. Finally, the Cr hard mask is removed using an acetic-acid-based wet etching process by using Microchrome Technology's CEA---100 chromium etchant: a blend of 10% acetic acid, 21% ceric ammonium nitrate, and the remainder water. The specific parameters of the Cr mask thickness and implantation energy are optimized for a film thickness of approximately 40 nm.

The ion implantation procedure primarily constrains the resolution of this patterning process. During ion implantation, ions entering the sample collide with the material's atoms, resulting in multiple changes in ion trajectory, a phenomenon known as *straggle*. Consequently, the straggle causes the ion beam to produce an irradiation profile within the material resembling a bulb shape rather than a cylindrical column. As a result, the material beneath the Cr hard mask may incur damage from incoming Ar ions. Predicting the extent of straggle and ion-material interaction is possible through simulations utilizing a software package called Stopping and Range of Ions in Matter (SRIM). Predictive analyses, such as those conducted by Lee *et al.* [60], suggest that implantation-induced defects can propagate approximately 35 nm beneath the Cr mask for a 40 nm thick film. However, in principle, the resolution needed for probing the lateral propagation of defects can be enhanced by utilizing lower implantation energies. SRIM simulations can also aid in determining the optimal Cr mask thickness and implantation energies for films of varying thicknesses. Interestingly, the ion implantation process is likely to cause alterations in the film's

strain states, resulting in changes to magnetization, resistivity, and Curie temperature of LSMO. Atomic force microscopy (AFM) analyses have earlier revealed an expansion of the matrix in comparison to the unpatterned region, estimated at approximately 10 nm or roughly 25% of the original thickness of the film [77]. Notably, the perimeter of the patterned region exhibits an elevated profile, raising the hypothesis regarding the influence of this 'lip' on the strain distribution and magnetic properties in the vicinity of the microstructure's edges.

2.3 Thin Film Magnetism

2.3.1 X-ray Absorption Spectroscopy

X-ray absorption (XA) spectroscopy is a powerful tool for probing the intricate chemical, electronic, and magnetic properties within a sample. In XA spectroscopy, illustrated in Figure 2.6, the quantification of X-ray absorption gauges the sample's absorption cross-section as the photon energy undergoes systematic variation, often facilitated by advanced monochromators employed at a synchrotron source. As the photon energy aligns with the requisite energy threshold to prompt the transition of a core-level electron to a valence-level hole, depicted in Figure 2.6, the sample exhibits a pronounced resonance. These resonant absorptions manifest as discernible peaks within the XA spectrum, their shapes and positions encoding information regarding the chemistry and localized bonding environments inherent to the studied material. Through the analysis of these peak features, XA spectroscopy furnishes an understanding of the fundamental electronic structures underpinning the material's properties.

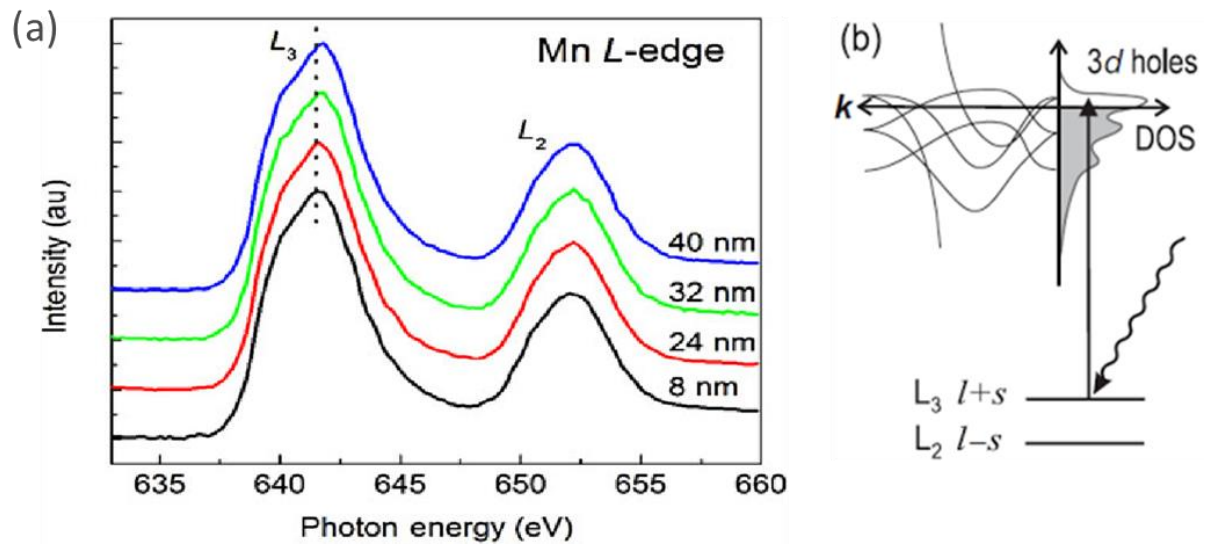

Fig 2.6 (a) Mn *L*-edge XA curves of LSMO films with different thicknesses [78]. **(b)** Schematic of an x-ray-induced excitation of a core-level electron into an empty 3*d* valence state. Adapted from Ref. [79].

In the investigation of 3*d* transition metal oxides conducted in this thesis, a strong absorption signal is discerned via the electronic excitation from the 2*p* to 3*d* energy levels, commonly referred to as the *L*-edge transition and notably observed within the soft X-ray photon energy spectrum, typically spanning from 400-1000 electron volts (eV) [80]. Among the several mechanisms exploiting X-ray-induced electronic excitations in XA spectroscopy, a set of methods exists to quantify the absorption signal. Each mode offers distinct insights into the relaxation mechanisms following electron excitation, crucial for understanding the properties of a 3*d* transition metal perovskite. Notably, in the total electron yield (TEY) mode, the secondary electrons emitted from the sample due to X-ray excitation are detected. This mode provides a comprehensive view of the electronic structure and surface sensitivity, making it particularly useful for probing the topmost layers (the top 5-10 nm of the sample as limited by the electron escape depth) of the material and is relevant to the work done in this thesis. Upon excitation, electrons are promoted to higher energy states, leaving behind core-level holes. The relaxation process involves the recombination of these excited

electrons with the core-level holes, releasing energy in the form of Auger electrons or secondary electrons. The detection of these emitted electrons in TEY mode allows for the characterization of the relaxation dynamics and electronic transitions occurring within the material [81].

In this study, synchrotron X-rays were harnessed from undulator insertion devices with sophisticated arrangements of permanent dipole magnets arranged along track-like structures within synchrotron storage rings. These undulators induce electron beam undulation, thereby stimulating the emission of X-rays. Fine-tuning of photon energy and polarization is achieved through adjustments in the gap size between undulator tracks and the phase between dipole structures. Subsequently, the emitted X-rays traverse a series of monochromators, focusing mirrors, and apertures before reaching the experimental end stations. Specifically, this research utilizes soft x-rays from the Advanced Light Source (ALS), at via undulator beamlines (BL) 4.0.2 for x-ray magnetic circular dichroism (XMCD) spectroscopy, and BL 11.0.1.1 for x-ray photoemission electron microscopy (X-PEEM), as elaborated in subsequent sections.

2.3.2 X-ray Magnetic Circular Dichroism

X-rays possess the ability to be polarized, exhibiting right-circular/left-circular (RCP/LCP), or linear polarization. When exposed to RCP/LCP X-rays, which possess opposing angular momentum, an electron of a specific spin absorbs the momentum. Each polarization yields a distinct spectrum, and the disparity between these spectra constitutes the XMCD spectrum. This spectroscopic technique is particularly invaluable for probing the magnetic properties of materials such as LSMO at the Fermi level [82]. Depicted in Figure 2.7 is a schematic representation of an XMCD spectrum in conjunction with XA measurements.

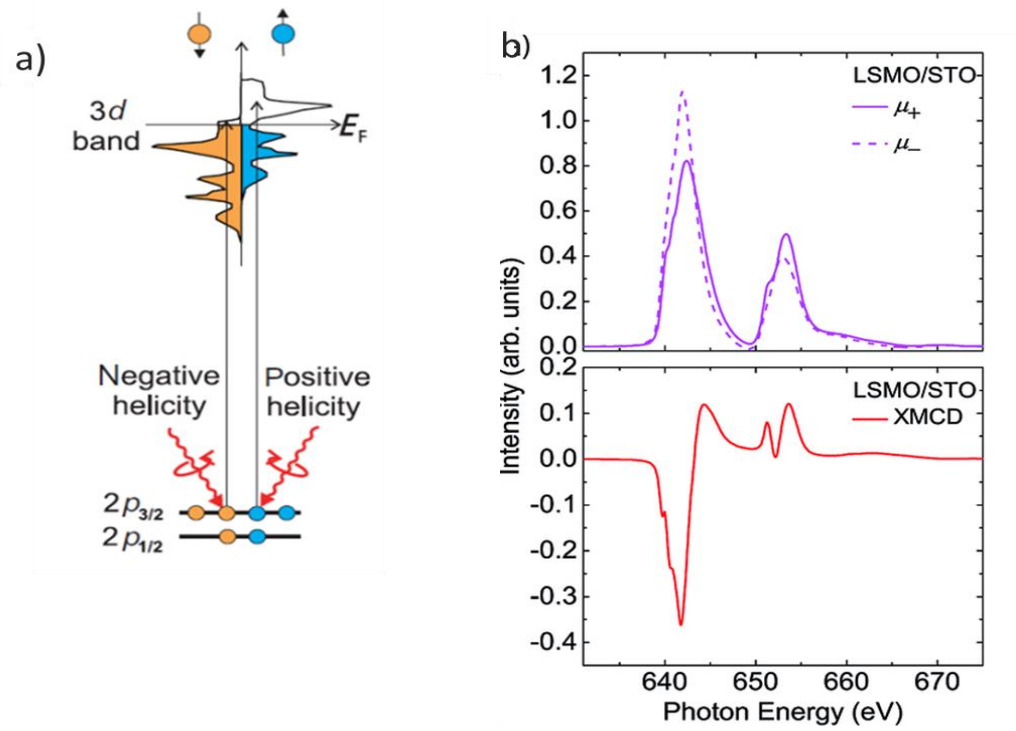

Fig 2.7 (a) Schematic of the circular-polarization-dependent electron excitation for a given example of the 2*p* core level to 3*d* valence states transition [83]. **(b)** XA and XMCD spectra of Mn at *L* edge for an LSMO/STO film at 80 K. The dichroism is given $\Delta\mu = \mu+ (LCP) - \mu-(RCP)$ [84].

XMCD was first applied to ferromagnetic domain imaging in a pioneering work in 1993 (Stohr. *et al.* [85]). The strength of the XMCD signal, represented by I_{XMCD}, in a magnetically saturated (i.e., magnetized with an external field) isotropic system, follows a scaling law given by,

$$I_{XMCD} \propto \boldsymbol{m}\cos\theta \qquad \text{(Equation 2.3)}$$

where θ denotes the angle between the X-ray beam and the magnetic moment $\boldsymbol{m}$, with m representing its magnitude. This mathematical relationship underscores how the XMCD signal reflects the net magnetic ordering within the region probed by the X-ray beam. Maximum XMCD signal occurs when the sample's magnetization aligns parallel or antiparallel to the X-ray helicity. The relationship between the two peaks observed in the XMCD spectrum is governed by sum rules in the illustration of Figure 2.8, establishing a connection between the area encompassed by the L_3

and L_2 XMCD regions. This connection is contingent upon the magnitude of the system's spin (m_s) and orbital (m_o) moments.

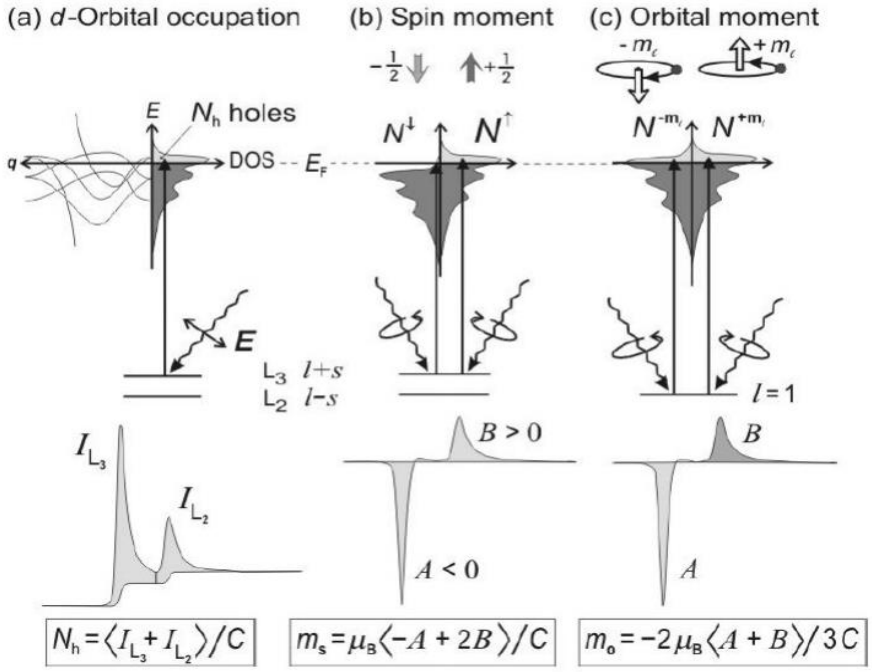

Fig 2.8 A summary of XA/XMCD sum rules for a **(a)** density of state and spectral detail states shown at Fermi level given by **(b)** spin moment sum (m_s) and **(c)** orbital moment sum (m_o). Adapted from Ref. [86]

Consequently, XMCD spectroscopy experiments typically involve the application of a saturating magnetic field, such as in the case of LSMO where H_c is approximately 50 Oe [56]. XMCD serves a dual role, facilitating both spectroscopic and magnetometric measurements of a sample, as its signal strength depends on the net magnetization. The distinctive line shapes observed in XMCD spectra provide insights into the elements and their valence states that contribute to magnetism. By combining XA and XMCD measurements, a correlation is established between the electronic structure of the material with its magnetic behavior. The XA spectrum offers insights into the valence states and bonding configurations of the atoms, while the XMCD spectrum reveals the magnetic ordering and spin orientations within the material.

2.3.3 X-ray Photoemission Electron Microscopy

At the intersection of spectroscopy and microscopy lies the need to delve into the spatial features of sample chemistry and magnetic ordering. While spectroscopy offers valuable insights, its information is spatially averaged over the region illuminated by the X-ray beam. Microscopy techniques come into play to unlock these spatial variations within a sample, and one such powerful method is X-ray photoemission electron microscopy (X-PEEM). Functioning as a *photon-in electron-out* technique, X-PEEM employs an electron microscope to visualize the spatial distribution of electrons emitted from a sample under the influence of monochromatic X-rays. This technique utilizes different contrast mechanisms depending on the wavelength of the radiation, offering insights into the elemental and chemical composition, as well as the electronic and magnetic properties of the material including any heterogeneity. One of the key applications of X-PEEM is magnetic domain imaging, which exploits strong X-ray magnetic dichroism effects, particularly at the *L* edges of magnetic 3*d* transition metals like Cr, Mn, Fe, Co, and Ni. X-PEEM facilitates the imaging of spatial variations in the TEY emission across the sample surface. Essentially, the observed contrast in X-PEEM images corresponds to the XA and XMCD signals, with additional contrast stemming from sample topography and variations in work function across the surface. X-PEEM stands out among other magnetic imaging techniques due to its surface sensitivity and element specificity, making it well-suited for investigating ultra-thin magnetic films, multi-layers, and alloys and not just limited to studying crystalline samples [87]. Unlike some high-resolution magnetic imaging techniques, X-PEEM is also sensitive to antiferromagnetic order when linearly polarized x-rays are used . With a typical spatial resolution of about 50–100 nm for magnetic domain imaging, X-PEEM bridges the gap between Lorentz imaging in transmission electron microscopy and optical techniques such as magneto-optic Kerr microscopy.

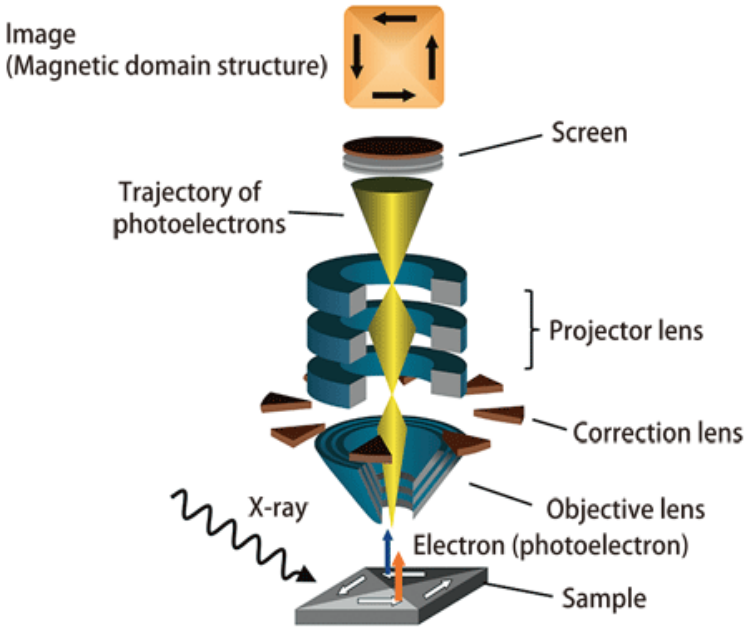

Fig. 2.9 Principle of X-PEEM microscope. Adapted from Ref. [88]

A schematic representation of an X-PEEM microscope is illustrated in Figure 2.9. The contrast mechanism in X-PEEM is a multifaceted interplay of energy-dependent electron emission, sample properties, and sophisticated instrumentation. In addition to energy-based contrast mechanisms, X-PEEM benefits from advanced electron optics. Strong electric fields between the sample and the first microscope lens accelerate emitted electrons, which are then guided and magnified by a series of electrostatic or magnetic lenses. The back focal plane apertures serve a dual purpose: limiting the angular spread of transmitted electrons and acting as energy filters to minimize chromatic and spherical aberrations. These optics, combined with deflector and stigmator elements, ensure precise control over the electron beam, correcting for any mechanical misalignments and optimizing image quality. The contrast in X-PEEM is further enhanced by exploiting variations in the efficiency of electron emission across different regions of the sample. This efficiency can be influenced by factors such as local chemical composition, electronic states,

surface morphology, and magnetic properties. Moreover, the spatial resolution of X-PEEM is greatly influenced by the sampling depth of emitted electrons, which correlates with the mean free path of low-energy electrons within the material. This sampling depth enables the probing of surface structures and interfaces with exceptional detail, making X-PEEM utilization a force to reckon with for magnetic domain imaging and domain analyses presented further in Chapter 4.

PEEM microscopes operate in three primary modes: (i) full-field imaging, (ii) local spectroscopy, and (iii) spectromicroscopy. Full-field imaging captures images at a fixed photon energy, offering an overview of the sample's surface. Local spectroscopy scans photon energy to acquire XA spectra in specific regions, utilizing X-PEEM's spatial resolution. Spectromicroscopy expands local spectroscopy to gather stacks of images across photon energies, forming a three-dimensional dataset, and integrating spatial and energy dimensions for comprehensive analysis of the sample's properties. For the LSMO sample, multiple X-PEEM images are captured while incrementally adjusting photon energy (approximately 0.2 eV steps) across the Mn L_3 edge, exhibiting a strong XMCD signal. The X-ray's energy is then optimized for maximum XMCD signal strength, typically around 0.2 eV lower than the XA peak. At this fixed energy, X-PEEM images are acquired alternately with RCP and LCP. To isolate the XMCD signal, an asymmetry calculation is performed using the formula,

$$I_{XMCD} = I_{RCP} - I_{LCP} / I_{RCP} + I_{LCP}, \quad \text{(Equation 2.4)}$$

where I_{RCP} and I_{LCP} represent intensities measured with RCP and LCP, respectively. This operation is depicted in Figure 2.10 to contextualize imaging of domain patterns using X-PEEM.

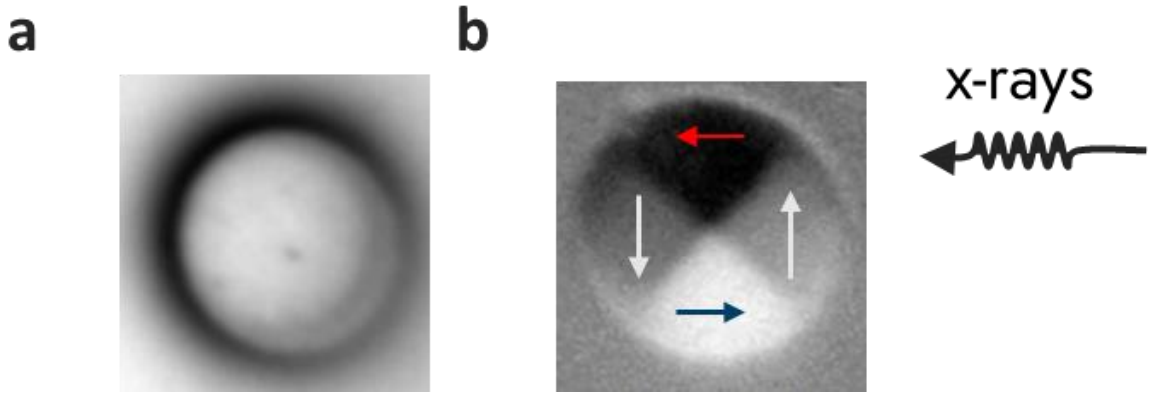

Fig 2.10 Principle of X-PEEM imaging done on an LSMO disc-shaped micromagnet with a diameter of 2 μm at 32 K. (a) X-PEEM image of the micromagnet captured using circularly polarized x-rays (b) XMCD-PEEM image calculated from the asymmetry equation showing contrasts in magnetic domains. The schematics depict the direction of x-rays relative to the orientation of magnetic moments with black/white/grey contrast corresponding with parallel (red arrow)/antiparallel (blue arrow)/ perpendicular (white arrows) directions respectively [60].

2.4 Micromagnetic Simulations

Micromagnetic simulations serve as computational tools for modeling magnetic systems with characteristic spin textures by a continuum approximation of magnetic moments. These simulations are facilitated by versatile software packages like Object-Oriented Micromagnetic Framework (OOMMF) and MuMax^3 [34], utilized in this thesis. Within these simulations, effective magnetic moments are approximated within user-defined unit cells or cuboids, considering their interactions with their six nearest neighbors. The process of magnetic relaxation is characterized by torque values derived from the Lifshiz-Landau-Gilbert framework [89], notably the Landau-Lifshitz torque, which accounts for the rotational dynamics of magnetic moments influenced by external fields, magnetostatic effects, exchange interactions, and thermal fluctuations. The iterative solution to the time-dependent equation of motion for a magnetic moment under an effective magnetic field is given by,

$$\partial \boldsymbol{M} \; \partial t = \gamma \boldsymbol{M} \times \boldsymbol{H}_{eff} - \alpha\gamma \; M_{sat} \; (\boldsymbol{M} \times (\boldsymbol{M} \times \boldsymbol{H}_{eff})) \qquad \text{(Equation 2.5)}$$

where γ is the gyromagnetic ratio, α is the empirical Gilbert damping parameter, and H_{eff} is the effective field encompassing different magnetic energy contributions from the exchange and magnetocrystalline anisotropy terms (H_{ex} and H_{MCA}, respectively). The first term represents the precessional motion of $\boldsymbol{M}$ under a magnetic field while the second represents the damping of the $\boldsymbol{M}$ precession (i.e., a tendency for $\boldsymbol{M}$ to eventually reach its equilibrium orientation). Micromagnetic features undergo relaxation under zero-field conditions, employing numerical methods such as the GPU-accelerated Runge-Kutta (RK) solver [90]. Spin texture modeling is parameterized by film thickness, geometric shape of the sample, saturation magnetization (M_S), magnetocrystalline anisotropy constant (K_1), and exchange stiffness constant (A_{Ex}). The output of micromagnetic simulations manifests as a three-dimensional vector field representing the magnetic configuration of the system, amenable to further analysis and manipulation. It is often facilitated through tools such as Python programming language or MATLAB. Simulations discussed in section 3.2.4 and 4.2 are specifically performed with an RK45 MuMax solver (or the Dormand-Prince method) offering a robust 5th-order error convergence.

2.5 Summary

The chapter describes the various experimental and computational techniques that govern the results of this investigation into micromagnetic domain textures of LSMO thin film. Chapters 3 and 4 provide further scientific analysis into their magnetic behavior and theoretical insights formed from applying quantitative methods to these magnetic domain textures.

Chapter 3: LSMO Non-edible Micromagnetic 'Donuts'

Exploring material systems for spintronics (detailed in Chapter 1) presents a fascinating tapestry of magnetic research and investigations into magnetization dynamics, topology, and emergent phenomena. Our capability to fashion these magnetic systems into micro/nanoscale structures gives an impetus to develop novel functionalities and drive the growth of magnetic memory. One such intriguing aspect of studying these microstructures is the unraveling of *chiral* magnetism at the nanoscale [91]. Chirality, characterized by the handedness of a spin texture, holds profound implications for magnetic phenomena, ranging from stability and dynamics to information encoding and functionality in spintronic devices as the spin moments form a flux enclosure. In particular, the presence of a vortex core within disc-shaped micromagnets, encapsulating a chiral spin configuration (Figure 3.1) offers unique opportunities in stable information encoding, dynamic manipulation, interaction studies, and sensor applications.

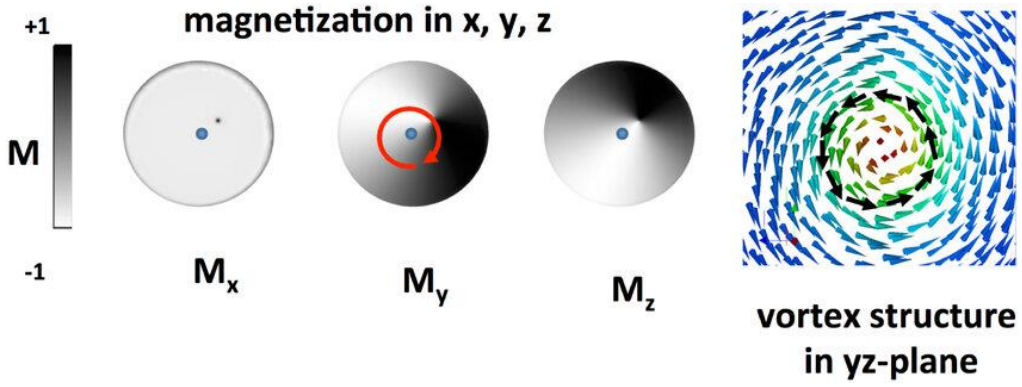

Fig. 3.1 Micromagnetic simulations of a vortex structure gyration outside the point contact area in a nano-pillar device [92].

Several research investigations have shed light on vortex core dynamics by engineering disc or circular micromagnets, since the groundbreaking work of Cowburn and Welland [93] on 'circular dots' of permalloy ($Ni_{80}Fe_{20}$) with a diameter ranging from 0.3 to 1 μm and 50 nm thickness.

Seminal studies by Novosad *et al.* [94] and Buchanan *et al.*[95] regarding vortex dynamics and chirality in magnetic nanostructures channeled a domino effect to the systematic research of vortex core dynamics, including precession, gyration, and manipulation through external fields like temperature or electric field [96], [97]. The core itself typically exhibits an out-of-plane orientation, termed *polarity*, where the magnetization points perpendicular to the plane of the material and is depicted in Figure 3.2. This perpendicular orientation can either be pointing upwards (as shown in Figure 3.2) or pointing downwards and lead to two different polarities in addition to the clockwise and counterclockwise chirality of the vortex structure, leading to four distinct states.

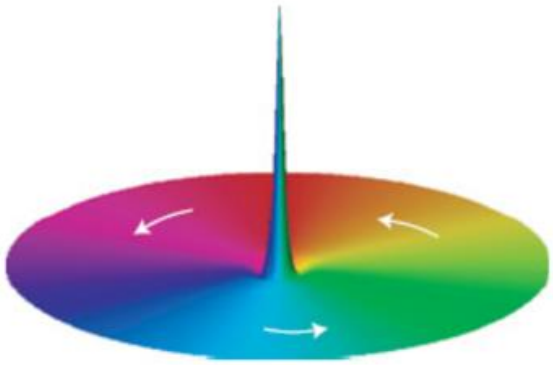

Fig 3.2 A vortex core orientation with an out-of-plane polarity. The electron spins in a magnetic vortex—clockwise or counterclockwise (depicted here with arrows). These polar orientations could form the units of multibit magnetic storage and spintronic systems.

3.1 Domain Structure in LSMO-based Micromagnets

Now imagine going a step further and being motivated by a 'donut'. Creating micromagnetic structures in the shape of a donut is an intriguing study of chiral magnetism. The principle here is to physically remove the vortex core region in an otherwise circular magnet and observe the spin texture formation. This thesis elucidates the exhibition of chiral magnetism at the nanoscale in the

absence of a vortex core in a 100-unit cell (40 nm) thick LSMO thin film patterned with circular micromagnetic islands with varying inner hole diameter (ID), which I will, hence, refer to as LSMO donuts. Quantitative image analysis of spin textures imaged with XMCD-PEEM is correlated with micromagnetic simulations performed using MuMax[3] to extract local magnetic parameters - specifically, K_1 constant and understand MCA energies.

3.1.1 Motivation

Previous magnetic investigations carried out by Dr. Michael Lee and Dr. Thomas Wynn from the Takamura Research Group looked into magnetic spin textures in LSMO micromagnets in a set of geometrical shapes: squares, diamonds, and circles with a 2 μm edge length/diameter [60]. The domain structure evolution in the various geometries was contingent on a delicate balance between magnetic energies, influenced by both shape and magnetocrystalline anisotropy, discussed further in Section 3.1.2. The spin textures were investigated over a range of temperatures (from 32 K to 230 K, all being below T_c) achieved at the PEEM3 end station, as shown in Figure 3.3. Square micromagnets, characterized by their edges parallel to the magnetic easy axes, adopt 'Landau' flux closure domain patterns, where magnetic moments align parallel to these edges. The diamond micromagnets have their edges oriented along the magnetic hard axis, and they display an evolution of the spin textures with decreasing temperature. At 230 K, the domain patterns adopt a Landau flux closure domain pattern with their magnetizations parallel to the edges of the micromagnets, causing an additional energy MCA term to be considered. Due to the X-PEEM measurement geometry which only offers sensitivity to magnetization parallel to the helicity vector of the x-rays, the two upper/lower domains appear with the same image contrast. As the temperature decreases, an additional Landau pattern emerges in the center of the micromagnet, this time with the magnetization parallel to the magnetic easy axes, forming a pattern with two

concentric Landau patterns rotated by 45° relative to one another. The circular micromagnets notably, have their edge contours guiding magnetic moments into a vortex structure The shift from vortex to Landau patterns as temperature decreases is indicative of the temperature sensitivity of micromagnetic structures and, more importantly, the balance between shape anisotropy energy and its MCA energy.

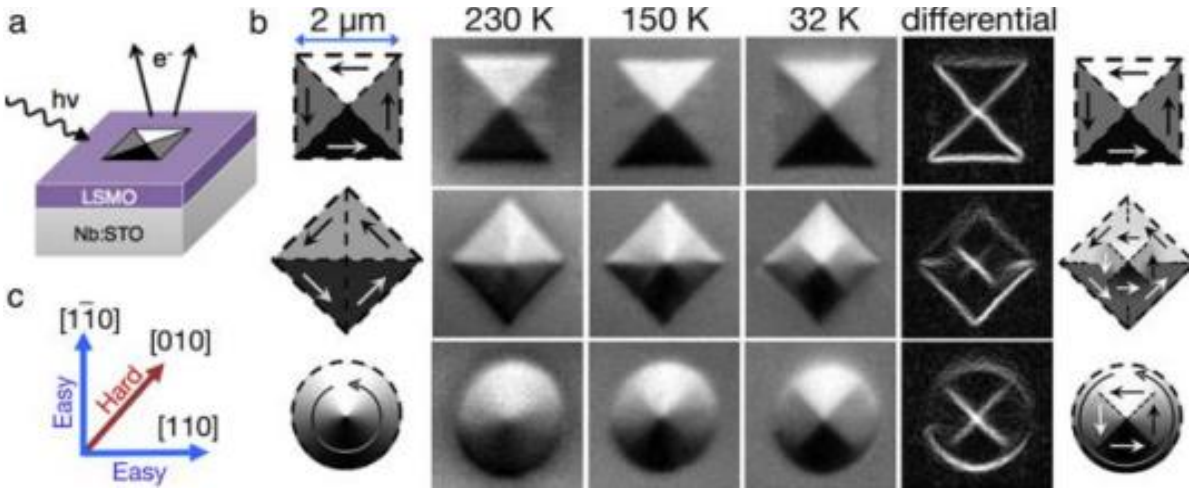

Fig. 3.3 Magnetic domain images of patterned micromagnets [60]. (a) Experimental setup of the PEEM3 microscope. Incident radiation is aligned with the [110] easy axis of the LSMO thin film (b) Temperature-dependent XMCD-PEEM images of the magnetic domains in square, diamond, and circular micromagnets. Contrast is normalized in all images/temperatures to better observe domain structure evolution. Differential images highlight domain boundaries of the domain images acquired at 32 K. Schematics indicate the direction of magnetic moments within the domains. (c) Orientation of the magnetic easy and hard axes of the LSMO thin film.

This study presents key takeaways from the spatial variation in fundamental magnetic parameters, such as magnetocrystalline anisotropy, significantly impacting domain patterns throughout the micromagnets, and emphasizing the importance of accurate modeling of spin textures. Results incorporated in this thesis are motivated by the experimental and theoretical insights of Lee *et al.* particularly, the crucial role of 'edge effects' where shape anisotropy dominates at the perimeter

of circular micromagnets, and magnetocrystalline anisotropy in determining the spin textures of LSMO donuts.

The micromagnets investigated in this study, measuring 2 μm in edge length/diameter, occupy a critical size range [98], [99]. Here, the conditions are such that the injection of new domain walls leading to the formation of more complex multidomain states is inhibited. Despite this constraint, these micromagnets still offer ample size for the observation of nuanced details within the domain structure, attributed to a unique balance between magnetostatic and MCA energies. Previous research has shown that for micromagnets with smaller dimensions (e.g., 500 nm wide), whether they are patterned in LSMO or composed of metallic magnetic structures, the resulting domain patterns are primarily dominated by shape anisotropy regardless of shapes such as square, diamond, or circle [100], [101]. Further, I will focus on the spin texture analysis of LSMO donuts at an intermediate temperature of 110 K for two reasons: firstly, a gradual development of the inner vortex pattern can be seen at an intermediate temperature regime for a circular micromagnet geometry consistent with LSMO donuts, and secondly, accounting for the experimental limitations of the PEEM3 end station when cooling with liquid nitrogen.

3.1.2 Experimental Geometry

PLD growth and micromagnetic patterning of the single-layer LSMO thin film were performed by Dr. Dayne Y. Sasaki according to the experimental descriptions provided in Sections 2.1 and 2.2 of Chapter 2. X-PEEM images were acquired using the principle of XMCD at a photon energy corresponding to the maximum XMCD signal at the Mn L_3 edge of the film. The orientation of the X-rays differs from the experimental geometry used by Lee *et al.* in that they are incident along the [100] direction, making an angle of 30 ° with the sample surface. Due to differences in the

samples, the in-plane <100> directions appear to be magnetic easy axes in the case of the circular LSMO donuts for reasons that are not entirely clear. Domain imaging was performed at 110 K following thermal demagnetization of the sample in the PEEM3 chamber which is shielded from any external magnetic field. The final domain contrasts are obtained using the asymmetry equation 2.4 on the XA images acquired with right/left circularly polarized X-rays. Figure 3.4 illustrates this experimental geometry with a circular LSMO micromagnet (white dashed line depicting the perimeter) where the black/white/grey contrast corresponds to the parallel/antiparallel/ perpendicular alignment of magnetic moments to the direction of X-rays and constituting the domain patterns. The resulting contrast from X-PEEM shows distinctive magnetic domain patterns like a "vortex" (blue arrow), discussed further in Section 3.1.4,

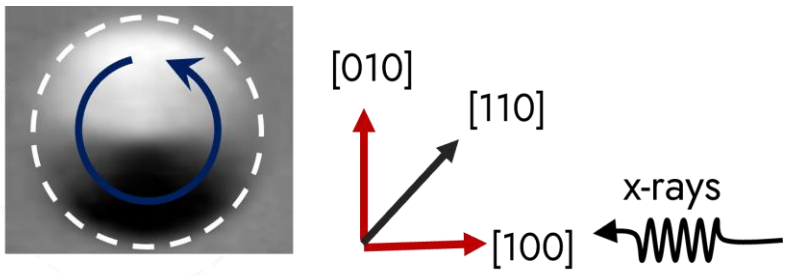

Fig. 3.4 Illustration of a vortex pattern in a single layer LSMO (40 nm) disc-shaped micromagnet with a diameter of 2 μm imaged using X-PEEM at 110 K. Experimental geometry on the right shows X-rays along the [100] direction with a 30 ° canting angle.

3.1.3 Magnetocrystalline Anisotropy

In this section, I take a step back to discuss magnetic energy considerations that influence domain formation as observed in the sample. *Magnetocrystalline anisotropy* refers to the preferential alignment of magnetic moments in a material along certain crystallographic directions or axes. The origin of magnetic 'domains', regions within a magnetic material where the magnetic moments are aligned parallel to one another, is a consequence of balancing magnetic energies in

the system. Thermodynamically, the formation of magnetic domains seeks to minimize the total energy of the system. This energy minimization involves balancing various energy terms that represent different atomic-scale magnetic phenomena. In essence, magnetic anisotropy arises due to the interplay of multiple factors such as exchange interactions, dipole-dipole interactions, and crystal structure. These factors dictate the preferred orientation of magnetic moments within the material, leading to the formation of magnetic domains. The total energy E_{total} of a magnetic system can be expressed as the sum of various energy terms, including exchange energy $E_{exchange}$, magnetocrystalline anisotropy energy (MCA) E_{MCA}, and dipole-dipole interaction energy dipole E_{dipole}:

$$E_{total} = E_{exchange} + E_{MCA} + E_{dipole} \quad \text{(Equation 3.1)}$$

$E_{exchange}$ arises from the interaction between neighboring magnetic moments and typically favors parallel alignment of neighboring spins. E_{MCA} originates from the anisotropic nature of the crystal lattice, which prefers that the magnetic moments lie along certain crystallographic directions over others. It is represented by terms in Hamiltonian that depend on the crystal structure and symmetry. E_{dipole} energy arises from the dipolar interaction between magnetic moments within the material. It depends on the distance between magnetic moments and their orientation relative to each other. Additional terms such as Zeeman energy (interaction with external magnetic field) or magnetoelastic energy (interaction with mechanical strain) may also be included in the total energy equation [102]. Overall, the total energy of the magnetic system reflects the balance between these various energy contributions, governing the material's magnetic behavior.

MCA energy elucidates the propensity of magnetic moments within a material to align preferentially along specific crystallographic directions (referred to as easy axes). This

phenomenon arises due to the inherent symmetry of the crystal lattice, which imposes energy minima along certain orientations, thus influencing the overall magnetic behavior of the material. Mathematically, E_{MCA} is expressed as an integral over the volume of the material, encapsulating the interactions between magnetic moments ($\boldsymbol{m}$) and the crystallographic anisotropy directions ($c1$, $c2$, $c3$). For cubic systems such as in bulk LSMO, the easy axis is along <100> directions. In cubic crystal thin films of LSMO under small tensile strain as found when grown on STO substrates, the expression for MCA energy takes the form:

$$E_{MCA} = K_1 \int [(\boldsymbol{c}1 \cdot \boldsymbol{m})^2 (\boldsymbol{c}2 \cdot \boldsymbol{m})^2 + (\boldsymbol{c}1 \cdot \boldsymbol{m})^2 (\boldsymbol{c}3 \cdot \boldsymbol{m})^2 + (\boldsymbol{c}2 \cdot \boldsymbol{m})^2 (\boldsymbol{c}3 \cdot \boldsymbol{m})^2] \, dV \qquad \text{(Equation 3.2)}$$

The MCA constant, K_1, is a key parameter quantifying the strength of this preference. This constant encapsulates the energy associated with aligning magnetic moments along the easy axes, effectively penalizing deviations from this preferred alignment. Consequently, materials with higher K_1 values exhibit stronger magnetic anisotropy, emphasizing the importance of this parameter in characterizing magnetic materials. It's worth noting that higher-order anisotropy terms (e.g., involving constants K_2, K_3, etc.) may be included for more intricate systems like low-symmetry non-cubic systems or in the case of thermal fluctuations affecting anisotropy energies. However, these terms are often negligible in cubic materials.

With regards to the shape of a magnetic entity, another anisotropy phenomenon must be taken into consideration stemming from the geometry or morphology of the material itself. This phenomenon, known as *shape anisotropy,* manifests when the shape of a magnetic entity, such as a nanoparticle or thin film, imposes energetic preferences on the alignment of its magnetic moments. Unlike MCA, which is quantified by K_1 and is intrinsic to the crystalline system, shape

anisotropy is typically quantified based on the demagnetization factor, which depends on the geometry of the magnetic entity. The demagnetizing factor, denoted by *n*, is a parameter that quantifies the influence of the shape of a magnetic body on its internal magnetic field. The term 'demagnetizing field' highlights this field's tendency to reduce the specimen's overall magnetic moment.

Calculating the demagnetizing field for objects with arbitrary shapes can be quite a challenge, even with a uniform magnetizing field. Hence, certain strategies are used to deal with this calculation. For instance, one approach is to minimize the demagnetizing field by using a very long sample or, more commonly, a ring-shaped sample. If the sample has an ellipsoidal shape and assumes uniform magnetization, the demagnetizing field can, in principle, be calculated. However, since ellipsoidal samples are difficult to produce, simpler shapes like rods or disks are often approximated as ellipsoids. The next step is to measure the magnetic field as close to the surface of the sample as possible. Since the tangential component of the field does not change across the surface, this measurement provides the true field acting on the sample, including the demagnetizing field. Experimentally determining the demagnetizing field involves using a sample with the same shape as the actual sample but made from a material with negligible coercivity. For such a sample, the demagnetizing field is equal and opposite to the applied field, and the magnetization varies linearly with the applied field. The slope of this line is inversely proportional to *n*, which remains consistent for all samples of the same shape.

Consequently, deviations from these preferred configurations incur energy penalties associated with the 'magnetostatic energy' or contributions from external stray fields. Magnetostatic energy E_{ms} determined by an integral over the volume V of the magnet is quantified by the expression:

$$E_{ms} = -\tfrac{1}{2}.\ \mu_0 M_{sat}\ n\int \boldsymbol{H_s}\cdot\boldsymbol{m}\ dV \qquad \text{(Equation 3.3)}$$

Here, M_{sat} is the saturation magnetization of the material, $\boldsymbol{H_s}$ is the magnetization field applied, m is the local magnetization vector within the material, μ_0 is the vacuum permeability. The demagnetization factor, *n, accounts* for the effect of the material's shape and geometry on its magnetization behavior. In principle, a single-domain magnetic structure would have a north and south magnetic pole because of the divergence of the magnetization $-\nabla\cdot\mathbf{M}$. Following the pole-avoidance principle [103], and as discussed in the preceding passages, an internal demagnetizing field would counter the magnetization of a material. The geometric constraints imposed by the material's shape lead to preferred magnetization orientations within domains, for minimizing energy. Certain geometries may favor specific arrangements of magnetic domains.

The boundary region between two magnetic domains with different orientations of an order parameter (such as m) is defined as a magnetic domain wall, where the magnetic moments gradually rotate their orientation. The formation of domain walls includes a domain wall energy factor in addition to MCA, which takes into account penalties of exchange energy (since adjacent moments are not parallel to one another) and MCA (as the moments are not aligned along the magnetic easy axes). These domain walls are an essential feature of Landau patterns such as those observed in the micromagnets at low temperatures. The exchange energy arises from the quantum mechanical exchange interaction, which tends to align neighboring magnetic moments parallel or anti-parallel to each other to minimize the system's energy. Exchange energy (E_{ex}) promotes the widening of domain walls because it prefers adjacent magnetic dipole moments to align as closely to parallel as possible whereas MCA tends to form narrow domain widths. Further, by penalizing configurations that lead to an increased 'stray field' production (like those shown in Figure 1.12),

shape anisotropy underscores the importance of considering the geometric properties of materials when analyzing their magnetic behavior.

The emergence of spin textures within demagnetized systems, particularly LSMO micromagnets given in this thesis signifies the balance achieved between various energetic considerations described in the preceding paragraphs, ultimately leading to the attainment of (meta)stable states the vortex state depicted in disk-shaped microstructures (refer to Figure 3.3) [60]. The formation of these spin textures in "flux-closure" domain configuration, results from the optimization of magnetic moments along the perimeter of the patterned feature to minimize the creation of magnetic poles compared to a uniformly magnetized disk. Despite incurring an energy penalty from E_{ex}, the reduction in stray field production (E_{ms}) associated with flux-closure domains may offset this penalty. Here, the core of these spin textures experiences significant moment misalignment, often pointing out of the disk plane to minimize local E_{ex}. The out-of-plane orientation of the core shown in Figure 3.2 (referred to as polarity), and the direction of magnetization rotation within the vortex/Landau spin textures (termed chirality), further characterize these structures. The presence or absence of significant magnetocrystalline anisotropy dictates the preference for either texture. For instance, a negligible K_1 favors the formation of a vortex spin texture in disk-shaped circular micromagnet (Figure 3.5), while a significant K_1 leads to a Landau state to maximize alignment with easy axes while minimizing E_{ms}.

Regarding the altered magnetic easy axes in the case of LSMO donuts, the strain state imposed by the substrate and the matrix can play a critical role in influencing the spatial variation of MCA in magnetic materials. When strain is introduced by the surrounding matrix (most likely with the ion implantation technique), there is a possibility of altering the lattice parameters which in turn affects

the direction and magnitude of MCA. This relationship is particularly pronounced in epitaxial thin films, where strain is non-uniformly distributed due to factors like lattice mismatches or any thermal expansion differences between the film and substrate. The spatial variation in strain leads to a corresponding variation in magnetocrystalline anisotropy. This phenomenon can lead to the introduction of "stress anisotropy", which refers to the phenomenon where the mechanical stress experienced by a material varies in different directions. In other words, the stress is not uniform or isotropic throughout the material but exhibits directional dependence and, thus, potentially altered strain states. This effect is pronounced in materials like $Y_3Fe_5O_{12}$ (YIG), where strain-induced lattice distortions shift the balance between in-plane and out-of-plane anisotropy, resulting in a tunable MCA that is crucial for optimizing the performance of spintronic devices [104]. The ion-implantation process used in this research is attributed to the introduction of this strain as the lattice swells upon irradiation. The vertical swelling of the lattice is observed by the height difference between the implanted matrix and magnetic feature, but the impact in the lateral direction is more difficult to probe. This lateral strain is likely to differ at the inner or outer perimeter of the donuts. Hence, extracting the spatial variation of MCA across the magnetic material is useful in correlating the magnetic behavior of the LSMO donuts and gathering insights about the switching of the easy axis.

3.1.4. Single and Complex Vortex Phenomena

XMCD-PEEM imaging of domain patterns in the LSMO donuts showcases unique chiral spin textures brought about by the delicate balance of the material's magnetic energies. Figure 3.5 depicts LSMO donuts with inner hole diameters (ID) varying from 0.2 μm to 1 μm with schematics depicting the orientation of magnetic moments in a single vortex pattern with both left-handed (red

arrow) and right-handed (blue arrow) chirality. The appearance of both chirality in the micromagnets is attributed to a random order of the demagnetized sample's magnetization.

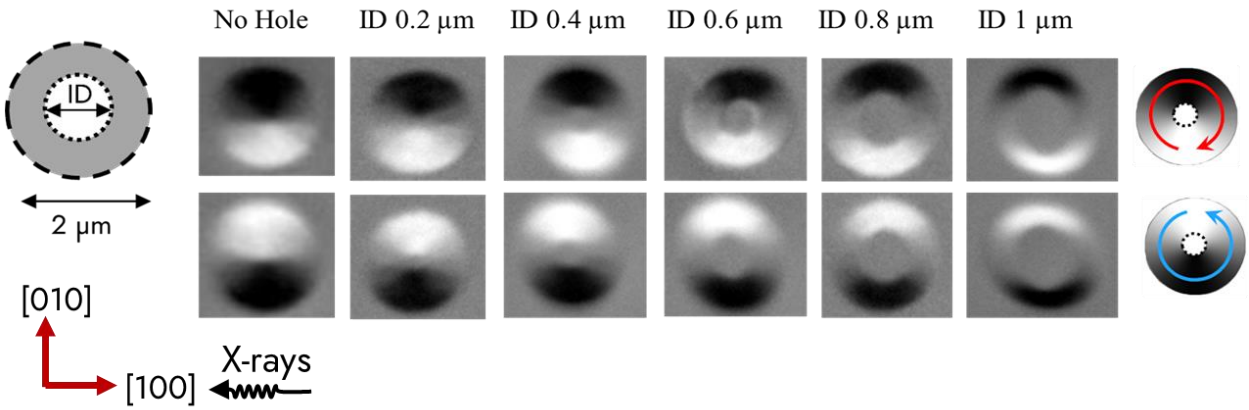

Fig. 3.5 X-PEEM images of patterned LSMO circular micromagnets with an ID varying between 0.2 - 1 µm and an outer diameter of 2 µm acquired at 110 K. The top and bottom panels show chiral domain patterns elucidated by domain contrasts with chiral orientations in color-coded schematics.

Schematic representation of the orientation of the domains in the donuts is similar to a prominent vortex texture that Lee *et al.*'s work observed for the circular micromagnets. The domain images for the donuts indicate easy axes along the <100> directions unlike <110> that were observed for the sample investigated by Lee *et al.* Figure 3.6 shows an example of four LSMO donuts with ID = 0.4 µm which display a distinctive spin texture with many more features than observed with the single vortices shown in Figure 3.5. (center panel). As with the single vortices, these complex spin textures (referred to as the 'screwhead' domains), display two types of chirality.

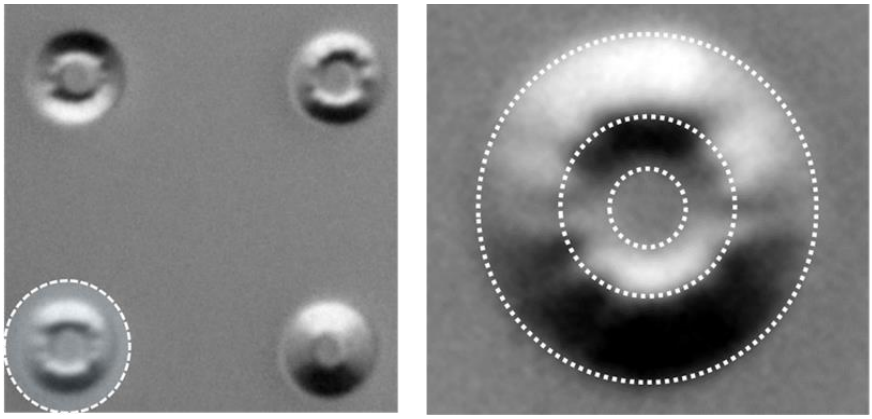

Fig. 3.6 (Left) X-PEEM image of four LSMO donuts with ID 0.4 μm. (Right) A zoomed-in image of the donut is highlighted with the dotted line.

Figure 3.7 shows MuMax[3] simulations, which suggest that these screwhead domains consist of two concentric vortex structures with opposite chirality with the formation of cross-tie domains instead of a 180° domain wall at their interface. These cross-tie domains consist of alternating vortex/antivortex structures (denoted by the bright/dark spots) along the path of the domain wall. The formation of this type of complex spin texture is unexpected and, from a characterization perspective, limited by X-PEEM resolution to concisely simulate the area of domain walls that is observed.

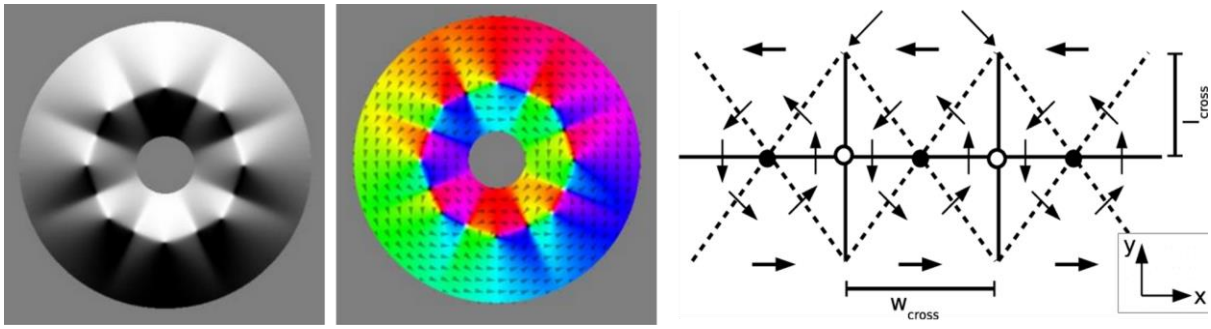

Fig. 3.7 (Left) MuMax[3] simulation of a double-vortex domain texture as seen from X-PEEM images of the LSMO donuts. (Center) *m-space* image of the domain patterns with apparent magnetic moment arrangements. (Right) illustration of cross-tie domains along the interface between the two vortex domains.

3.2 Quantitative Image Analysis Methods

To explain the formation of the screwhead domains, a quantitative analysis of the X-PEEM images was performed using the methods developed by Lee *et al.* [60] as inspiration. The spin textures in the LSMO donuts possess a unique blend of spatially varying magnetic anisotropies. Quantitative image processing techniques enabled in this research operate through first-order approximation of spatially dependent variables extracted from X-PEEM images and hence, provide a framework for characterizing spin textures of the LSMO donuts. This approach also contributes to visualizing expected micromagnetic behavior as well as any deviations from the physics governing spin texture formations that may not be readily apparent from experimental observations alone. The following sections elucidate this quantitative framework.

3.2.1 Image Distortion Correction

Raw X-PEEM images possess lateral distortions caused by the stigmatism of the lenses in the PEEM3 microscope. These distortions present themselves as stretching of the circular shape of the micromagnets. This deviation can be removed using a "perspective transformation" algorithm

scripted in Python programming language that warps an image perspective about a 4 X 2 matrix of corrected pixel coordinates (refer to Appendix A.1). This operation involves a perspective correction of the image uniformly rather than just a polar transformation of a single coordinate in the image, hence, ensuring that the nominal features of the original X-PEEM image remain intact without modifications to any individual pixel. A schematic representation of perspective correction performed to a set of four nearest neighbor LSMO donuts with ID 0.2 μm is given in Figure 3.8. The yellow dashed square doesn't have its corners located at the centers of the four micromagnets, indicating that they are in a non-square geometry due to the stretching of the X-PEEM image. This stretching is made evident in a magnified image in Figure 3.8 of one of the donuts at the right lower corner (circular edge highlighted in black dashed line) with an apparent ovular shape. Figure 3.8 also represents the same donut image following distortion correction where perspective transformation imparts a circular shape to the donut, given the image's dimensions remain unchanged (in blue line). The appearance of thin blackened regions at the image edges arises from this apparent change in perspective and factors in the two-dimensional warping of the image object within the original dimensions and preserving the pixel quality of the X-PEEM image.

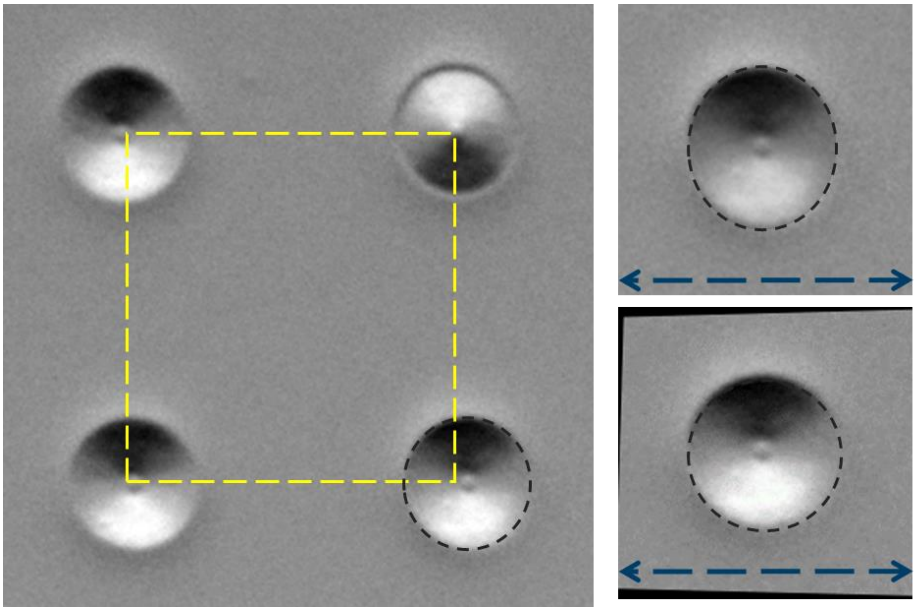

Fig. 3.8 An example of an image distortion correction process applied to an LSMO donut (ID 0.2 μm). The yellow square shows a misalignment of the donut centers, highlighting the distortion of the X-PEEM image. An individual donut (in black dashed outline) is chosen to be corrected for its stretched distortion (top right corner). The processed image is shown in the bottom right corner with a blue schematic representation of equal matrix size.

3.2.2 Radial Intensity Profiling

The purpose of image distortion correction is fundamental for any further quantitative operations to characterize spin textures in the LSMO donuts. Because of this distortion correction, a radial intensity profile of a circular micromagnet possessing a vortex state would represent a sinusoidal wave. This radial intensity profiling method performed on LSMO micromagnets allows us to distinguish between the sinusoidal curve associated with a vortex state from the abrupt changes in domain contrast associated with a Landau pattern shown in Figure 3.9. This figure shows the radial intensity profiles of a square micromagnet imaged at 32 K with a pure Landau pattern and a circular micromagnet at 230 K with a pure vortex pattern. The Landau patterns consist of abrupt steps

every 90 ° while a sinusoidal wave characterizes a pure vortex state. Profiles of domain patterns imaged at intermediate temperatures like the ones described in this thesis are expected to lie between these extreme profiles, i.e., combining a pure sine wave and a pure step function.

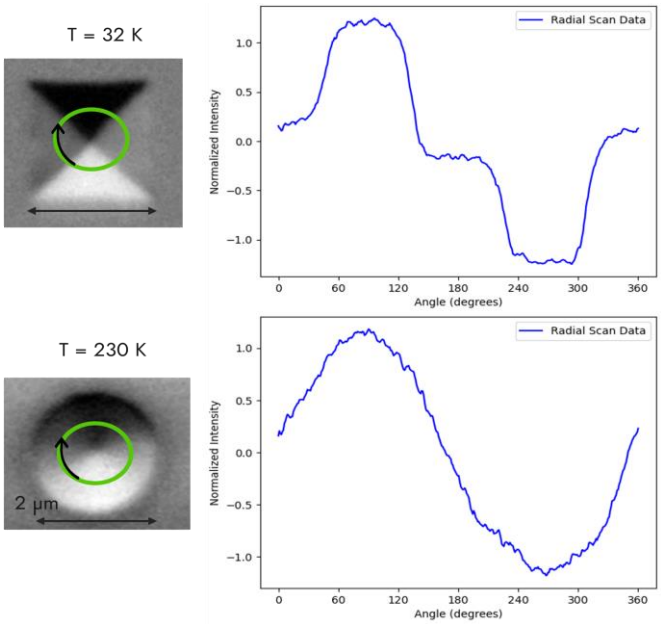

Fig. 3.9 Radial intensity scan profiles of a pure Landau pattern (top panel) and pure vortex state (bottom panel) corresponding to a square and circle micromagnets taken along the green circular path.

This radial intensity profiling is performed by binning intensity values from X-PEEM images across elementary circular paths (2-4 pixels thick) with varying radii. Normalized intensity values range between +1 and -1 depicting white and dark domain contrast range.

3.2.3 Vortex Fraction Calculation

Lee *et al.* conceptualized a metric called the *vortex fraction* (VF) to quantify the relative amount of vortex vs. Landau character in the X-PEEM images from LSMO micromagnets given by,

$$VF = A_{sine} \div (A_{sine} + A_{step}) \qquad \text{(Equation 3.4)}$$

where the equation is parameterized by the amplitude of the sine wave (A_{sine}) and the amplitude of the step function (A_{step}) obtained from radial profile scans. These amplitudes represent the greyscale intensity of the domain images along a radial scan and vary between +1 to -1 for white to black regions (respectively). This variation is a quantitation of the proportion of a vortex (sine-like) or a Landau(step-like) pattern. VF captures the deviation from a pure vortex state observed at low temperatures in circular micromagnets due to the formation of Landau states in the center of the micromagnets due to the increase in MCA. For example, Figure 3.11 plots a radial profile of an LSMO donut with ID 0.4 μm at 0.6 μm scan radius (green circle) as a function of angle. The purple wave that is superimposed on the radial profile (green curve) is fitted with a linear combination of sine and step functions. The resulting vortex fraction is obtained from the optimized curve-fit using the computational script presented in Appendix A.2. Further, the same fitted wave (purple dashed line) is decomposed into its constituent step and sine waves in Figure 3.10(b) to highlight the contributions of the pure Landau and pure vortex states, respectively.

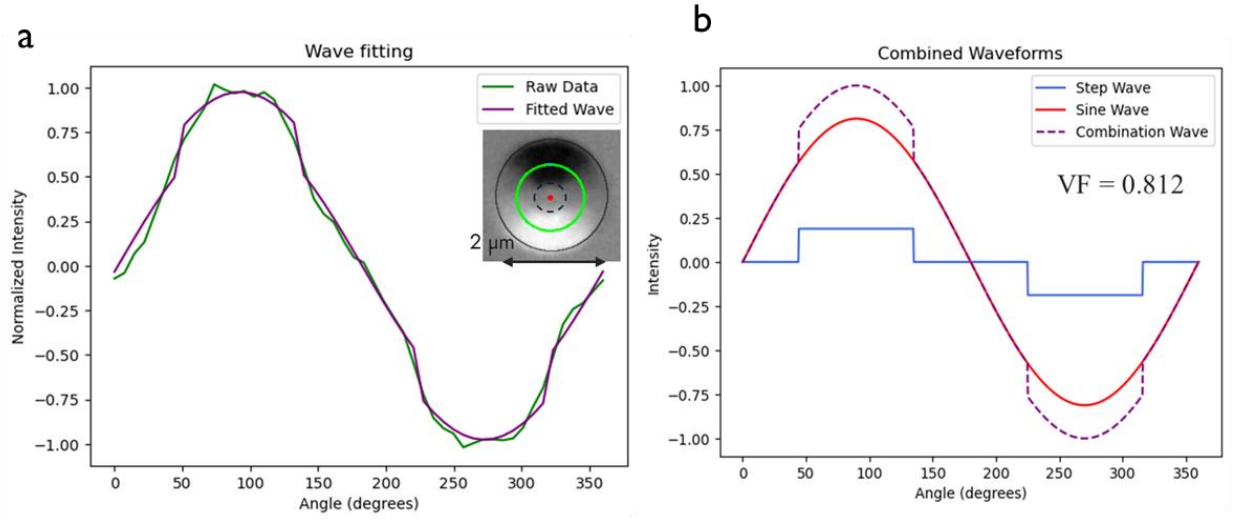

Fig. 3.10 (a) The principle of obtaining VF using first-order curve fitting for a radial scan profile (in green line) about a circular ring on a donut ID 0.4 μm (green circle shown in inset). Inset schematics show circular edges and the center of the donut. **(b)** The fitted curve (in purple line) is decomposed into its constituent sine and step functions, showing the quantification of vortex and Landau states.

This quantitative analysis is applied to each set of LSMO donuts with single vortex patterns (i.e., non-screwhead domains) across varying hole diameters and the results are presented in Chapter 4.

3.2.4 Micromagnetic Simulations

MuMax[3] simulations corresponding with each of the spin textures obtained in LSMO donuts were performed to help understand the local magnetic parameters for LSMO, which can reproduce the spatially varying profiles of vortex vs. Landau patterns observed in X-PEEM images acquired at 110 K. The RK45 solver in MuMax[3] considers the shape of the micromagnet, M_{sat}, A_{ex}, and K_1 values for LSMO thin films. As a starting point, the values presented in the supplementary information in Ref. [60]) were approximated for a temperature corresponding to 110 K. The relationship between M_{sat} and A_{ex} is given by,

$$A_{ex} = M_{sat} \frac{D_{sp}}{2g\mu_B}, \qquad \text{(Equation 3.5)}$$

where g is the Landé factor, μ_B is the Bohr magneton, and D_{sp} is the spin wave stiffness constant. These temperature-dependent parameters and material constants (see Appendix B) were used as input to set up MuMax[3] simulations for the circular micromagnets and the donuts. The simulation solver considers the geometrical specifications of the micromagnets and solves the Landau-Lifshitz-Gilbert equation (Equation 2.5) to relax the various magnetic energies. The solution to this operation is obtained in the form of a spatial image like that given in Figure 3.11 and further discussed in Chapter 4 to correlate results obtained from X-PEEM image analysis.

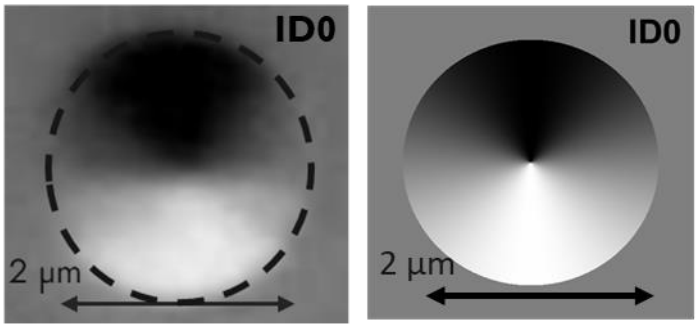

Fig. 3.11 MuMax[3] simulation (right) of a circular micromagnet (left) imaged with X-PEEM at 110 K. The magnetization of the simulation is set to vortex along the M_x direction with material properties and anisotropic definitions for the simulation grid in the MuMax RK45 solver.

In this purview, I performed MuMax[3] simulations to superpose Landau and vortex proportions to closely approximate VF as obtained from X-PEEM images and empirically model spatial anisotropy variations in the donuts. The simulations obtained are to be treated as ideal without any defects. The simulations help fine-tune anisotropy energies by defining K_1 constants in radial increments of ring elements (refer to Appendix B Figure B.1) about 100 nm thick instead of setting uniform K_1 across the simulated donut. This spatial setting in simulations form a K_1 continuity

mesh and, upon relaxation of magnetic energies in the simulation grid, develops into domain patterns resembling those observed in the X-PEEM images (refer to Figure 3.5).

Lee *et al.* [60] found that a spatially varying K_1 profile was needed to describe the VF profiles extracted at intermediate and low temperatures from their circular micromagnets (see Figure 3.12). They found that the best fit was obtained using a sigmoid function which represents a probabilistic distribution characterized by an S-shaped curve and is given by the relationship,

$$f(x) = \frac{1}{1 + e^{-ax}} \qquad \text{(Equation 3.6)}$$

where x is the input variable, e is the base of the natural logarithm (Euler's number), and a is a parameter that controls the steepness of the curve. This sigmoidal function was adopted to account for the strain that is imposed from the surrounding implanted matrix onto the circular micromagnets. As the ion implantation process leads to an expansion of the matrix regions, it is postulated that it also imposes a compressive lateral strain.

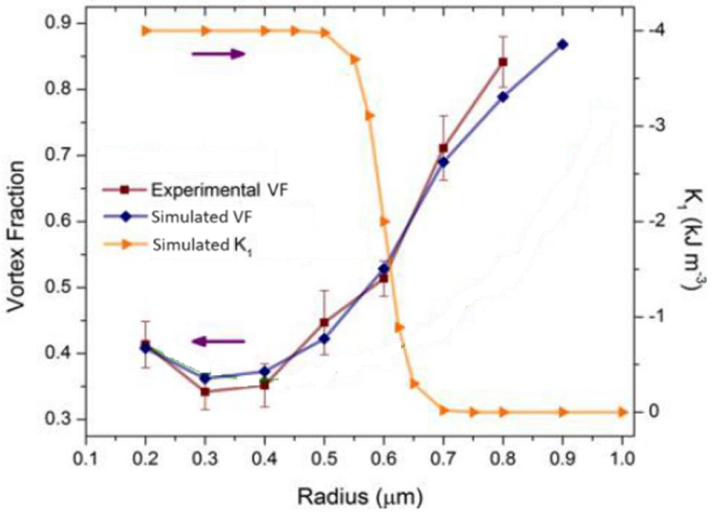

Fig. 3.12 Vortex fraction vs. radius obtained from circular LSMO micromagnetic discs at 32 K of 2 μm diameter and 40 nm thick for X-PEEM data (red line) and simulations (blue line) depicting an abrupt decay of K_1 in the form of sigmoidal profile (in orange line) going from the micromagnet center to the outer perimeter. Adapted from Ref [60].

3.3. Summary

This chapter discusses the salient features of the domain structures as observed in the LSMO donuts and the qualitative theories surrounding their complex patterns. A list of quantitative and computational analysis techniques has been outlined to corroborate these discussions to understand their magnetic behavior about their altered easy axes and the importance of mapping spatially varying MCA through MuMax^3 simulations and vortex fraction calculations. Chapter 4 further provides a comprehensive picture of the results drawn from these analyses and correlates my experimental and computational techniques used to probe the LSMO micromagnets.

Chapter 4: Results and Discussion

A replicated growth process outlined by Lee *et al.* [60] and standard process parameters, as reported in Chapter 2, were used to fabricate LSMO thin films. X-PEEM imaging revealed intriguing domain textures in LSMO donuts in the form of the vortex phenomena described in Chapter 3. The computational and quantitative image analysis methods described in Chapter 3 were used to comprehensively probe their micromagnetic character, particularly explaining spatial variations in the effective magnetic anisotropy in each donut. The varying sizes of the holes imparted a unique spatial trend to each donut set, implying the functional tuning abilities that our fabrication techniques can impart to further the spintronic theory described in Chapter 1.

4.1 Magnetic Domain Image Analysis in LSMO Donuts

4.1.1 Vortex Fraction Profiles

The fundamental characterization principle of analyzing domain images considers precise image distortion correction measures followed by radial profiling in ring elements with about 4-pixel width (~ 0.057 μm) incremented radially from the donut's hole edge to the donuts' outer circumference. The width of these ring elements was optimized to provide sufficient spatial resolution, while also achieving a sufficient signal-to-noise ratio. Figure 4.1(a) shows a comparison of radial profiles for LSMO donuts of varying inner diameter at a scan radius of 0.7 μm for X-PEEM images acquired at 110 K. A general trend showing deviation from a nearly pure sine wave to a more step-like nature can be observed as the inner diameter of the holes increases from 0.2 to 1.0 μm. A similar analysis with radial profiling within 0.2 μm of the hole edge is shown

in Figure 4.1(b) where this deviation from a pure vortex (i.e., sine wave) to include a step proportion (i.e., a Landau component) also shows the same general trend. Curve-fitting using first-order approximation was performed to determine the VF as a function of radial distance away from the center of the donut and plotted in Figure 4.2 for donuts with inner diameters ranging from 0.2 to 1.0 µm. A sampling of four donuts from each hole size set resulted in a nominal error of ~10^{-2} in VF.

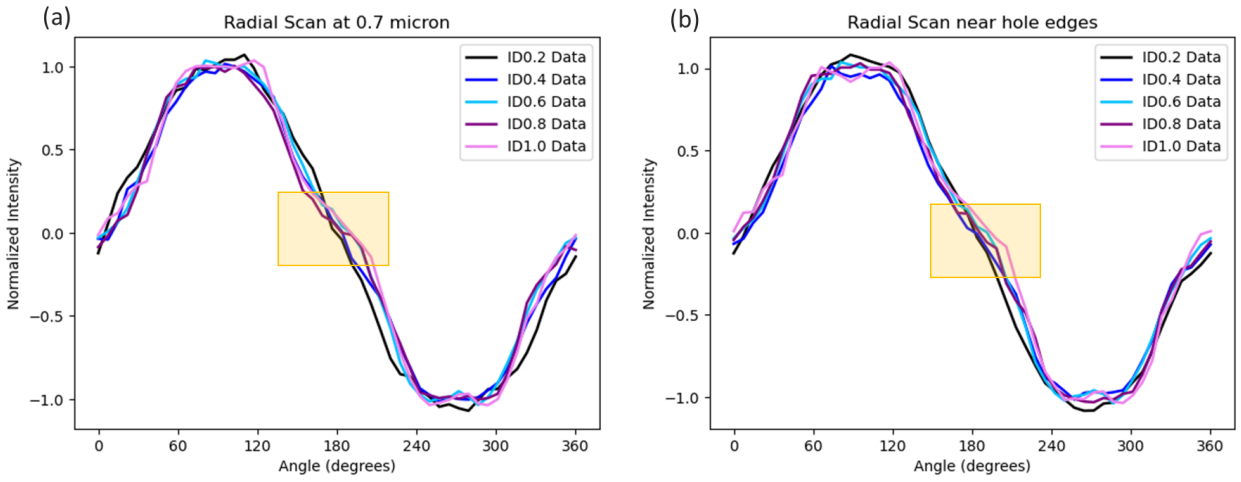

Fig. 4.1 (a) Radial profiles at a scan radius of 0.7 µm from domain images of LSMO donuts as a function of inner diameter from 0.2 to 1.0 µm. **(b)** Radial profiles at a scan radius of 0.2 µm from the LSMO donut's hole edge. The yellow highlights show deviations from a pure sine wave to include a more step-like profile as a function of the hole's inner diameter.

The relatively flat black line in Figure 4.2 close to VF = 1 implies an almost pure vortex nature in the circular LSMO micromagnets (without a hole, OD = 0 µm) at 110 K. However, a decrease in VF with increasing hole inner diameter can be observed. This trend can be visualized in the X-PEEM images shown in Figure 3.5 as a more pronounced division of the contrast into distinct black/white/grey regions (consistent with a Landau pattern) instead of a gradual transition corresponding to a vortex state. It should be noted that the LSMO donuts, irrespective of the inner

diameter, retain a predominance of the vortex state (average VF > 0.6) at 110 K even without a vortex core. Radial line scans from the hole edge of the donuts to the outer circular edge show that the VF is not uniform throughout the LSMO donuts but rather tends to decrease towards the hole edge, and to a lesser degree towards the outer edge. As a result, the maximum VF is observed for a scan radius between 0.5-0.7 µm. Contrary to the general trend, the LSMO donut with ID 1.0 µm shows a maximum VF near the hole edge and decreases with increasing scan radius (radial distance from the donut center). A minimal hole diameter such as 0.2 µm emphasizes the decrease in VF with a steeper slope towards the hole edge and the outer edge.

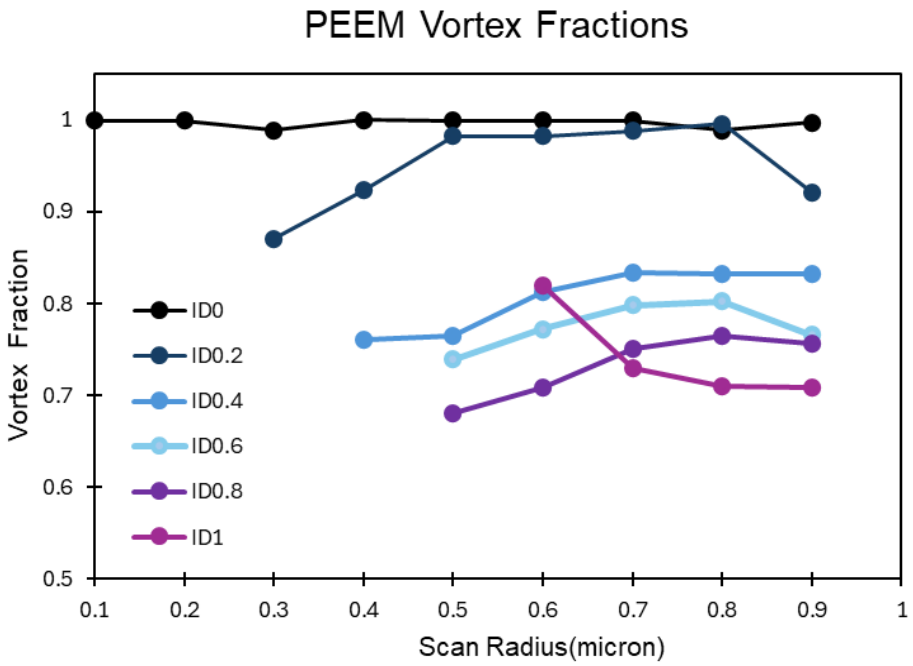

Fig. 4.2 Vortex fraction as a function of scan radius determined using radial profiling and computational model fitting for LSMO donuts with ID 0-1.0 µm.

4.1.2 Spatial Variation in Magnetic Anisotropy

The non-uniform VF profiles in the LSMO donuts (Fig. 4.2) suggest that K_1 also varies with the scan radius and the hole diameter of the donut. MuMax[3] micromagnetic simulations were used to

determine the best K_1 profile that reproduces the VF behavior of the LSMO donuts from the X-PEEM image analysis. The uniform VF profile for the LSMO circular micromagnets implies a uniform K_1 throughout its volume. MuMax[3] simulations performed using a uniform K_1 value agreed with VF analysis from X-PEEM interpreted as a nearly complete vortex state and is illustrated in Figure 4.3. A uniform $K_1 = 0$ J/m^3 confirms the absence of MCA in the LSMO circular micromagnets. For comparison, the VF profiles obtained by Lee *et al.* using a sigmoidal function for circular micromagnets imaged at a lower temperature of 32 K are also shown in black in Figure 4.3. The differences may come from the combined effects of different samples as well as the increase in K_1 value at lower temperatures.

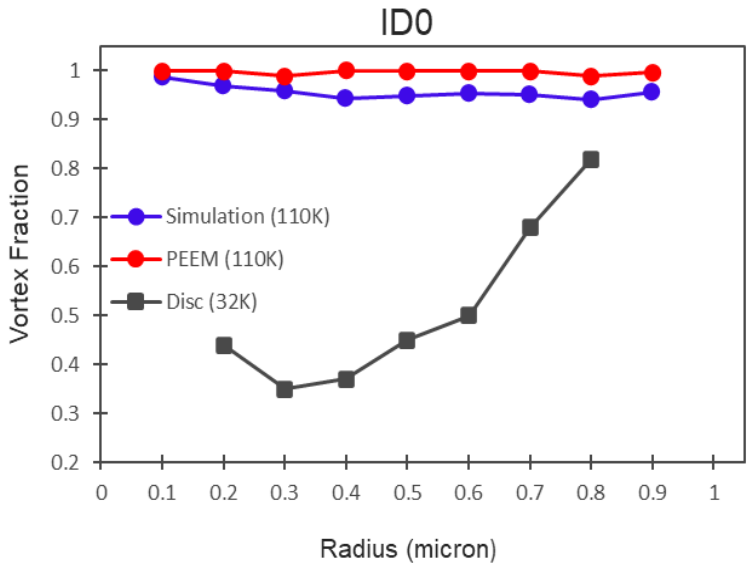

Fig. 4.3 VF calculations obtained from X-PEEM (red line) and simulated images (blue line) of the LSMO disc (ID 0 µm) show an almost pure vortex proportion (V.F > 0.94) irrespective of scan radius. The analysis by Lee *et al.* and a comparative VF trend computed in the micromagnetic discs at 32 K are shown in the black line. The comparison showcases the absence of magnetic anisotropy variation in the domain patterns imaged and simulated at 110 K.

The sigmoidal K_1 decay model used by Lee *et al.* was used as a first attempt to model the VF profiles determined for the LSMO donuts (Figure 4.4). This profile includes an abrupt change in

K_1 at 0.7 μm radial distance from the center of the micromagnet according to the observations made from VF calculations on the LSMO circular discs.

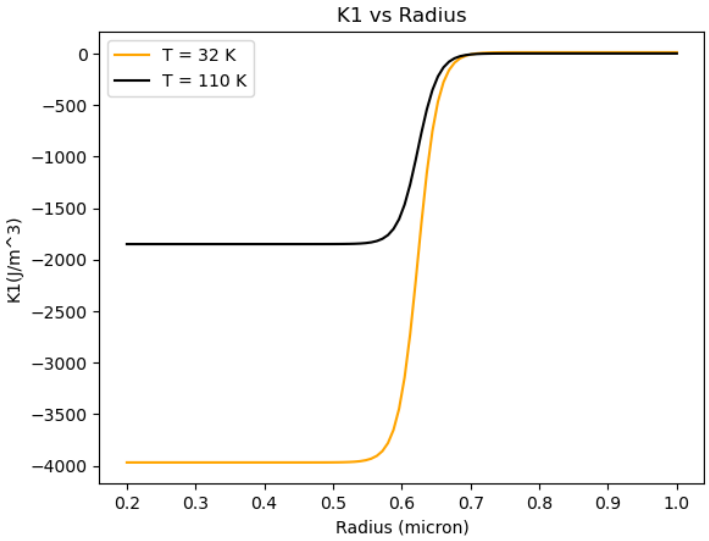

Fig. 4.4 K_1 variation for MuMax^3 simulations using a sigmoid function as a function of radial distance and temperature utilized for circular micromagnets. The original S-shaped curve (in orange) is adapted from Ref [60] and approximated for a temperature of 110 K (in black). The maximum value of K_1 reaches 1850 J/m^3 as calculated by Lee *et al.* and 0 at the outer edges corresponding to a vortex state observed from PEEM imaging. A negative y-axis only indicates syntactical definitions of K_1 in the MuMax^3 console.

The domain patterns imaged using X-PEEM and the subsequent VF analysis shown in Figure 4.2 paint a different picture of the MCA landscape compared to the previous work by Lee *et al.* At 110 K, there is a net deterrence in the vortex state as the hole size increases. Moreover, the 'bowing' of the VF profiles implies that K_1 values should increase towards the hole edge and the outer edge. To represent spatially varying anisotropy across the LSMO donuts in MuMax^3 simulations, two separate K_1 models were used namely (i) the 'sawtooth' model for ID 0.2-0.6 μm and (ii) a linear model for ID 0.8-1.0 μm. The mathematical representation of a sawtooth wave used in this work is:

$$y(t) = A\left(t - \frac{|t|}{T}\right), \qquad \text{(Equation 4.1)}$$

where y(t) is the value of the sawtooth wave at parameter t, A is the amplitude of the sawtooth wave, t represents the base function, which gives the greatest integer less than or equal to t, T is the period of the sawtooth wave, representing the length of one cycle. However, in the context of fitting data, the sawtooth function (Figure 4.6) used in curve fitting here includes parameters for amplitude and a sine base function. Simulations at low temperatures and corresponding K_1 approximation models are provided in Appendix B.

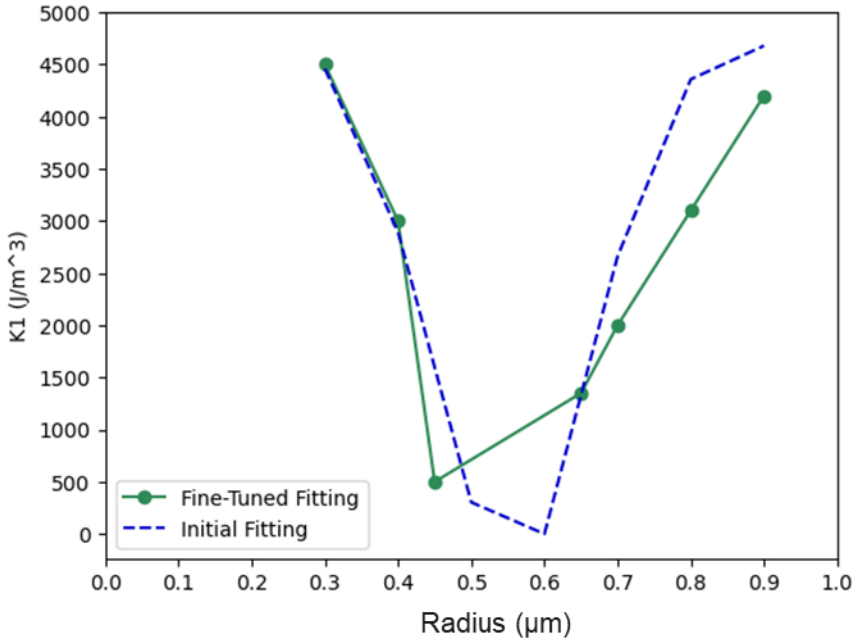

Fig. 4.5 A saw-tooth function optimized curve-fitting to capture the K_1 trend for an ID 0.6 μm donut simulation. K_1 values (in blue) are a nearly ideal saw-tooth fitting approximated from initial simulation trials to represent the VF trend as obtained from XPEEM domain images including the vanishing of MCA when K_1 reaches almost zero near 0.6 μm radial region. The green curve is a fine-tuned saw-tooth model for the exact representation of the VF profiles included in simulation results and close approximation with results from XPEEM images.

The saw-tooth model for defining K_1 was used for simulating the LSMO donuts in MuMax[3]. The simulation space was divided into circular regions (inner to outer circular edges) for setting K_1 that best fitted VF calculations done on the X-PEEM images. Figure 4.6 below shows the simulated LSMO donut images (ID 0.1- 0.8 μm) as obtained from MuMax[3]. These simulations not only show the domain contrasts of the X-PEEM imaged donuts in high resolution but also provide a simpler method of comparing their magnetic energy densities across space. Provided the VF calculations from these simulations are in good agreement with the X-PEEM images, one can fine-tune K_1 spatial definitions to obtain a concise quantitative model of the micromagnets in vector space.

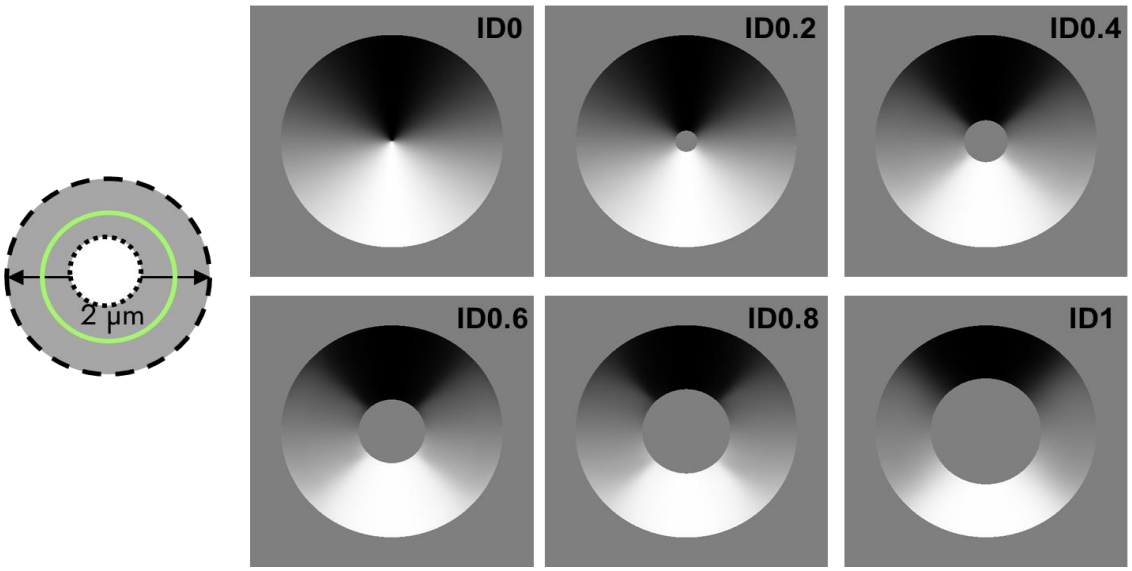

Fig. 4.6 MuMax[3] simulated domain images for LSMO donuts with an outer diameter of 2 μm and varying ID. The schematic picture depicts a ring element (green circle) and the donuts' circular dimension. A series of such ring regions are defined with spatially varying K_1 values within the simulations in radial increments of 100 nm, parsing the magnetic volume enclosed between the hole and outer circular edge.

4.2 Experimental and Simulated Methods

I will now discuss anisotropy characterization in the LSMO donuts following a categorization according to the hole sizes (or ID) and the salient magnetic features present. Figure 4.7 displays the saw-tooth K_1 model (in green) characterized by a flat step corresponding to $K_1 \sim 0$ J/m^3 which

best describes the edge phenomena and uniform VF in the center of the LSMO donuts. The gradual increase of K_1 at the hole edge between scan radius 0.3-0.5 µm is higher than that of the increase in K_1 towards the donut edge (i.e., beyond scan radius 0.7 µm).

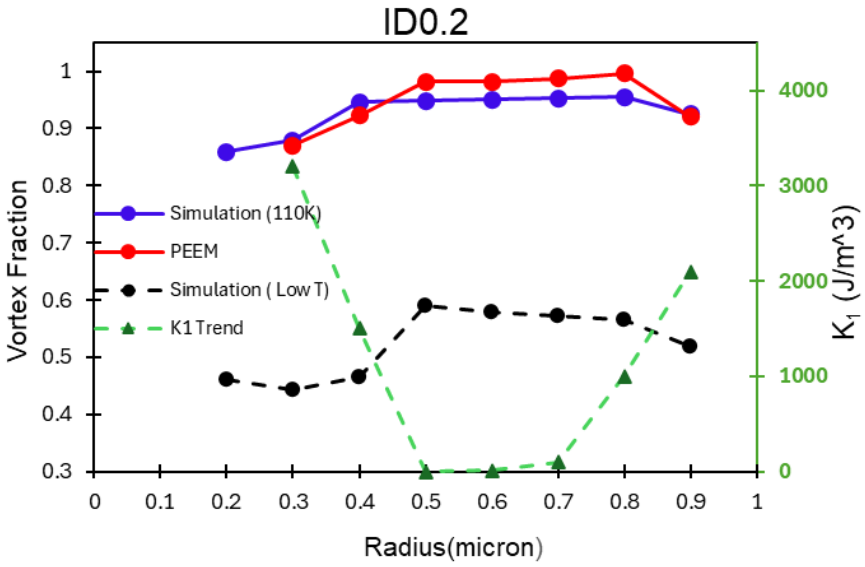

Fig. 4.7 VF calculations obtained from X-PEEM (red line) and simulated images (blue line) of the LSMO micromagnetic donut ID 0.2 µm. The simulations use K_1 approximation (green trendline) on the green axis as used from a saw-model model. A predictive analysis using the K_1 saw-tooth model describes VF for low temperatures like 32 K (black line) used by Lee *et al.* (refer to Figure 3.12). Here, the VF profile is almost bowing at the outer edges of the donuts rather than continuously increasing as seen in the case of the disks at 32 K.

Furthermore, an approximation of the simulated VF trend of the donut was performed for lower temperatures by curve-fitting and normalizing previously computed low-temperature parameters, such as the maximum K_1 value of the discs at 32 K, and setting material parameters A_{ex}, $M_{sat,}$ and <110> anisotropy directions. The low-temperature trend shows a prominent Landau contribution or decrease of VF, as MCA dominates at these lower temperatures. The green triangular data points represent circular regions of the simulation space where K_1 is set at the corresponding radial

location along the x-axis. A similar operation is performed to characterize the spin textures of ID 0.4 μm and ID 0.6 μm, as shown in Figure 4.8.

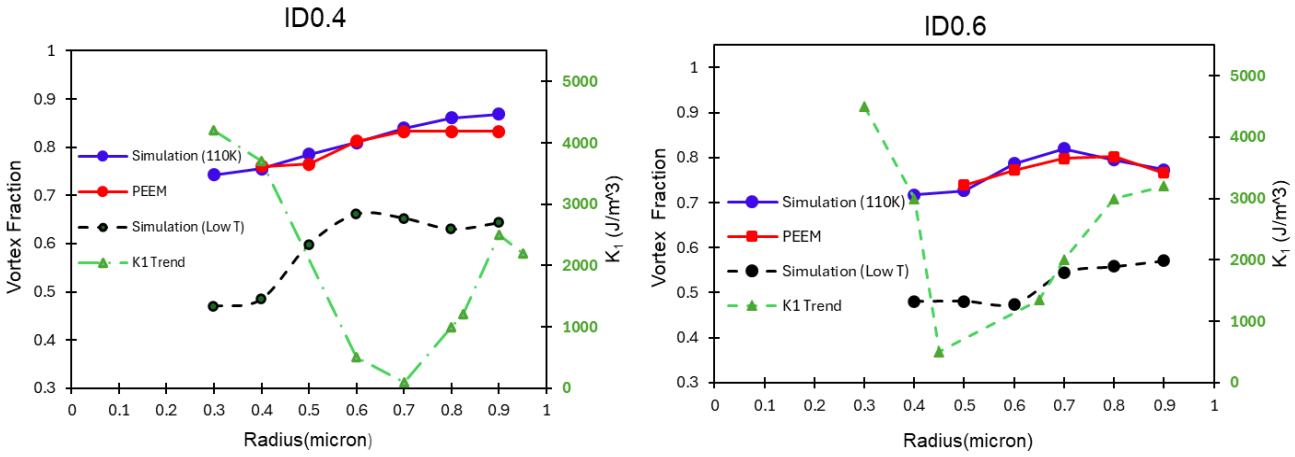

Fig. 4.8 K_1 variation (in green trendline) and VF profiles of X-PEEM (red line) and simulated spin textures (blue line) for (left) 0.4 μm and (right) 0.6 μm ID, respectively. The black line represents the extrapolation of VF trends at low-temperature simulations.

In addition to the ring definitions, secondary rings like shown by green data points at 0.8-0.82 μm for ID 0.4 μm or between 0.6-0.7 μm are defined to further approximate the saw-tooth model at the uniform VF region in the simulations like that observed from X-PEEM domain images. For large hole sizes, the magnetic volume in the width enclosed by the hole and the outer edge is reduced, implying the strain states have likely changed from patterning. Figure 4.9 plots the K_1 variation for donuts with IDs 0.8 μm and 1.0 μm where a polynomial function matches the VF trend with a relatively constant value towards the edges of the micromagnets.

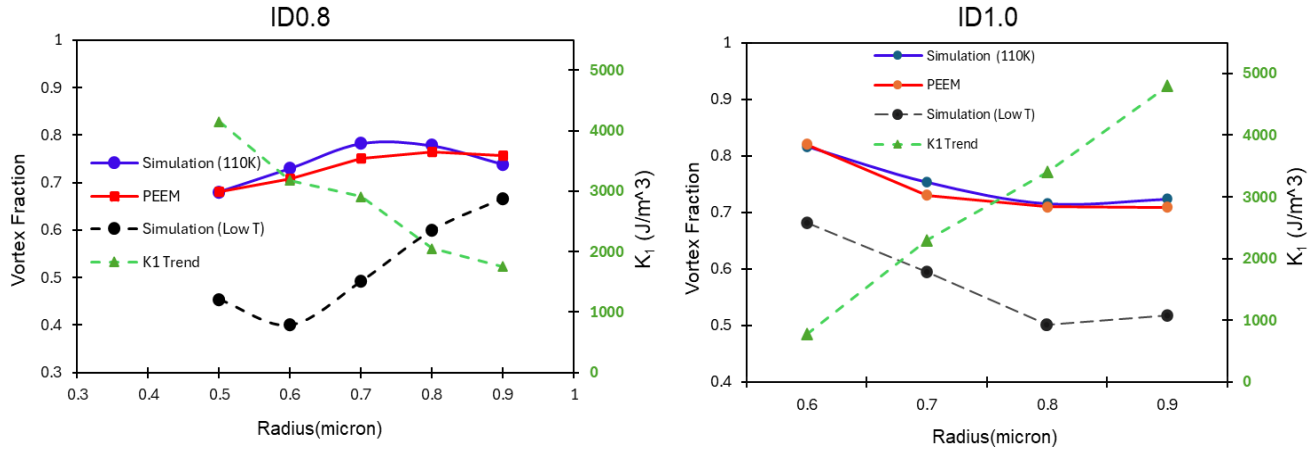

Fig. 4.9 K_1 variation (in green trendline) and VF profiles of X-PEEM (red line) and simulated spin textures (blue line) for (left) 0.8 µm and (right) 1.0 µm ID, respectively. The black line represents the extrapolation of VF trends at low-temperature simulations.

The reversal of a K_1 decay trend in the LSMO donut with ID 1.0 µm is, in principle, due to a relatively large MCA existing near the outer edge compared to the other donuts as confirmed quantitatively but also partly suggestive of a difference in energy penalty to anisotropy at either edge brought about by increasing the hole size. However, spatially varying anisotropy and, hence, magnetic energy variation at the same temperature hint at a different force at play, most likely a strain component that exhibits variability in edge phenomena. This spatial variation is observed uniformly across the LSMO donuts irrespective of inner diameter, except for ID 1.0 µm, which is attributed to a two-fold principle. Firstly, the strain states that exist in the material volume and at the edges of the circle-shaped donuts by material structure as obtained from epitaxy, and secondly, modification of these energy states by the introduction of stress anisotropy as the hole diameter changes in size, likely from ion-implantation causing different strain effects at the edges and the central micromagnetic volume.

The underlying crystal structure of the LSMO thin film gives rise to its inherent anisotropy. Previous investigations have shown bulk LSMO to possess an in-plane uniaxial easy axis along the <100> directions and a hard axis along the <110> directions. For LSMO thin films grown under small tensile strain on (001)-oriented STO substrates impart tetragonal distortion to the lattice grown with the magnetic easy axis lying along the in-plane <110> directions [57] [58]. The same studies also stipulate a significant MCA contribution exists from strain effects rather than any non-uniaxial contribution from an additional hard axis, both of which lie in the plane for the LSMO film. The only other anisotropy contribution that can arise in the lattice structure is likely from stress anisotropy unless a rhombohedral MCA is present in the case of growth in a (110) orientation. As discussed in Section 3.1.3, the implanted LSMO film matrix during the patterning process is a significant source of strain distributed at the inner and outer edges of the donuts. The results discussed in this chapter strongly imply the presence of strain from an expanded lattice which makes these LSMO donuts unique compared to traditionally patterned material systems in which material is removed surrounding the magnetic features.

This hypothesis on the contribution of strain effect to offset the potential anisotropy variation has yet to be experimentally proved. Contemporary research on magnetic 'dots' and 'anti-dots' in metallic nanomagnets shows an edge variation of anisotropy brought about by the size and spacing of the nanostructures [95], [105]. In principle, compared to their metallic counterparts, complex oxide micromagnets show more correlated spin-orbit phenomena that can pronounce the effect of MCA and related magnetic energies in ferromagnetic systems. The combined interpretations from analyzing LSMO discs performed by Lee *et al.* [60] and the unique spatial features of LSMO donuts presented in this thesis pose a distinct magnetic energy landscape in micromagnetic research where subtle energetic changes can bring about drastic effects in their domain

arrangements. Since MuMax[3] simulations can additionally characterize energetic profiles across magnetic regions, magnetic energy variation from the complex K_1 model was estimated.

4.3 Magnetic Energy Density Approximation

Figure 4.10 illustrates magnetic energies, namely contributions from magnetic anisotropy, exchange, and demagnetization energies. The energies are derived from the individual ring elements used for the K_1 profile and integrated over the magnetic volume in each donut. Anisotropy energy is seen to be higher for intermediate and larger ID donuts, with a maximum for ID 0.6 µm (~ 2798.7 J/m^3). This order is consistent with the decrease in the overall vortex component in these IDs, as shown in Figure 4.3. Notably, the overall order of the different energies (~10^3) corresponds to that obtained for LSMO discs at the intermediate temperature range, implying the range of operation for setting both the saw-tooth and the sigmoidal K_1 spatial approximation is more or less similar in the same simulation space. Further, demagnetization and exchange energies were found to decrease as hole sizes got bigger. This is consistent with the fact that E_{ms} or demagnetization, as given in Equation 3.3, doesn't directly depend on a strain term.

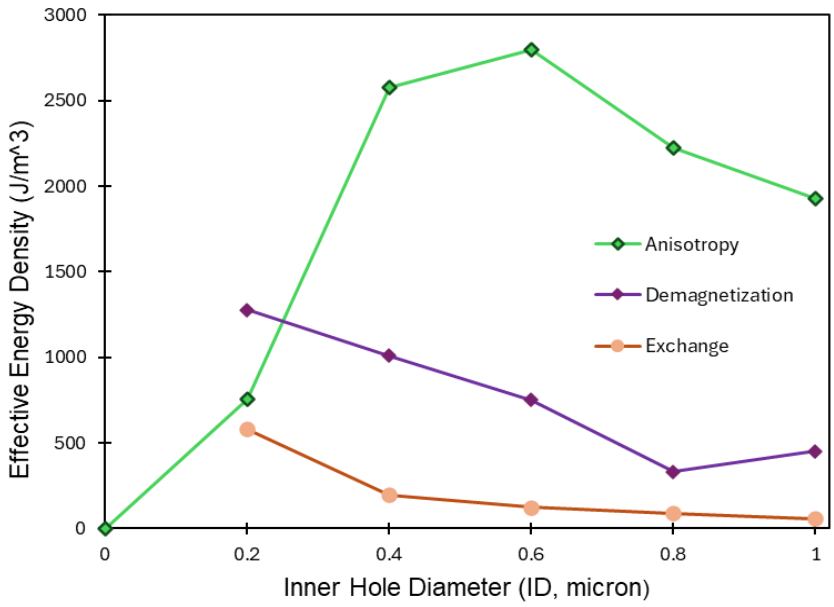

Fig. 4.10 Magnetic energy density profiles of the simulated LSMO donuts as a function of hole size.

Exchange interactions are related to the alignment of neighboring magnetic moments and rely on the electronic band structure of the material. However, the exchange energy order is effectively lower compared to the overall anisotropic energy densities and similar for hole sizes greater than ID 0.4 µm. Given that strain is present, the anisotropy energy expression can be modified to include strain-dependent terms. However, there is a lack of experimental validation for a unified strain theory in literature to adequately quantify this strain effect in complex oxide thin films.

To investigate if the changing magnetic anisotropy energies were indicative of a modified strain state brought about by the hole size in an otherwise uniform circular geometry of the micromagnets, Table 1.1 lists the energy densities in the elemental rings at the hole edge, outer edge, and in the central region between the edges.

K_1 Energy Density in Rings (J/m^3)	ID 0.2 µm	ID 0.4 µm	ID 0.6 µm	ID 0.8 µm	ID 1.0 µm
Near Hole Edge	458.390	669.614	706.005	714.042	115.877
Near Outer Edge	295.738	346.502	608.001	303.250	830.889
Near Center	109.080	999.000	1350.001	2910.089	3300.530

Table 1 Energy densities as obtained from MuMax[3] simulations of ring elements near the hole edge, outer edge, and central region between the edges.

These differential energies show a more significant proportion of the overall energy density near the holes than the outer circular edge. The principle reverses for ID 1.0 µm to yield a higher vortex near the hole edge. In principle, if the inner strain at the hole edges increased with hole size, the offset would be proportional to the compressive strain to the magnetic volume caused by the outer edges. This disproportion is evident from the difference in near-hole edge and outer edge energy densities for each donut. The difference is highest for ID 1.0 µm (~ 750 J/m^3) and lowest for ID 0.6 µm (~ 98 J/m^3). The X-PEEM VF trend for ID 0.6 µm in Figure 4.2 that shows the least steep positive slope change could be correlated to this quantification where the anisotropic energies at both edges are in competition or strain states have a significant effect. The energy densities near the center (to be noted as the geometric center of the magnetic volume enclosed between the circular edges) of the micromagnets are found to be increasing from smaller holes to the larger ones. Similarly, in the same Figure 4.2, ID 1.0 µm is characteristic of the steepest negative slope. A large offset to the net anisotropy energy would be caused by more considerable strain from a large hole. For ID 0.2 µm the difference in energy densities between the center and the edges do not vary so significantly as the larger hole diameters ID 0.4-0.8 µm. This is in line with the observation that ID 0.2 µm has a rather flat slope for a VF profile and a minimal K_1 variation at

the center while for the other donuts an additional energy contribution from matrix strain must be accounted for to understand the overall energetics of the system. The largest energy density difference observed for ID 1.0 μm implies the positive K_1 spatial variation slope and an abruptly decreasing VF profile moving away from the center.

4.4 Limitations

The quantitative characterization of strain theory discussed in the previous sections is limited by experimental designs in conventional transmission electron microscopy owing to their destructive principle, which is likely to interfere with the metastate magnetics revealed by domain patterns. The challenge arises in probing the nature of strain states in the LSMO donuts at sub-micron length scales (a depth of 40 nm) without distorting the magnetic state of the material as observed from XMCD and X-PEEM. Moreover, simulation artifacts encountered with the MuMax^3 solver tend to reach a less than 100% vortex state at $K_1 = 0$ and underestimate VF values compared to values calculated from X-PEEM images. This artifact is apparent in Figures 4.5 and 4.6, where simulation and PEEM VF slightly diverge (highest VF reached ~ 0.95 in simulations) or create an 'alligator mouth', *i.e.* the mismatch between the maximum VF reached from MuMax^3 simulations and that in X-PEEM image analysis. MuMax^3 doesn't yield close to 0.99 VF at $K_1 = 0$. These artifacts slightly skew precise approximations in the characterization of magnetic parameters and only yield a range of potential anisotropy variation instead of absolute anisotropy constants. Moreover, the standard deviation of VF as represented in this chapter is of a nominal order ~ 0.04 as calculated from the X-PEEM images. X-PEEM's spatial resolution is limited (between 50 -100 nm) which poses a challenge to precisely profile circular edges as the domain images incorporate lens aberrations. Moreover, probing the vertical component of magnetization in the micromagnets is

limited by X-PEEM capabilities to shed light on the out-of-plane characteristics of the magnetic states, challenging our complete understanding of the double vortex phenomena.

4.5 Conclusion

In conclusion, the LSMO micromagnets with varying hole sizes present a range of unique spin textures and flux closure domain arrangements that proportionately vary between vortex and Landau states. These domain arrangements result from a delicate balance between the thin film's local magnetic anisotropy interactions and structural factors. The spatial variation in anisotropy, characterized by combining experimental and computational techniques, demonstrates the potential of tuning functional magnetic parameters like MCA by varying geometric shapes and sizes to further spintronic theory, in which micromagnetic order is integral. This size effect brought about by varying hole sizes of the micromagnets is hypothesized to modify local strain states, causing an energetic competition with anisotropy across their magnetic volume. Quantitative approximations from the magnetic domain images obtained at sub-micron spatial resolution described in this thesis work provide an essential and comprehensive framework to characterize spatial features of micromagnets. Finally, this research aims to enhance our fundamental understanding of varying magnetic anisotropy in topological spin textures and develop functional spintronic applications based on their control engineering in the future.

Chapter 5: Summary and Future Work

This thesis performs explorative analysis of spin textures observed in single crystal LSMO thin films patterned into circular donuts with 2 μm diameter and varying inner diameter of the hole. Chapter 1 details the material properties and magnetics of complex oxides, namely LSMO, and their emerging applications for advancing spintronics. LSMO thin films are grown using PLD and donut geometries as patterned by a unique ion-based implantation technique. By utilizing a donut structure, the vortex core was removed, and the domain textures were shown to exhibit chirality. The micromagnetic spin textures were found to be randomly distributed between chiral single and double-vortex (aka screwhead) states in the absence of a vortex core. These domain patterns were imaged using X-PEEM at 110 K and were observed to have a superposition of two flux-closure domain states - vortex and Landau patterns, much like their circular disc counterparts from previous findings [60]. Chapter 2 provides a detailed description of the experimental techniques carried out in this research work. Further, the LSMO donuts as imaged were found to possess an easy axis in <100> directions as opposed to <110> directions previously found with LSMO disc-shaped micromagnets with no hole imaged at lower temperatures.

Chapter 3 describes the salient features of LSMO donuts and domain textures therein in detail. A quantitative image analysis framework was developed to analyze the donuts, including computational modelling for characterizing the spatial variation of magnetocrystalline anisotropy that aligns magnetic domains along the <100> easy axes. MuMax^3 simulations were carried out following this computational framework to detail formation of the domain textures by using K_1

spatial modelling that was found to represent the anisotropy variation in the donuts. While many of the domain patterns were characterized to have a predominant vortex fraction, the vortex component varies in the magnetic volume of the individual micromagnets showing a spatially varying nature of magnetic anisotropy. Quantitative characterization through computational modeling and comparison with experimental data was done to better understand the role of magnetic anisotropy in the domain patterns observed. Chapter 4 summarizes the results obtained from comparing experimental and computational techniques. A unique balance of spatially varying anisotropies was found to exist along with geometrical effects in the micromagnets, hence, queuing possibilities to probe into their topology and tuning capabilities for functional spintronic applications in the future. The LSMO donuts with hole diameters 0.4 and 0.6 μm significantly deviate from the abrupt decaying sigmoidal K_1 profile obtained for the discs and show a decrease in the amount of vortex going towards either patterned edge. This spatial variation was captured in a saw-tooth model for K_1 spatial variation. Likewise, donuts with hole diameters 0.2, 0.8 μm, and 1.0 μm were found to be deviating from a sigmoidal K_1 profile for 110 K temperature.

Following vortex fraction analysis, simulations using a fine-tuned K_1 profile were shown to agree well with X-PEEM domain images, implying a significant strain contribution arising in the micromagnetic volume of the LSMO donuts. The strain effects that penalize magnetic anisotropic energies are a likely contributor to a change in easy-axis orientation arising from swelling of the matrix during the ion-implantation technique. The effect amplifies moving toward either of the circular edges of the donuts as represented by vortex fraction profiling. To understand the empirical variation of anisotropic energies while material properties remained unchanged, local energies were extracted from simulations to understand the differential energies present at the

edges and the center of the micromagnets. Overall, the LSMO micromagnetic domains bring out complex magnetism operating at the sub-micron scale. Given that patterning of the micromagnets into two or more unique geometries presents a significant variation of magnetocrystalline anisotropy in space, tuning the functional behavior of the material system is a promising venture in developing spintronic-based-memory applications.

Going ahead, these results obtained for an intermediate 110 K temperature must be compared with data from lower temperatures to better understand temperature dependence and their influence on magnetic energies in the domain patterns. Experimental and computational methodologies must be implemented to characterize the strain states in the micromagnets to gain a thorough understanding of these energetics in sub-micron scales. The characterization principles and quantitative framework provided in this thesis work can be further extended and applied to donut-shaped micromagnets with non-circular geometries like squares, diamonds, or hexagons with computational modifications to incorporate an additional geometric factor. Finally, accounting for MuMax^3 simulation accuracy and computational modeling in the form of linear approximations serve as a powerful tool in an endeavor to form a holistic understanding of complex oxide micromagnetic and their potential capabilities as spintronic devices.

References

[1] F. Estrada, E. J. Guzmán, O. Navarro, and M. Avignon, “Curie temperature behavior in half-metallic ferromagnetic double perovskites within the electronic correlation picture,” *Phys. Rev. B*, vol. 97, no. 19, p. 195155, May 2018, doi: 10.1103/PhysRevB.97.195155.

[2] “The resistance and thermoelectric properties of the transition metals,” *Proc. R. Soc. Lond. Ser. - Math. Phys. Sci.*, vol. 156, no. 888, pp. 368–382, Aug. 1936, doi: 10.1098/rspa.1936.0154.

[3] S. M. Thompson, “The discovery, development and future of GMR: The Nobel Prize 2007,” *J. Phys. Appl. Phys.*, vol. 41, no. 9, p. 093001, Mar. 2008, doi: 10.1088/0022-3727/41/9/093001.

[4] C. Wang, “Current Driven Magnetization Dynamics in Ferromagnets and Antiferromagnets,” PhD Thesis, 2015. doi: 10.13140/RG.2.1.2165.4801.

[5] B. N. Engel *et al.*, “A 4-Mb toggle MRAM based on a novel bit and switching method,” *IEEE Trans. Magn.*, vol. 41, no. 1, pp. 132–136, 2005, doi: 10.1109/TMAG.2004.840847.

[6] J. S. Moodera, L. R. Kinder, T. M. Wong, and R. Meservey, “Large magnetoresistance at room temperature in ferromagnetic thin film tunnel junctions,” *Phys. Rev. Lett.*, vol. 74, no. 16, p. 3273, 1995.

[7] W. Butler, X.-G. Zhang, T. Schulthess, and J. MacLaren, “Spin-dependent tunneling conductance of Fe| MgO| Fe sandwiches,” *Phys. Rev. B*, vol. 63, no. 5, p. 054416, 2001.

[8] P. Cappelletti and J. Slaughter, “6 - Embedded memory solutions: Charge storage based, resistive and magnetic,” in *Semiconductor Memories and Systems*, A. Redaelli and F. Pellizzer, Eds., in Woodhead Publishing Series in Electronic and Optical Materials. , Woodhead Publishing, 2022, pp. 159–215. doi: https://doi.org/10.1016/B978-0-12-820758-1.00007-8.

[9] J. Slaughter *et al.*, “High speed toggle MRAM with MgO-based tunnel junctions,” presented at the IEEE InternationalElectron Devices Meeting, 2005. IEDM Technical Digest., IEEE, 2005, pp. 873–876.

[10] D. Apalkov *et al.*, “Spin-transfer torque magnetic random access memory (STT-MRAM),” *ACM J. Emerg. Technol. Comput. Syst. JETC*, vol. 9, no. 2, pp. 1–35, 2013.

[11] S. Parkin, “Racetrack Memory: a high capacity, high performance, non-volatile spintronic memory,” in *2022 IEEE International Memory Workshop (IMW)*, May 2022, pp. 1–4. doi: 10.1109/IMW52921.2022.9779286.

[12] “Dissemination of IT for the Promotion of Materials Science.” [Online]. Available: https://www.doitpoms.ac.uk/tlplib/ferromagnetic/walls.php

[13] B. Kaviraj and J. Sinha, “Relativistic torques induced by currents in magnetic materials: physics and experiments,” *RSC Adv.*, vol. 8, no. 44, pp. 25079–25093, 2018, doi: 10.1039/C8RA04001J.

[14] P. Lai *et al.*, “An Improved Racetrack Structure for Transporting a Skyrmion,” *Sci. Rep.*, vol. 7, no. 1, p. 45330, Mar. 2017, doi: 10.1038/srep45330.

[15] Y. Zhang, W. S. Zhao, D. Ravelosona, J.-O. Klein, J. V. Kim, and C. Chappert, “Perpendicular-magnetic-anisotropy CoFeB racetrack memory,” *J. Appl. Phys.*, vol. 111, no. 9, p. 093925, May 2012, doi: 10.1063/1.4716460.

[16] P. Mandal *et al.*, “Designing switchable polarization and magnetization at room temperature in an oxide,” *Nature*, vol. 525, no. 7569, pp. 363–366, Sep. 2015, doi: 10.1038/nature14881.

[17] C. A. F. Vaz, “Electric field control of magnetism in multiferroic heterostructures,” *J. Phys.*

Condens. Matter, vol. 24, no. 33, p. 333201, Jul. 2012, doi: 10.1088/0953-8984/24/33/333201.
[18] J. Lu *et al.*, “Defect-Engineered Dzyaloshinskii–Moriya Interaction and Electric-Field-Switchable Topological Spin Texture in SrRuO3,” *Adv. Mater.*, vol. 33, no. 33, p. 2102525, Aug. 2021, doi: 10.1002/adma.202102525.
[19] Y. Kim, H. Yuk, R. Zhao, S. A. Chester, and X. Zhao, “Printing ferromagnetic domains for untethered fast-transforming soft materials,” *Nature*, vol. 558, no. 7709, pp. 274–279, Jun. 2018, doi: 10.1038/s41586-018-0185-0.
[20] C. A. R. Sá de Melo, “Interplay of magnetism and superconductivity at the nanometer scale: the case of complex oxide heterostructures,” *Proc. 3rd Pol.-US Workshop Supercond. Magn. Adv. Mater.*, vol. 387, no. 1, pp. 17–25, May 2003, doi: 10.1016/S0921-4534(03)00635-X.
[21] D. Meyers *et al.*, “Pure electronic metal-insulator transition at the interface of complex oxides,” *Sci. Rep.*, vol. 6, no. 1, p. 27934, Jun. 2016, doi: 10.1038/srep27934.
[22] A. K.-W. Chee, “On current technology for light absorber materials used in highly efficient industrial solar cells,” *Renew. Sustain. Energy Rev.*, vol. 173, p. 113027, Mar. 2023, doi: 10.1016/j.rser.2022.113027.
[23] D. Fu and M. Itoh, “Ferroelectricity in Silver Perovskite Oxides,” Aug. 2011.
[24] R. Ramesh and D. G. Schlom, “Creating emergent phenomena in oxide superlattices,” *Nat. Rev. Mater.*, vol. 4, no. 4, pp. 257–268, Apr. 2019, doi: 10.1038/s41578-019-0095-2.
[25] H. Assaridis, I. Panagiotopoulos, A. Moukarika, V. Papaefthymiou, and T. Bakas, “Structural and magnetic properties of La0.67−y(Sr,Ba,Ca)0.33+yMn1−xSnxO3 (x=0.01, 0.02, y=0, 0.07) perovskites,” *Solid State Commun.*, vol. 139, no. 9, pp. 473–478, Sep. 2006, doi: 10.1016/j.ssc.2006.07.002.
[26] O. Toulemonde, N. N’Guyen, F. Studer, and A. Traverse, “Spin State Transition in LaCoO 3 with Temperature or Strontium Doping as Seen by XAS,” *J. Solid State Chem. - J SOLID STATE CHEM*, vol. 158, pp. 208–217, May 2001, doi: 10.1006/jssc.2001.9094.
[27] C. N. R. Rao, “Charge, Spin, and Orbital Ordering in the Perovskite Manganates, Ln1-xAxMnO3 (Ln = Rare Earth, A = Ca or Sr),” *J. Phys. Chem. B*, vol. 104, no. 25, pp. 5877–5889, Jun. 2000, doi: 10.1021/jp0004866.
[28] Y. Wan-Lun and Z. Min-Guang, “Spin-Hamiltonian parameters of state 6 ions,” *Phys. Rev. B*, vol. 37, no. 16, p. 9254, 1988.
[29] H. Sawada, Y. Morikawa, K. Terakura, and N. Hamada, “Jahn-Teller distortion and magnetic structures in LaMnO 3,” *Phys. Rev. B*, vol. 56, no. 19, p. 12154, 1997.
[30] A. VAN HEUVELEN, “Relativistic Crystal-Field Splitting of Mn 2,” *J. Chem. Phys.*, vol. 46, no. 12, 1967.
[31] A. Liechtenstein, M. Katsnelson, and V. Gubanov, “Exchange interactions and spin-wave stiffness in ferromagnetic metals,” *J. Phys. F Met. Phys.*, vol. 14, no. 7, p. L125, 1984.
[32] R. L. Martin and F. Illas, “Antiferromagnetic exchange interactions from hybrid density functional theory,” *Phys. Rev. Lett.*, vol. 79, no. 8, p. 1539, 1997.
[33] C. Zener and R. Heikes, “Exchange interactions,” *Rev. Mod. Phys.*, vol. 25, no. 1, p. 191, 1953.
[34] J. De Clercq, “Modelling antiferromagnetic interfaces with MuMax3,” 2017.
[35] E. C. Stoner, “LXXX. Atomic moments in ferromagnetic metals and alloys with non-ferromagnetic elements,” *Lond. Edinb. Dublin Philos. Mag. J. Sci.*, vol. 15, no. 101, pp. 1018–1034, May 1933, doi: 10.1080/14786443309462241.
[36] Q. Liu *et al.*, “Ultra-large non-volatile modulation of magnetic moments in PbZr0.2Ti0.8O3/MgO/La0.7Sr0.3MnO3 heterostructure at room temperature via interfacial polarization mediation,” *Sci. Rep.*, vol. 7, Jun. 2017, doi: 10.1038/s41598-017-03019-x.
[37] Z. Trajanovic *et al.*, “Growth of colossal magnetoresistance thin films on silicon,” *Appl.*

Phys. Lett., vol. 69, no. 7, pp. 1005–1007, 1996.
[38] Y. Tokura, “Critical features of colossal magnetoresistive manganites,” *Rep. Prog. Phys.*, vol. 69, no. 3, p. 797, Feb. 2006, doi: 10.1088/0034-4885/69/3/R06.
[39] M. Opel, “Spintronic oxides grown by laser-MBE,” *J. Phys. Appl. Phys.*, vol. 45, no. 3, p. 033001, Dec. 2011, doi: 10.1088/0022-3727/45/3/033001.
[40] *Goodenough, J.B. (1963) Magnetism and the Chemical Bond. Interscience Monographs on Chemistry, Vol. 1, John Wiley, New York, 1-385.* [Online]. Available: Goodenough, J.B. (1963) Magnetism and the Chemical Bond. Interscience Monographs on Chemistry, Vol. 1, John Wiley, New York, 1-385.
[41] J. Kanamori, “Superexchange interaction and symmetry properties of electron orbitals,” *J. Phys. Chem. Solids*, vol. 10, no. 2, pp. 87–98, Jul. 1959, doi: 10.1016/0022-3697(59)90061-7.
[42] P. W. Anderson, “Antiferromagnetism. Theory of Superexchange Interaction,” *Phys Rev*, vol. 79, no. 2, pp. 350–356, Jul. 1950, doi: 10.1103/PhysRev.79.350.
[43] B. Náfrádi *et al.*, “Tuning ferromagnetism at room temperature by visible light,” *Proc. Natl. Acad. Sci.*, vol. 117, p. 201915370, Mar. 2020, doi: 10.1073/pnas.1915370117.
[44] A.-M. Haghiri-Gosnet and J.-P. Renard, “TOPICAL REVIEW: CMR manganites: physics, thin films and devices,” *J. Phys. -Appl. Phys. - J PHYS--APPL PHYS*, vol. 36, Jan. 2003.
[45] J. Hemberger *et al.*, “Structural, magnetic, and electrical properties of single-crystalline \mathrmLa_1\ensuremath-x\mathrmSr_x\mathrmMnO_3 (0.4<x<0.85),” *Phys Rev B*, vol. 66, no. 9, p. 094410, Sep. 2002, doi: 10.1103/PhysRevB.66.094410.
[46] M. Bowen *et al.*, “Nearly total spin polarization in La 2/3 Sr 1/3 MnO 3 from tunneling experiments,” *Appl. Phys. Lett.*, vol. 82, no. 2, pp. 233–235, 2003.
[47] M. Julliere, “Tunneling between ferromagnetic films,” *Phys. Lett. A*, vol. 54, no. 3, pp. 225–226, Sep. 1975, doi: 10.1016/0375-9601(75)90174-7.
[48] Y. Takamura, F. Yang, N. Kemik, E. Arenholz, M. D. Biegalski, and H. M. Christen, “Competing interactions in ferromagnetic/antiferromagnetic perovskite superlattices,” *Phys. Rev. B*, vol. 80, no. 18, p. 180417, 2009.
[49] L. F. Feiner and A. M. Oleś, “Electronic origin of magnetic and orbital ordering in insulating LaMnO 3,” *Phys. Rev. B*, vol. 59, no. 5, p. 3295, 1999.
[50] S. Majumdar and S. Dijken, “Pulsed laser deposition of La1-xSrxMnO3: Thin-film properties and spintronic applications,” *J. Phys. Appl. Phys.*, vol. 47, p. 034010, Dec. 2013, doi: 10.1088/0022-3727/47/3/034010.
[51] E. Dagotto, T. Hotta, and A. Moreo, “Colossal magnetoresistant materials: the key role of phase separation,” *Phys. Rep.*, vol. 344, no. 1, pp. 1–153, Apr. 2001, doi: 10.1016/S0370-1573(00)00121-6.
[52] X. Wang *et al.*, “Defects induced huge magnetoresistance in epitaxial La1–xSrxMnO3 thin films deposited by magnetic sputtering,” *Appl. Phys. Lett.*, vol. 115, no. 18, p. 182405, Oct. 2019, doi: 10.1063/1.5120838.
[53] S. K. Chaluvadi, “Influence of the epitaxial strain on magnetic anisotropy in LSMO thin films for spintronics applications,” 2017.
[54] M. Foerster *et al.*, “Efficient spin transfer torque in La2/3Sr1/3MnO3 nanostructures,” *Appl. Phys. Lett.*, vol. 104, no. 7, 2014.
[55] E. Goering *et al.*, “Strong Anisotropy of Projected 3 d Moments in Epitaxial CrO 2 Films,” *Phys. Rev. Lett.*, vol. 88, no. 20, p. 207203, 2002.
[56] Y. Suzuki *et al.*, “Magnetic anisotropy of doped manganite thin films and crystals,” *J. Appl. Phys.*, vol. 83, no. 11, pp. 7064–7066, 1998.
[57] L. M. Berndt, V. Balbarin, and Y. Suzuki, “Magnetic anisotropy and strain states of (001) and (110) colossal magnetoresistance thin films,” *Appl. Phys. Lett.*, vol. 77, no. 18, pp. 2903–2905, Oct. 2000, doi: 10.1063/1.1321733.
[58] E. Houwman *et al.*, “Out-of-plane magnetic domain structure in a thin film of La_ {0.67}

Sr_ {0.33} MnO_ {3} on SrTiO_ {3}(001) observed by magnetic force microscopy," *Phys Rev B*, vol. 77, May 2008, doi: 10.1103/PhysRevB.77.184412.
[59] N. Nagaosa and Y. Tokura, "Topological properties and dynamics of magnetic skyrmions," *Nat. Nanotechnol.*, vol. 8, no. 12, pp. 899–911, 2013.
[60] M. S. Lee *et al.*, "Tailoring Spin Textures in Complex Oxide Micromagnets," *ACS Nano*, vol. 10, no. 9, pp. 8545–8551, Sep. 2016, doi: 10.1021/acsnano.6b03770.
[61] Y. Suzuki, H. Y. Hwang, S.-W. Cheong, and R. B. van Dover, "The role of strain in magnetic anisotropy of manganite thin films," *Appl. Phys. Lett.*, vol. 71, no. 1, pp. 140–142, Jul. 1997, doi: 10.1063/1.119454.
[62] Y. Takamura, R. Chopdekar, E. Arenholz, and Y. Suzuki, "Control of the magnetic and magnetotransport properties of La0. 67Sr0. 33MnO3 thin films through epitaxial strain," *Appl. Phys. Lett.*, vol. 92, no. 16, 2008.
[63] S. Zhang *et al.*, "Determining the oxygen stoichiometry of cobaltite thin films," *Chem. Mater.*, vol. 34, no. 5, pp. 2076–2084, 2022.
[64] A. Tebano *et al.*, "Strain-induced phase separation in La 0.7 Sr 0.3 Mn O 3 thin films," *Phys. Rev. B*, vol. 74, no. 24, p. 245116, 2006.
[65] K. Chopra and S. Bahl, "Amorphous versus crystalline GeTe films. I. Growth and structural behavior," *J. Appl. Phys.*, vol. 40, no. 10, pp. 4171–4178, 1969.
[66] A. Herklotz, D. Lee, E.-J. Guo, T. L. Meyer, J. R. Petrie, and H. N. Lee, "Strain coupling of oxygen non-stoichiometry in perovskite thin films," *J. Phys. Condens. Matter*, vol. 29, no. 49, p. 493001, Nov. 2017, doi: 10.1088/1361-648X/aa949b.
[67] J. W. Matthews and A. E. Blakeslee, "Defects in epitaxial multilayers: I. Misfit dislocations," *J. Cryst. Growth*, vol. 27, pp. 118–125, Dec. 1974, doi: 10.1016/S0022-0248(74)80055-2.
[68] F. Yang, N. Kemik, M. D. Biegalski, H. M. Christen, E. Arenholz, and Y. Takamura, "Strain engineering to control the magnetic and magnetotransport properties of La0. 67Sr0. 33MnO3 thin films," *Appl. Phys. Lett.*, vol. 97, no. 9, 2010.
[69] A. J. Haider, T. Alawsi, M. J. Haider, B. A. Taha, and H. A. Marhoon, "A comprehensive review on pulsed laser deposition technique to effective nanostructure production: trends and challenges," *Opt. Quantum Electron.*, vol. 54, no. 8, p. 488, Jun. 2022, doi: 10.1007/s11082-022-03786-6.
[70] R. Desfeux, S. Bailleul, A. Da Costa, W. Prellier, and A. Haghiri-Gosnet, "Substrate effect on the magnetic microstructure of La 0.7 Sr 0.3 MnO 3 thin films studied by magnetic force microscopy," *Appl. Phys. Lett.*, vol. 78, no. 23, pp. 3681–3683, 2001.
[71] M. Sahana, T. Walter, K. Dörr, K.-H. Müller, D. Eckert, and K. Brand, "Magnetic properties of heteroepitaxial La 0.7 Sr 0.3 MnO 3/SrTiO 3 superlattices," *J. Appl. Phys.*, vol. 89, no. 11, pp. 6834–6836, 2001.
[72] A. Haghiri-Gosnet *et al.*, "Microstructure and magnetic properties of strained La 0.7 Sr 0.3 MnO 3 thin films," *J. Appl. Phys.*, vol. 88, no. 7, pp. 4257–4264, 2000.
[73] T. Gagnidze, H. Ma, C. Cancellieri, G.-L. Bona, and F. La Mattina, "Structural properties of ultrathin SrO film deposited on SrTiO 3 Structural properties of ultrathin SrO film deposited on SrTiO 3," *Sci. Technol. Adv. Mater.*, vol. 20, Apr. 2019, doi: 10.1080/14686996.2019.1599693.
[74] I. N. Stranski and L. Krastanow, "Zur Theorie der orientierten Ausscheidung von Ionenkristallen aufeinander," *Monatshefte Für Chem. Verwandte Teile Anderer Wiss.*, vol. 71, pp. 351–364, 1937.
[75] R. Eason, Ed., *Pulsed laser deposition of thin films: applications-led growth of functional materials*. John Wiley & Sons Ltd., 2006. [Online]. Available: https://eprints.soton.ac.uk/48210/
[76] Y. Takamura *et al.*, "Tuning magnetic domain structure in nanoscale La0. 7Sr0. 3MnO3 islands," *Nano Lett.*, vol. 6, no. 6, pp. 1287–1291, 2006.

[77] “M. Lee, Designing Magnetic Spin Textures in Complex Oxide Thin Films, University of California, Davis, 2018.” [Online]. Available: M. Lee, Designing Magnetic Spin Textures in Complex Oxide Thin Films, University of California, Davis, 2018
[78] J. Ma *et al.*, “Strain-induced modulation of oxygen vacancies and magnetic properties in La0.5Sr0.5MnO3 thin films,” *MRS Commun.*, vol. 6, pp. 1–6, Nov. 2016, doi: 10.1557/mrc.2016.55.
[79] *J. Stöhr and H. C. Siegmann, Magnetism: From Fundamentals to Nanoscale Dynamics (2006)*. [Online]. Available: J. Stöhr and H. C. Siegmann, Magnetism: From Fundamentals to Nanoscale Dynamics (2006)
[80] J. Kowalska and S. DeBeer, “The role of X-ray spectroscopy in understanding the geometric and electronic structure of nitrogenase,” *Biochim. Biophys. Acta BBA-Mol. Cell Res.*, vol. 1853, no. 6, pp. 1406–1415, 2015.
[81] M. Giménez-Marqués *et al.*, “GraftFast surface engineering to improve MOF nanoparticles furtiveness,” *Small*, vol. 14, no. 40, p. 1801900, 2018.
[82] G. van der Laan and A. I. Figueroa, “X-ray magnetic circular dichroism—A versatile tool to study magnetism,” *Coord. Chem. Rev.*, vol. 277, pp. 95–129, 2014.
[83] R. Reeve, H. Elmers, F. Büttner, and M. Kläui, *Magnetic Imaging and Microscopy*. 2018.
[84] Y. Kim, S. Ryu, and H. Jeen, “Strain-effected physical properties of ferromagnetic insulating La 0.88 Sr 0.12 MnO 3 thin films,” *RSC Adv.*, vol. 9, pp. 2645–2649, Jan. 2019, doi: 10.1039/C8RA09851D.
[85] J. Stöhr *et al.*, “Element-Specific Magnetic Microscopy with Circularly Polarized X-rays,” *Science*, vol. 259, no. 5095, pp. 658–661, 1993, doi: 10.1126/science.259.5095.658.
[86] “XAS/XMCD Sum rules.” [Online]. Available: https://xiaoshanxu.unl.edu/system/files/sites/unl.edu.cas.physics.xiaoshan-xu/files/private/2020_12_18%20XMCD%20Sum%20Rules.pdf
[87] T. Kinoshita, “Photoemission Electron Microscope,” 2018, pp. 465–469. doi: 10.1007/978-981-10-6156-1_76.
[88] T. Kinoshita, “Photoemission Electron Microscope,” in *Compendium of Surface and Interface Analysis*, The Surface Science Society of Japan, Ed., Singapore: Springer Singapore, 2018, pp. 465–469. doi: 10.1007/978-981-10-6156-1_76.
[89] Anonymous, “Abstracts of Papers to be Presented at the 1955 Thanksgiving Meeting at the University of Chicago, Chicago, Illinois, November 25 and 26, 1955,” *Phys Rev*, vol. 100, no. 4, pp. 1235–1235, Nov. 1955, doi: 10.1103/PhysRev.100.1235.
[90] A. Vansteenkiste and B. Van de Wiele, “MuMax: A new high-performance micromagnetic simulation tool,” *J. Magn. Magn. Mater.*, vol. 323, no. 21, pp. 2585–2591, Nov. 2011, doi: 10.1016/j.jmmm.2011.05.037.
[91] S.-W. Cheong and X. Xu, “Magnetic chirality,” *Npj Quantum Mater.*, vol. 7, no. 1, p. 40, Apr. 2022, doi: 10.1038/s41535-022-00447-5.
[92] G. Hrkac, P. Keatley, M. Bryan, and K. Butler, “Magnetic vortex oscillators,” *J. Phys. Appl. Phys.*, vol. 48, p. 453001, Oct. 2015, doi: 10.1088/0022-3727/48/45/453001.
[93] R. P. Cowburn, D. Koltsov, A. Adeyeye, M. Welland, and D. Tricker, “Single-domain circular nanomagnets,” *Phys. Rev. Lett.*, vol. 83, no. 5, p. 1042, 1999.
[94] V. Novosad, F. Y. Fradin, P. E. Roy, K. S. Buchanan, K. Y. Guslienko, and S. D. Bader, “Magnetic vortex resonance in patterned ferromagnetic dots,” *Phys. Rev. B*, vol. 72, no. 2, p. 024455, 2005.
[95] K. Buchanan, K. Y. Guslienko, A. Doran, A. Scholl, S. Bader, and V. Novosad, “Magnetic remanent states and magnetization reversal in patterned trilayer nanodots,” *Phys. Rev. B*, vol. 72, no. 13, p. 134415, 2005.
[96] K.-W. Moon, B. S. Chun, W. Kim, Z. Qiu, and C. Hwang, “Control of skyrmion magnetic bubble gyration,” *Phys. Rev. B*, vol. 89, no. 6, p. 064413, 2014.
[97] C. Schütte and M. Garst, “Magnon-skyrmion scattering in chiral magnets,” *Phys. Rev. B*,

vol. 90, no. 9, p. 094423, 2014.
[98] J. Martın, J. Nogues, K. Liu, J. Vicent, and I. K. Schuller, “Ordered magnetic nanostructures: fabrication and properties,” *J. Magn. Magn. Mater.*, vol. 256, no. 1–3, pp. 449–501, 2003.
[99] L. Heyderman *et al.*, “Photoemission electron microscopy study of remanent magnetic domain states in ferromagnetic wedge films deposited on substrates with micrometer-sized square plateaus,” *J. Appl. Phys.*, vol. 99, no. 6, 2006.
[100] S.-B. Choe *et al.*, “Vortex core-driven magnetization dynamics,” *Science*, vol. 304, no. 5669, pp. 420–422, 2004.
[101] T. Shinjo, T. Okuno, R. Hassdorf, † K Shigeto, and T. Ono, “Magnetic vortex core observation in circular dots of permalloy,” *science*, vol. 289, no. 5481, pp. 930–932, 2000.
[102] Y. Lee, A. Ramdas, and R. Aggarwal, “Energy gap, excitonic, and “‘internal”’Mn 2+ optical transition in Mn-based II-VI diluted magnetic semiconductors,” *Phys. Rev. B*, vol. 38, no. 15, p. 10600, 1988.
[103] “Aharoni, Amikam (1996).” [Online]. Available: https://archive.org/details/introductiontoth00ahar/page/n5/mode/2up
[104] H. Wang, C. Du, P. C. Hammel, and F. Yang, “Strain-tunable magnetocrystalline anisotropy in epitaxial Y_3\mathrmFe_5\mathrmO_12 thin films,” *Phys Rev B*, vol. 89, no. 13, p. 134404, Apr. 2014, doi: 10.1103/PhysRevB.89.134404.
[105] M. Krupinski *et al.*, “Magnetic transition from dot to antidot regime in large area Co/Pd nanopatterned arrays with perpendicular magnetization,” *Nanotechnology*, vol. 28, no. 8, p. 085302, Jan. 2017, doi: 10.1088/1361-6528/aa5656.
[106] T.A. Wynn, “Anisotropy and Micromagnetics in Complex Oxide Thin Film”, M.S. Thesis, Dept. Of Materials Science and Engineering, Univ. of California, Davis, 2015.

APPENDIX A: First-order approximation models and distortion correction fitting

Python scripts

#1. Polar Transform code

```
import polarTransform
import matplotlib.pyplot as plt
import numpy as np
import imageio

#Read Image path
image = imageio.imread(r"<pathname>)
# Get image dimensions
height, width, channels = image.shape
# Define the center of polar transformation
center = (width // 2, height // 2)

# polar transformation
polarImage, ptSettings = polarTransform.convertToPolarImage(image,  center, hasColor=True)

#cartesianImage = ptSettings.convertToCartesianImage(polarImage)
print(polarImage.shape)

plt.figure()
plt.imshow(np.rot90(polarImage), origin='lower')
plt.show()
```

#2. Selection of matrix coordinates for ROI

```
import cv2
import numpy as np

# select points using mouse click
def select_points(event, x, y, flags, param):
   if event == cv2.EVENT_LBUTTONDOWN and len(source_points) < 4:   #select more points
to define ROI ?
       cv2.circle(image,  (x, y), 5, (0, 0, 255), -1)
       source_points.append((x, y))
       cv2.imshow('Select Points', image)

source_points = []
```

```
# Load image
image = cv2.imread(r<image path>)

# Creating window to display the image
cv2.imshow('Select Points', image)
cv2.setMouseCallback('Select Points', select_points)

# selecting points
while len(source_points) < 4:
    cv2.waitKey(10)

# Close the window
cv2.destroyWindow('Select Points')

# Points to be corrected
print("Source Points:", source_points)
```

#3.Perspective correction after ROI identification

```
from IPython.display import display, Image
import cv2
import numpy as np

def correct_perspective(image_path):
    # Load the image
    image = cv2.imread(image_path)
    display(Image(data=cv2.imencode('.png', image)[1].tobytes()))
    height, width, _ = image.shape

    # Define four pairs of points to correct the circular features
    original_points = np.float32([[137, 9], [220, 84], [124, 160], [53, 78]])
    corrected_points = np.float32([[130,8], [220, 84], [124, 150], [53, 78]])

    # Calculate the perspective transformation matrix
    perspective_matrix = cv2.getPerspectiveTransform(original_points, corrected_points)

    # Apply the perspective transformation to the image
    corrected_image = cv2.warpPerspective(image, perspective_matrix, (width, height))

    return corrected_image
```

```
# Specify the path to distorted image
input_image_path = r'<name>

# Perform perspective correction
corrected_image = correct_perspective(input_image_path)

# Display the corrected image
display(Image(data=cv2.imencode('.png', corrected_image)[1].tobytes()))
```

#4. Radial Scan

```
import cv2
import numpy as np
import matplotlib.pyplot as plt
from scipy.optimize import curve_fit
from sklearn.metrics import r2_score

radius = None

def custom_square_wave(x):
    # Function to generate the square wave with modified piece 2
    # First piece
    piece1 = np.where((x >= 44) & (x < 3*(45)), 1, 0)
    piece1 = np.where((x >= 3*(45)) & (x < 180), 0, piece1)

    # Second piece
    piece2 = np.where((x >= 180) & (x < 5*(45)), 0, 0)
    piece2 = np.where((x >= 5*(45)) & (x <= (2*180 - 44)), -1, piece2)

    return piece1 + piece2

def my_wave(t, phi, amp_sin, amp_square):
    # Generate custom square wave
    square_wave =  amp_square * custom_square_wave(t+phi)

    # Sinusoidal wave
    sin_wave = amp_sin  * np.sin(np.deg2rad(t+phi))

    fv = amp_sin/(amp_sin  + amp_square)
```

```
    print(fv)

    # Combining sinusoidal and square waves
    combined_wave = sin_wave + square_wave

    return combined_wave

def get_radius(center, point):
    global radius
    radius = int(np.linalg.norm(np.array(point)  - np.array(center)))

def main(image_path):
    global radius
    image = cv2.imread(image_path)
    image_copy = image.copy()

    center = None
    point = None

    def select_point(event, x, y, flags, param):
        nonlocal center, point

        if event == cv2.EVENT_LBUTTONDOWN:
            if center is None:
                center = (256, 255)
                cv2.circle(image_copy,  center, 3, (0, 0, 255), -1)
            elif point is None:
                point = (243, 80)
                cv2.circle(image_copy,  point, 3, (255, 0, 0), -1)
                get_radius(center, point)
                cv2.circle(image_copy,  center, radius, (0, 255, 0), 4)

    cv2.namedWindow('Select Center and Point')
    cv2.setMouseCallback('Select Center and Point', select_point)

    while True:
        cv2.imshow('Select Center and Point', image_copy)
        key = cv2.waitKey(1) & 0xFF
        if center is not None and point is not None:
            break
```

```
    cv2.destroyAllWindows()
    print(center)
    print(point)
    pixel_distance = np.linalg.norm(np.array(point)  - np.array(center))
    print(pixel_distance)

    radius = int(np.linalg.norm(np.array(point)  - np.array(center)))

    intensity_values = []
    num_angles = 360
    thickness = 4 #in pixels

    for angle in (np.linspace(0, 361)):
        intensity_sum = 0
        for r in range(radius - thickness // 2, radius + thickness // 2):
            x = int(center[0] + r * np.cos(np.deg2rad(angle)))
            y = int(center[1] + r * np.sin(np.deg2rad(angle)))
            intensity_sum += image[y, x, 0]  # Accumulating intensity values within the ring
        intensity_values.append(intensity_sum / thickness)  # Calculating the average intensity

    intensity_values = np.array(intensity_values)
    max_intensity = np.max(np.abs(intensity_values))
    normalized_intensity = intensity_values / max_intensity

    mean_intensity = (np.max(normalized_intensity)  + np.min(normalized_intensity))  / 2.0
    modified_intensity = (normalized_intensity - mean_intensity) * 2.1

    phi = (np.argmax(modified_intensity) * 360) / len(modified_intensity)  # converting to
degrees

    sin_weight = 0.50
    square_weight = 0.50

    # Curve fitting using scipy's curve_fit
    angles = np.linspace(0, 361)  # using degrees instead of radians

    phi_guess = phi
    sin_weight_guess = 0.5
    square_weight_guess = 0.5
```

```
# Normalizing initial guesses
total_amplitude_guess = sin_weight_guess + square_weight_guess
sin_weight_guess /= total_amplitude_guess
square_weight_guess /= total_amplitude_guess

p0 = [phi_guess, sin_weight_guess, square_weight_guess]

# Curve fitting with constraints
bounds = ([-np.inf, 0, 0], [np.inf, 1, 1])  # Constraint: 0 <= amp_sin, amp_square <= 1

popt, _ = curve_fit(my_wave, angles, modified_intensity, p0=p0, bounds=bounds)
fitted_curve = my_wave(angles, *popt)*1.0

sin_wave = np.sin(np.deg2rad(angles))
square_wave =  custom_square_wave((angles))

# Ploting fitted curves
plt.plot(angles, modified_intensity, label='Raw Data', color='green')
plt.plot(angles, fitted_curve, label='Fitted Wave', color='purple')
#plt.plot(angles, sin_wave, linestyle='dotted', label='Sin Wave', color='red')
#plt.plot(angles, square_wave, linestyle='dotted', label='Square Wave', color='blue')

plt.title('Wave fitting')
plt.xlabel('Angle (degrees)')  # labeling in degrees
plt.ylabel('Normalized Intensity')
plt.legend()
plt.xticks(np.arange(0, 361, 60))
plt.show()

# Display the image with the circle
cv2.imshow('Image with Circle', image_copy)

cv2.waitKey(0)
cv2.destroyAllWindows()

# Calculate R^2 value
r_squared = r2_score(modified_intensity, fitted_curve)
print(f"R^2 value: {r_squared}")
```

```
if __name__ == '__main__':
    image_path = r"<path>"
    main(image_path)
```

APPENDIX B: MuMax^3 Simulations

GOLAN script

```
SetMesh(512, 512, 1, 5e-09, 5e-09, 4e-08, 0, 0, 0)
Aex = 3.6e-12
anisC1 = vector(1, 1, 0)
anisC2 = vector(-1, 1, 0)
Msat = 390000
disc := cylinder(2e-6, 40e-9)
setgeom(disc) #setting disc
m = Vortex(1, 1) #setting vortex domain
Aex = 3.6e-12
Kc1 = 0   #For uniform K1
snapshot(m)
relax()
m = Vortex(1, 1)
relax()
hole = cylinder(<ID>, 40e-9)
donut = disc.sub(hole)
setgeom(donut)
m = Vortex(1, 1)
relax()
save(m)
//output directory: mumax-2024-04-27_13h36.out/
hole := cylinder(0.4e-6, 40e-9)
donut := disc.sub(hole)
setgeom(donut)
m = Vortex(1, 1)
#Defining rings
<ring1 := cylinder(0.6e-6, 40e-9).sub(hole)> #Example
defregion(1, ring1)
edgesmooth = 8

kc1.setregion(1, <K1>) #Example
relax()
m = Vortex(1, 1)
#Extracting Energies
e1 := edens_anis.region(<region>)
d1 := edens_demag.region(<region>)
ex1 := edens_exch.region(<region>)
```

API access: https://mumax.github.io/api.html [90]

B.1 MuMax^3 Simulations

MuMax^3 simulations of LSMO donuts (ID 0.0 - 1 μm) obtained for 32 K at which Lee *et al* calculated the spatial variation of the LSMO disc shaped micromagnets are shown in Figure B.1. These simulations are performed using the saw-tooth model (in Figure B.2.) for approximating K_1 in space. Subsequently, radial intensity profiling was done to obtain VF profiles and included in the results (refer to Chapter 4) for comparison. The simulated results can be further compared with future work on imaging domain patterns of the LSMO donuts at low temperatures.

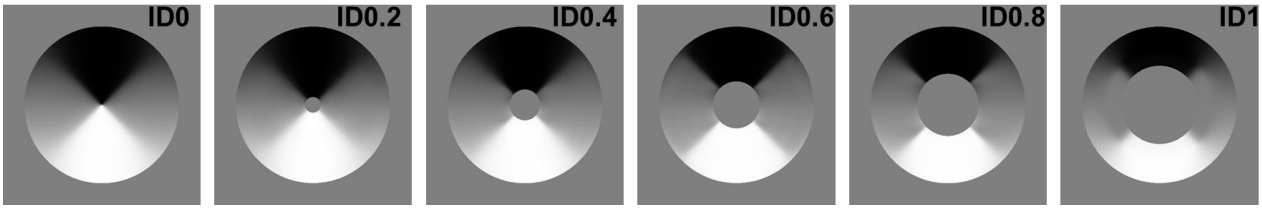

Fig. B.1. MuMax^3 simulated domain images for LSMO donuts with an outer diameter of 2 μm and varying ID performed at low temperatures (~32 K). The simulations consider <100> easy axes directions observed for the LSMO donuts.

B.2 K_1 approximation fit for the saw-tooth model

Figure B.2.1 shows the K_1 approximation of ID 0.4 μm LSMO donut using the saw-tooth model and linear fitting to yield a vortex fraction profile (refer to Figure 4.8). The model shows K_1 reaches zero at the 0.6 μm radial mark with a flat step to account for maximum MCA and rising subsequently towards the outer circular edge. The model is linearly shifted upwards considering the average K_1 values of the LSMO micromagnetic discs at 32 K determined by Lee *et al.* Considering the saw-tooth model of K_1 spatial variation holds for the LSMO donuts, going forward temperature-dependence of MCA can be established to tune magnetic properties and thereby their

application in spintronic application. A similar operation was performed for the rest of the hole diameters.

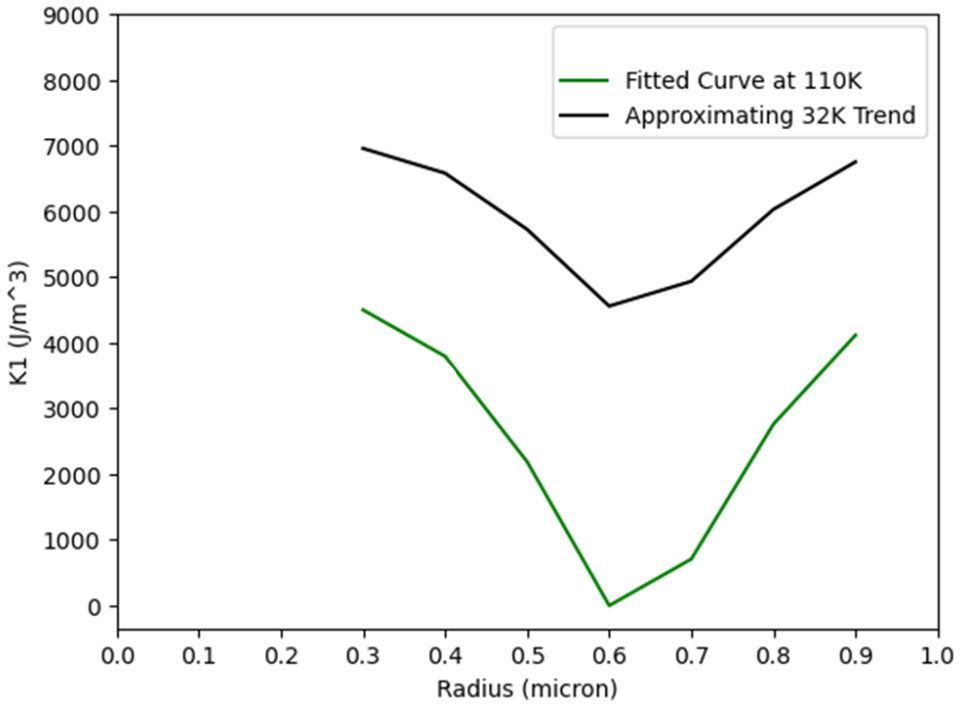

Fig B.2 K_1 approximation trend for ID 0.4 μm fitting at 110 K (in green). The curve is linearly shifted to represent K_1 spatial variation at lower temperatures (in black).

Table S1: Simulation Parameters

T (K)	Ms (A/m)	Dsp (meV*A^2)	A_{ex} (pJ/m)
110	390,000	210	3.6

Experimental values used as constants in the MuMax^3 simulations of the LSMO micromagnetic donuts. Adapted from reference [60]. K_1 values are set up according to the generated saw-tooth model or decay model corresponding to each of the hole diameters.